This electronic thesis or dissertation has been downloaded from the King’s Research Portal at https://kclpure.kcl.ac.uk/portal/

Magnetic Resonance Compatible Tactile Force Sensing Using Optical Fibres for Minimally Invasive Surgery

Xie, Hui

Awarding institution:
King's College London

The copyright of this thesis rests with the author and no quotation from it or information derived from it may be published without proper acknowledgement.

END USER LICENCE AGREEMENT

Unless another licence is stated on the immediately following page this work is licensed under a Creative Commons Attribution-NonCommercial-NoDerivatives 4.0 International licence. https://creativecommons.org/licenses/by-nc-nd/4.0/

You are free to copy, distribute and transmit the work

Under the following conditions:

- Attribution: You must attribute the work in the manner specified by the author (but not in any way that suggests that they endorse you or your use of the work).
- Non Commercial: You may not use this work for commercial purposes.
- No Derivative Works - You may not alter, transform, or build upon this work.

Any of these conditions can be waived if you receive permission from the author. Your fair dealings and other rights are in no way affected by the above.

Take down policy

If you believe that this document breaches copyright please contact librarypure@kcl.ac.uk providing details, and we will remove access to the work immediately and investigate your claim.

Download date: 29. Dec. 2024

Magnetic Resonance Compatible Tactile Force Sensing Using Optical Fibres for Minimally Invasive Surgery

by Hui Xie

A thesis submitted in partial fulfilment of the requirements for the degree of

‘Doctor of Philosophy’ in Robotics

to

King’s College London
University of London
School of Natural and Mathematical Sciences
Department of Informatics
Centre for Robotics Research

June 2014

Abstract

This thesis presents research in design, fabrication and testing of magnetic resonance (MR) compatible tactile array sensors based on light intensity modulation using optical fibres. The popularity of minimally invasive surgery (MIS) opens the field of tactile sensing for medical use, especially in MR environment. The departure from conventional sensing approaches (such as capacitive and piezoresistive) allows the development of tactile sensors which are low cost, small in size, lightweight, free from electromagnetic interference, water and corrosion resistant and capable to operate in harsh environments. In the framework of this PhD study, a number of MR compatible tactile array sensors have been developed, including uniaxial tactile array sensors and an x- and y-axis lateral contact sensor. Mathematical models for these newly-developed tactile sensors have been created and verified. Force is measured through the displacement of a flexible structure with a known stiffness, modulating in turn the light intensity in the employed optical fibres. For the tactile array sensor, a 2D vision system is applied to detect light signals from all sensing elements via the optical fibres – this new approach provides a great potential for high density tactile array sensing, employing a low-cost vision sensor. For the lateral sensor, high-speed/high-sensitivity detectors are utilized to calculate contact force position and magnitude. Combined with 3D printing technology, a miniature tactile probe head capable of palpation in MIS has been designed and tested in *ex vivo* tissue palpation experiments. All sensor systems developed in this thesis are MR compatible and immune to electromagnetic

noise. The proposed sensing structures and principles show high miniaturization and resolution capabilities, making them suitable for integration with medical tools.

Acknowledgments

My research could not have been completed without guidance from my supervisors, contributions from my colleagues and moral support from my family. I would like to express here my sincere thanks to the all persons who have given me great support throughout my PhD research.

First and foremost, I would like to give special thanks to my supervisor, Prof. Kaspar Althoefer, who has drawn my attention to tactile sensing research. I am really indebted to him for his guidance and numerous suggestions. I would also like to deliver my sincere thanks to my other supervisor, Dr. Hongbin Liu, for his useful advice and encouragement. Without my supervisors, I would not have been able to start my research, make significant progress on my study and finally complete my PhD thesis.

In addition, I would like to acknowledge the help and friendly support of my colleagues at the Centre for Robotics Research. Especially, I am grateful to Prof. Lakmal Seneviratne, Dr. Thrish Nanayakkara, Dr. Pinyo Puangmali, Dr. Noh Yohan, Allen Jiang, Dr. Helge Wurdemann, Min Li, Christian Deters, Dr. Sina Sareh, Chen Qiu, Dr. Panagiotis Polygerinos, Shan Luo, Peng Qi, Joao Bimbo, Dr. Jichun Li, Dr. Ali Ataollahi, Dr. Dinusha Zbyszewski, Dr. Xiaojing Song for spending a great amount of time with me on several technical discussions.

Finally, I am deeply thankful to my wife Li Sun and my parents Huimin Xie and Fuyun Zhou who have always been supporting me.

Table of Contents

Nomenclature

MR	Magnetic resonance
MRI	Magnetic resonant imaging
ISO	International Standard Organization
MIS	Minimally invasive surgery
FDA	Food and Drug Administration
CT	Computerized tomography
ABS	Acrylonitrile butadiene styrene
V	Voltage
I	Current
R	Electrical resistance
PVDF	Polymer polyvinylidene fluoride
PDMS	Polydimethylsiloxane
C	Capacitance
A	Size of overlap area between two plates

ε_0	The permittivity of free space
ε_r	The relative permittivity of dielectric material
d_c	The distance between two plates
PPS	Pressure profile systems
CCD	Charge-coupled device
FBG	Fibre Bragg gratings
fMRI	Functional magnetic resonant imaging
d	Distance between transmission fibre and receiving fibre
θ	Angle between fibre and mirror
D	Diameter of optical fibres
h	Distance between the centre of the fibre and the mirror
L	Distance between virtual fibres
S	Projection diameter of light transmitted to the receiving fibre
α	Radiation angle
x	Downward shift distance of mirrors
S'	Projection diameter after mirror shifting

r	The light beam's radial distance
$I_{(r)}$	The intensity of the beam
I_o	The beam's maximum intensity
w_o	The mode-field radius
Φ_{VT}	The total virtually transmitted light flux
ΔI_o	The variation of maximum light intensity between virtual transmitting and receiving fibres
$I_o^{'}$	The maximum intensity of the light projected at the tip of virtual transmitting fibre
β	Divergence angle
Φ_r	The receiving fibre's maximum collected light flux
N	The number of the activated pixels in the sensing area
N_{max}	Maximum value of the number of the activated pixels in the sensing area
I	Light intensity
R	Red value of each pixel
G	Green value of each pixel

B	Blue value of each pixel
n	Numerical value of each pixel
$I_{threshold}$	Defined intensity threshold to eliminate ineffective pixels
N	The total numerical value of the pixels in each sensing area
K	The total number of the pixels in each sensing area
f	Force
MEMS	Microelectromechanical systems
CMOS	Complementary metal–oxide–semiconductor
$g(x, y)$	The grey value of the pixel coordinated at (x, y) in the image
$g_T(x, y)$	The value of pixel at (x, y) after thresholding
ρ_1, ρ_2, ρ_3	Constant parameters
σ_1, σ_2	Constant parameters
$\gamma_1, \gamma_2, \gamma_3$	Constant parameters
δ_1, δ_2	Constant parameters
RMSE	Root mean square error

SD	Standard deviation
DAQ	Data acquisition
V_a, V_b, V_c	Outputs of the detectors
AD, BE, CG	Displacement between fibres and mirrors
K_1, K_2, K_3	The transforming factors of detectors converting distance to voltage
α	The location angle of applied force
d_s	The shifting distance of outer ring due to force applied
μ_a, μ_b, μ_c	Constant parameters
$\Delta V_a, \Delta V_b, \Delta V_c$	The changes of voltage outputs of three sensing elements
d_a, d_b, d_c	The displacement changes at three points
K_a, K_b, K_c	Constant parameters
d_1, d_2, d_3	The displacement changes of the outer ring during three tests
Kf_a, Kf_b, Kf_c	Constant parameters
ε_a, ε_b, ε_c	Constant parameters

List of Tables

Number *Page*

List of Figures

Number *Page*

Chapter 1 Introduction

This chapter describes the overview, aim and objectives, summary of contributions and the outline of this thesis.

1.1. OVERVIEW

The word *robot* was first introduced in *Rossum's Universal Robots,* a 1920s play by Karel Capek. Since then robots of many types and different functions have been created and have increasingly become important in humans' everyday lives. For example, many consumer goods from automobiles to electronic products such as computers and mobile phones are assembled not by human hands but by an industrial automated assembly line [1]. During medical procedures, where very accurate micro motions are needed through small size incisions surgeons may need assistance from surgical robots [2]. Robots can carry out certain tasks in a repetitive and precise manner, but to achieve more complex tasks, especially when changes occur, they also need to perceive the external environment [3]. It is something humans take for granted but is a difficult process for machines.

Many sensors have been developed to this end, such as sound sensors to serve as robotic ears, contact and temperature sensors to act as skin and vision sensors to act as eyes. While other sensors have been well explored and developed, the contact sensors, especially force and tactile sensors, still need to be further investigated [4]. There are several tactile sensing methods, such as piezoelectric-based sensing [5], strain gauges sensing [6] and capacitive-based sensing [7]. However, the problem is that few of them can satisfy medical requirements, such as magnetic resonant imaging (MRI) compatibility, small size to fit through a trocar port in minimally invasive surgery, and low cost so as to be disposable after a single surgery. One of the methods which satisfies medical requirements such as high electromagnetic resonance capability is the light intensity modulation method which uses optical fibres [8]. Optical fibres allow the creation of tactile sensors which are low cost, small in size, lightweight, free from electromagnetic interference, water and corrosion resistant and capable to operate in harsh environments. Existing intensity modulation fibre optic sensors [9] are mostly based on a set of optoelectronics, where each optoelectronic receiver (consisting of a photodiode, photoresistor or phototransistor and a signal conditioning circuit) converts received light signals individually into voltage signals. However, the problem of using this detection method are high cost and entails some complex electronic circuits involved when building a tactile array sensor. Also, in most of the medical applications using optical fibre array sensors, force information in x- and y-directions have not been addressed. This thesis proposes new low-cost tactile array sensing techniques to provide tactile information during minimally invasive surgery (MIS) in MRI.

1.2. AIM AND OBJECTIVES

Aim:

This research aims to develop tactile sensors for minimally invasive surgery. This includes tactile array force detection in z-axis and contact force detection in x- and y-directions.

Objectives:

- Investigate and develop an appropriate force sensing scheme that allows an effective tactile array sensing structure to be designed for MIS.

- Miniaturization of a disposable tactile array probe head that can be integrated with MIS instruments, and validate its usefulness of providing tactile feedback.
- Develop a two axis tactile sensor providing force information in x- and y-directions for the developed probe head.

1.3. SUMMARY OF CONTRIBUTIONS

The main contributions of the research are as follows:

- The first contribution is the creation of a tactile array system using a 2D vision system for the acquisition of sensory information from a tactile array. A mathematical model of light intensity modulation has been developed. The relation between applied force and light intensity has been analysed and applied force information can be detected by a camera through optical fibres. The camera system reduces electronic complexity which characterizes conventional intensity modulation schemes (such as photodiodes and photoresistors) and has high potential for high density tactile array sensing (see Chapter 3).
- The second contribution is the creation of a miniature tactile probe head system for palpation use during MIS in MRI. The probe has high sensitivity and spatial resolution with little crosstalk and hysteresis. Ex-vivo tests on silicone phantoms and lamb kidneys demonstrated its capability of conducting accurate and effective tissue palpation for tissue abnormality detection (see Chapter 4).

- The third contribution is the creation of a two axis ring-shaped tactile sensor system based on a geometry-based algorithm. This sensor has a similar diameter as the probe head developed in Chapter 4, equipping the tool with force measurement capabilities in x- and y-directions (see Chapter 5).

1.4. THESIS OUTLINE

An overview of each chapter of the thesis is shown in the following:

Chapter 1 describes the overview, aim and objectives, summary of contributions and the outline of this thesis.

Chapter 2 first introduces the importance of tactile sensing in robotics surgery, and then describes commonly used tactile sensing methods: piezoresistance-based, piezoelectric-based, strain gauges, capacitive-based, magnetic-based, vision-based and optical-based sensing method.

Chapter 3 presents the development of a 3 × 3 tactile sensor prototype using optical fibres. It first introduces the intensity modulation method, which is explained by a mathematical model described. The hardware and software design of the proposed sensor type is presented based on this model. After sensor calibration and hysteresis analysis, tests of static and dynamic responses together with shape detection are carried out.

Chapter 4 presents a miniaturized tactile probe head with 14 sensing elements to provide tactile information for palpation in minimally invasive surgery. It first introduces existing sensing technologies for robot-assisted palpation and their limitations. Then the chapter proposes a method which addresses these issues. By using optical fibres and acrylonitrile butadiene styrene (ABS) material for 3D printing, our tactile probe head is designed to be MRI compatible. After sensor calibration, tests of dynamic responses and shape detection are carried out. To validate the effectiveness of the proposed probe head, hard nodules are embedded in both silicone phantom and lamb kidney as tumours. The results from ex-vivo experiments show the tactile probe's effectiveness in tumour detection.

Chapter 5 presents a two axis ring-shaped tactile sensor which provides information of both magnitude of applied force and contact location. This tactile sensor is developed to equip the tactile probe in Chapter 4 with a sensation of force in x- and y-directions. First the importance of tactile information in x- and y-directions is introduced followed by the development of a mathematical model to illustrate the sensing principle of the proposed sensor. Sensor design and silicone manufacture is presented. Both the proposed sensor and the tactile probe are MRI compatible. After evaluating the relationship between displacement/angle and force/voltage, the model of force calculation based on 3 voltage outputs is established. During model validation tests, results from sensor outputs and simulation outputs are compared and analysed. Test results show that the proposed sensor has an accuracy of 83.4985% for force magnitude measurement and an average error of 10.2301 degree for contact location measurement.

Chapter 6 includes the conclusion and discussion of the thesis, together with future work illustration.

Chapter 2 Background on Tactile Sensing

This chapter first introduces the importance of tactile sensing in robotics surgery, and then provides an overview of commonly used tactile sensing methods: piezoresistance-based sensing method, piezoelectric-based sensing method, strain gauges sensing method, capacitive-based sensing method, magnetic-based sensing method, vision-based sensing method and optical-based sensing method.

2.1. ROLE OF TACTILE FEEDBACK IN ROBOTIC SURGERY

Robotics research has an increasing impact on daily life. Many robot devices have been developed to imitate human behaviour in order to collaborate with humans or conduct arduous and dangerous tasks such as industrial assembly line manufacturing [10] or bomb dismantling. Based on the International Standard Organization (ISO) in 8373, a robot is defined as “an automatically controlled, reprogrammable, multipurpose manipulator programmable in three or more axes, which may be either fixed in place or mobile for use in industrial automation applications.” With more advanced robotics technology being developed, new application areas are becoming a reality: new robot systems are introduced in the operating theatre and are capable of conducting MIS [11]. The efficacy and reliability of surgical applications have been enhanced by advanced mechanisms design, control theory and sensing technology, which were initially intended for industrial use. A successful surgical robotic system not only consists of the surgical robot itself but also of the imaging systems, visualization equipment, high-level controllers, end effecter tools, haptics controller devices, and, most importantly, the surgeon [12]. Compared to humans, a surgical robot can provide higher precision and accuracy, and can at the same time automatically carry out repetitive motions allowing the surgeon to focus on the essential aspects of the surgical task. Furthermore, modern robotic surgery tools can be designed and fabricated at a small size thus enabling surgeons to carry out minimally invasively procedures through much smaller incisions than the ones used in traditional open surgery [13].

Minimally invasive surgery is a type of surgery where the operation is performed through small incisions employing specially designed medical tools such as laparoscopic instruments or miniature manipulators [14]. The instruments usually include a viewing instrument known as an endoscopic or laparoscopic camera. During the procedure, these tools are inserted through narrow openings, anatomical openings or natural orifices, allowing the surgeon to view the inside of the patient and to conduct procedures such as suturing, ablation and generally, to manipulate the patient's organs. MIS can be performed with robot assistance due to the difficulty of handling surgical tools and the limited view of the surgical area. Master-slave configuration robots like the da Vinci system [15] have revolutionized minimally invasive surgery over the past decade. The da Vinci system consists of two main parts: robotic apparatus with manipulator arms and a control console. Also, it is the only master-slave MIS system approved by US Food and Drug Administration (FDA). Despite some controversy concerning the clear benefits of the da Vinci system, there is a clear trend towards extensive use of robotic systems in the operating theatre [11]. This is mainly due to the advantages of MIS, namely reduced pain and blood loss, decreased rates of infection, and shorter patient recovery periods as well as shorter learning curves for surgeons.

Early robotic surgery focused on orthopaedics as the shape of bones stays the same during surgery. Soft tissue surgery is comparably difficult to perform as surgical tools need to adapt to the mobility and deformability of soft tissues. There are several methods to investigate the mechanical properties of soft tissue: indentation, imaging, boundary condition methods, and mathematical modelling [12]. CT-scans taken before the operation provide the surgeon with a good view of the patient's anatomy and the target area. However, eliminating radiation exposure to patients and medics while providing much higher soft tissue details, Magnetic Resonance Imaging (MRI) has established itself as an alternative pre-operative imaging tool for operation planning. Due to the recent advances in the field of MRI scanner technology and associated MR image processing methods, MRI scanning has now real-time or near real-time capability and is suitable for intra-operative image guidance [16]. One of the main limitations of MRI scanners is that any tool to be used inside the scanner bore or in its close vicinity needs to be MR compatible [17], i.e. any instrument or device used near the scanner needs to avoid usage of magnetic material in order not to be affected by the MR signals and not to distort the images [18].

Vision and imaging, in form of internally-applied laparoscopic cameras or external imaging techniques including CT and to a lesser extent MRI, have found wide-spread application in the modern operating theatre. However, the incorporation of other sensing modalities, such as force and tactile sensing, into medical devices and as a means to provide the surgeon with relevant information about the surgical site has been neglected. Signals from force and tactile sensors, especially in combination with visual information [19], are considered a powerful method to provide the surgeon with a better insight into and assessment of the geometrical and mechanical properties of the patient's organs, such as shape, friction and stiffness.

2.2. TACTILE SENSING METHODS

Based on [4] “any device which senses information such as shape, texture, softness, temperature, vibration or shear and normal forces, by physical contact or touch, can be termed a tactile sensor”. The ultimate goal for a tactile sensor is, to achieve the function of human skin, which is distributed all over the human body and consists of four types of tactile receptors which are: Pacinian corpuscles, Ruffini endings, Merkel cells and Meissner corpuscles [20]. Different from traditional force and torque sensors, tactile sensors give more information than only measuring the total force due to the contact with object. A tactile sensor can not only measure the spatial distribution of force to an area, but is also capable of interpreting the corresponding information when in contact with an object.

The tactile sensing plays an important role in various applications over many areas. With tactile sensors embedded [21], the industrial assembly line can make flawless assembly and precise part fitting possible. For the dexterous robotic hand with multi-fingers, tactile sensors are needed on its fingertips and palm [22] [23] to convey the contact force and position of the objects, thus making grasping and manipulation possible. Other than putting force sensors only on the hand, researchers have tried to equip the whole robot skin with high resolution tactile sensors [24]. In the medical field, such as MIS in which the operation is carried through a small incision, a force sensor embedded on the tip of surgical tools could help the surgeon gain a better understanding of how much force has been applied on the tissue during the operation without damaging it.

Research has been conducted by John Hopkins University [25] on the comparison of human and robotic tactile sensing for lumps detection in soft tissue. A standard tactile sensor and human index finger are placed on a platform to perform passive palpation tasks. The platform consists of a vertical actuator, force sensor, gripper and a soft tissue model with a lump embedded, shown in Figure 2-1. Test results show that the tactile sensor outperforms the human finger in palpation tasks with lower indentation depths and lower pressures applied. Also similar work has been done by Liu and Li [26].

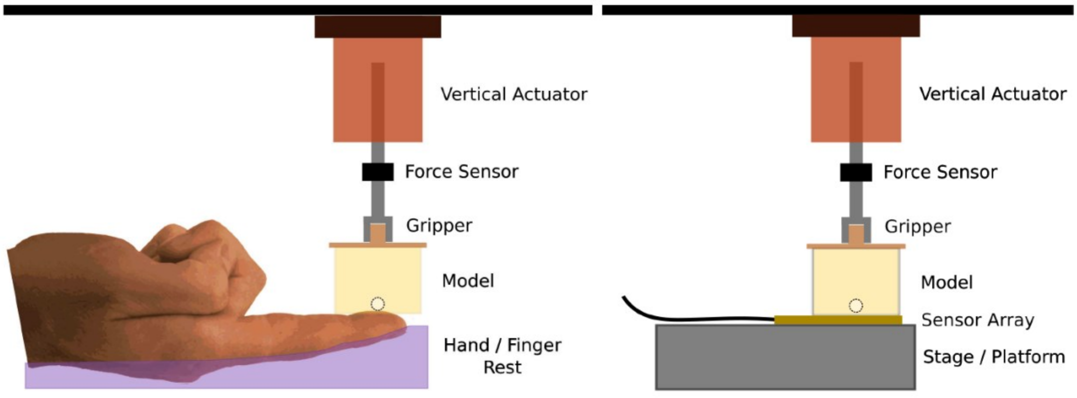

(a) (b)

Figure 2-1 Experimental setup for lump detection by: (a) human finger, (b) tactile array sensor [25].

Research into tactile sensing reaches nearly as far back as research into vision, but has developed at a lower rate [27]. The main reasons for this are that the tactile sensors have to be in physical contact with the probed object all the time in order to perceive tactile information. In addition, the acquisition of force and tactile sensor data is generally complex with numerous design requirements for the sensor, which needs to be capable of robustly acquiring sensor information during repeated physical interaction with objects [28].

There are many non-medical application fields where a tactile sensor can play an important role in. The most popular one would be the touch screen [29] on smart phones or touch pads, which falls into the category of human-machine interface. In robotic applications, the two main research areas for tactile sensors are lifting/grasping/re-grasping objects and characterizing surface textures. Tactile sensors are gradually becoming popular in hospitals, such as in minimally invasive and remote surgeries, and tissue characterization [30] [31]. There are a number of force sensing methods [32] [33] [34] that have been incorporated in tactile sensing systems.

2.2.1. PIEZORESISTIVE-BASED SENSING

Piezoresistive-based sensing is based on Ohm's Law, and the magnitude of the force is a function of the measured resistance value [35] [36] [37]. This method can be described as

$$V = IR \, , \tag{2.1}$$

where V is the voltage, I is the current and R is the electrical resistance. In principle this method works by fixing the voltage/current and calculating the change of resistance by monitoring the change of current/voltage. Normally, the sensor contains a conductive material which is also pressure sensitive between or in touch with two electrodes (Figure 2-2 taken from [38]). The conductive material is usually conductive rubber, foam or ink laid in a mesh configuration.

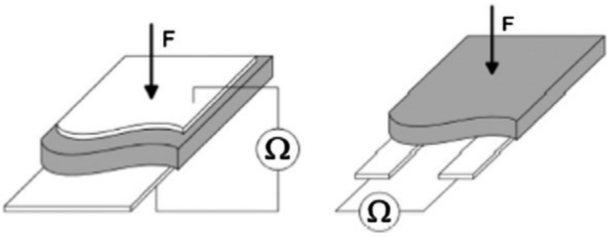

Figure 2-2 Resistive tactile sensors [38].

Wettels *et al.* [39] developed a robust tactile sensor array using piezoresistive-based sensing method with conductive fluid, shown in Figure 2-3. The system mainly consists of a rigid core, conductive fluids, electrodes and elastomeric skin. When force is applied on the deformable skin, the fluid path of conductive fluid around the electrodes changes. The resistance of electrode is determined by the thickness of conductive fluid between electrode and skin, thus the change of fluid path will cause the change of the distributed pattern of electrode resistance. These changes contain information regarding the point of contact, force magnitude and direction. Spatial resolution and frequency response are limited by the viscoelastic properties of the elastomeric skin [40].

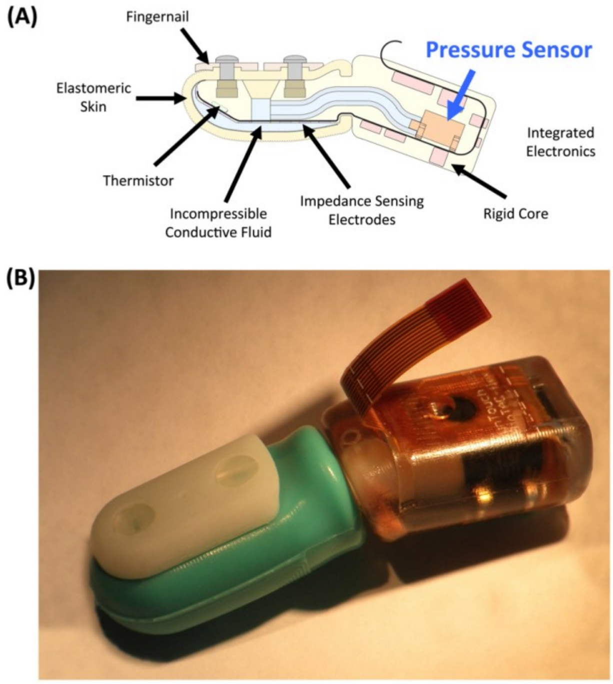

Figure 2-3 (A) Cross-sectional drawing of BioTac showing various components used for each sensing modality. (B) Photo of an assembled BioTac [41].

Another commercial tactile sensor using piezoresistive-based sensing method is developed by the company Tekscan [22], shown in Figure 2-4. It consists of two thin polyster sheets attached to each other in the non-sensing area. The conductive traces which are placed to form a grid in the sensing area are covered by semi conductive ink. Each cross section of the grid in the sensing area is an individual force sensor at the spatial resolution of 0.5 mm.

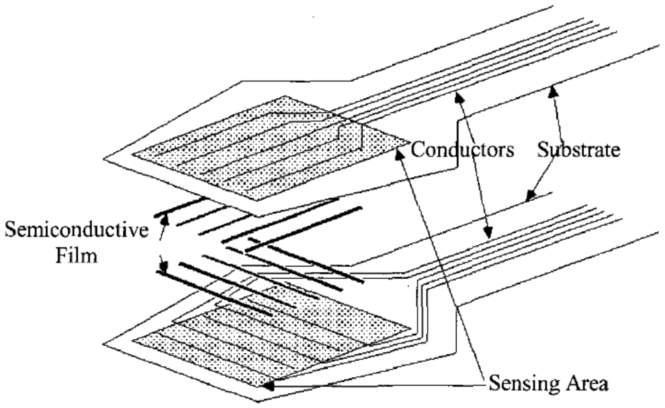

Figure 2-4 Tekscan resistive sensor [22].

Resistive based sensing requires few electronic components and is easy to manufacture at a small scale. However, it is sensitive to temperature variations and suffers from hysteresis effect. Although it is less susceptible to noise, its relatively low precision and has a limited use.

2.2.2. PIEZOELECTRIC-BASED SENSING

Piezoelectric-based sensing makes use of the piezoelectric effect (electricity generated by pressure) to measure force and acceleration [42] [43] [44]. Some materials such as certain crystals, ceramics and polymers have this piezoelectric effect. Polymer polyvinylidene fluoride (PVDF) is mostly used in many measurement tasks.

Dargahi *et al.* [45] developed a piezoelectric tactile sensor which can be integrated with commercial endoscopic graspers. The sensor consists of three layers: a tooth-like silicone on top, PDVF electrodes and film in between and a Plexiglass substrate at the bottom, shown in Figure 2-5. When a force is applied on the silicon, it will cause a polarization charge in the PVDF. The magnitude of the force can be determined by the amplitude of the signal and the contact point can be identified by comparing the slope of the signals between four electrodes. The sensor is easy to fabricate and demonstrates small crosstalk issues as there are only four outputs.

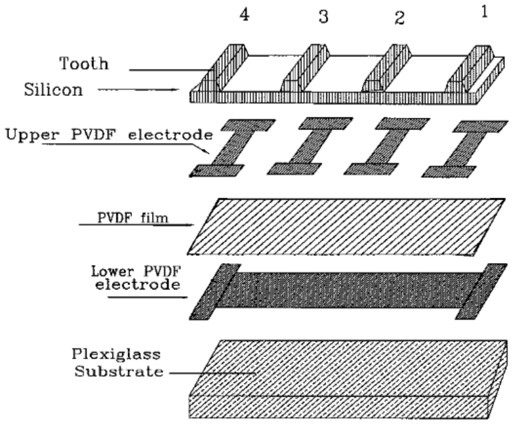

Figure 2-5 Different layer of the tactile sensor [45].

Chuang *et al.* [46] introduced structural electrodes on the sensing material in order to improve the sensitivity of the traditional piezoelectric tactile sensor, shown in Figure 2-6. A traditional PVDF-based tactile sensor usually has a sandwich structure: the piezoelectric thin film made of PVDF is placed between two soft substrates made of Polystyrene. By adding a Polydimethylsiloxane (PDMS) microstructures array, contact force is transmitted through the PDMS rather than through direct contact with the sensing material. The reduced contact area makes for an increase of the induced charge of the piezoelectric material. Chuang et al. claim that the sensitivity is increased by 30%.

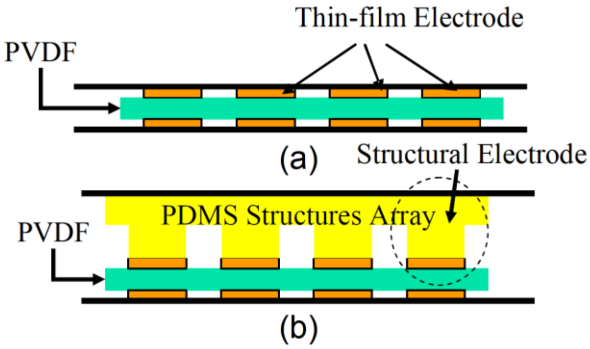

Figure 2-6 Cross-sectional structure of (a) traditional PVDF-based tactile sensor with thin-film electrode array; (b) new type of PVDF-based tactile sensor with structural electrode by adding a layer of PDMS microstructures array [46].

The piezoelectric-based sensing method exhibits excellent high frequency responses, which make it suitable for vibration measurement. Its feature of nearly zero deflection has brought it into widespread industrial use; however, it is not suitable for static measurements [47].

2.2.3. STRAIN GAUGES

Strain gauge sensing has been widely used in many applications, such as stress analysis and durability testing [48] [49] [50]. It measures force by translating the strain of the sensor structure caused by an applied force into electrical resistance.

Hwang *et al.* [51] developed a flexible 8 × 8 tactile sensor with a size of $35 \times 35\ mm^2$ and a thickness of 70 μm by using strain gauges, shown in Figure 2-7. Each sensing unit consists of four strain gauges for normal and shear load detections in the x- and y-directions. The substrates will deform when force is applied on the sensor, and induce strains on all four strain gauges. If the four strains are equal, then it is a normal force which causes only tensile stress. If not, it is the shear force which contributes to both tensile and compressive stress. The normal/shear force can then be determined by calculating these outputs from four strain gauges.

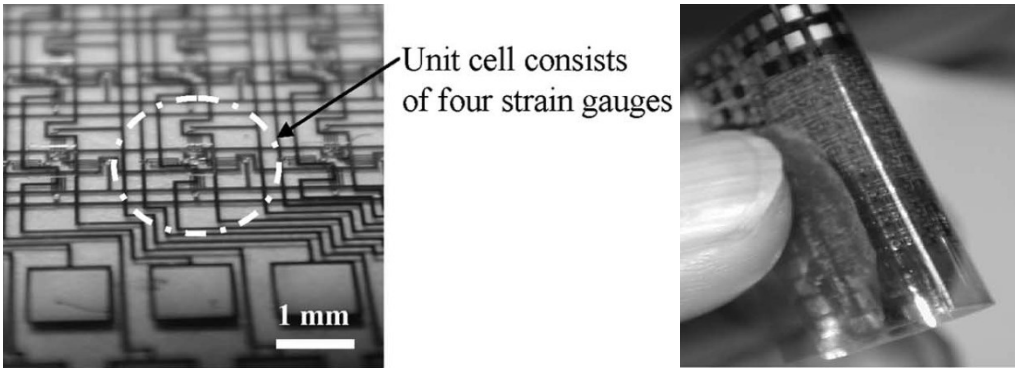

(a) (b)

Figure 2-7 Photo of flexible tactile sensor. (a) One sensing unit. (b) The flexible sensor array [51].

Strain gauges are very sensitive and has been used in the market for so long that its usefulness has been well established. However, it is sensitive to temperature and has high hysteresis, and cannot be recovered once overloaded.

2.2.4. CAPACITIVE-BASED SENSING

Capacitive-based sensing is widely used at present due to its low cost, easy fabrication and insensitivity to high temperature [52] [53] [54]. The operation principle of this sensor is a capacitance change in accordance to either the distance between the two capacitor plates or the amount of overlap between them. The equation to calculate capacitance is

$$C = \frac{A\varepsilon_0\varepsilon_r}{d_c}, \tag{2.2}$$

where C is the capacitance, A is the size of overlap area between two plates, ε_0 is the permittivity of free space and ε_r is the relative permittivity of dielectric material, d_c is the distance between two plates.

One of the commercial capacitive-based tactile sensors is RoboTouch, shown in Figure 2-8 (a) from pressure profile systems (PPS) [55]. It consists of 20-24 sensing elements with the size of 25 – 100 mm each. The whole set includes: an interface module, a USB Bluetooth adapter and an expansion board, shown in Figure 2-8. The PPS sensor is using Chameleon software to run three sensors at the same time. Data from each sensor is available in direct format via USB using PPS' interface electronics. The pressure range is 0 – 20 psi and the sensitivity is 0.1 psi, with a sample rate is 35 Hz.

Figure 2-8 PPS sensor on the finger of Barrett Hand [55].

Lee *et al.* [56] presented a flexible capacitive tactile array sensor which is capable of measuring both normal and shear force. This tactile sensor is an 8 × 8 array with the size of 22 × 22 mm, the size of each sensing cell is 2 × 2 mm, shown in Figure 2-9 (a) (b). Each cell consists of four electrodes, an air gap and a pillar between two thick PDMS layers. The capacitance will change when force is applied on the bump causing the air gap to deform. If it is a normal force, the air gap between top and bottom electrodes will decrease and all four capacitances will increase. A shear force will result in two increased capacitances and two decreased capacitances. The sensing range of one single sensor is 0-10 mN and the sensitivities in x-, y-, and z-directions are 2.5%/mN, 3.0%/mN, and 2.9%/mN respectively. The issue of crosstalk between each cell, however, is not addressed.

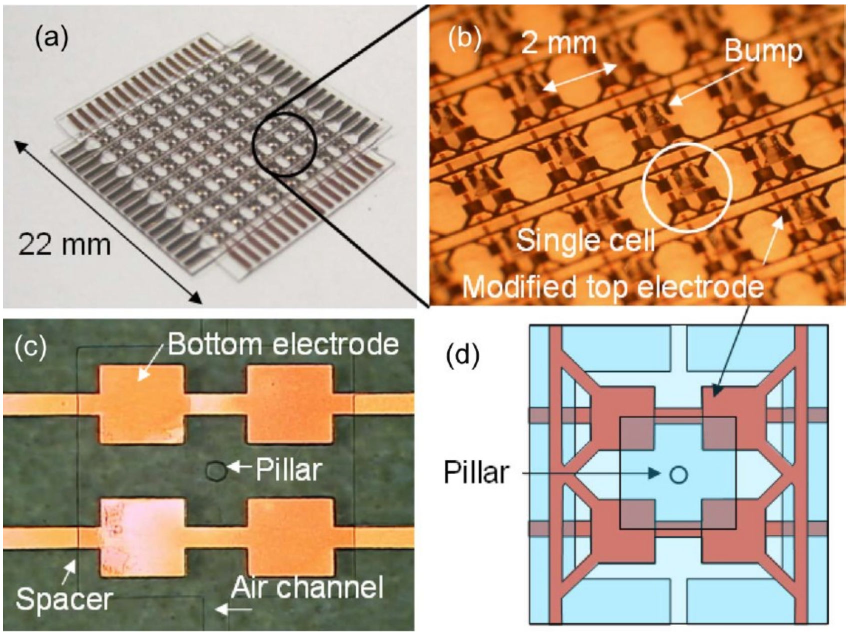

Figure 2-9 Photo of the three-axis capacitive tactile sensor (a) 8 × 8 tactile array, (b) close view of sensing cells, (c) structure of a single cell, (d) top electrode pattern illustrating the sensing principle [56].

Though the capacitive-based sensing provides good frequency response and large dynamic range, it suffers from sudden electrostatic discharge introducing noise which requires complex electronics to filter out. Also there is the likelihood that the discharge damages other electronic components in the vicinity.

2.2.5. MAGNETIC-BASED SENSING

Magnetic-based sensing involves the use of on magneto-elastic materials [57] [58], which affect the magnetic transduction by the movement of a magnet or deformation of the core of a transformer or inductor caused by an applied force. To measure the magnetic flux, devices with force dependent magnetic properties are used (e.g. magneto-resistance). Then force is calculated by the detection of the inductor's electrical parameters change (e.g. voltage, current) [59].

Takenawa [60] proposed a soft three-axis tactile sensor based on the magnetic sensing method, shown in Figure 2-10. A permanent magnet is embedded in an elastic medium located on a rigid substrate. Inductors are placed under the magnet and substrate generating individual induction voltage in response to the movement of the permanent magnet caused by the loaded force and deformation of elastic medium. The sensor utilized four inductors in a way that it is able to detect both vertical and tangential force.

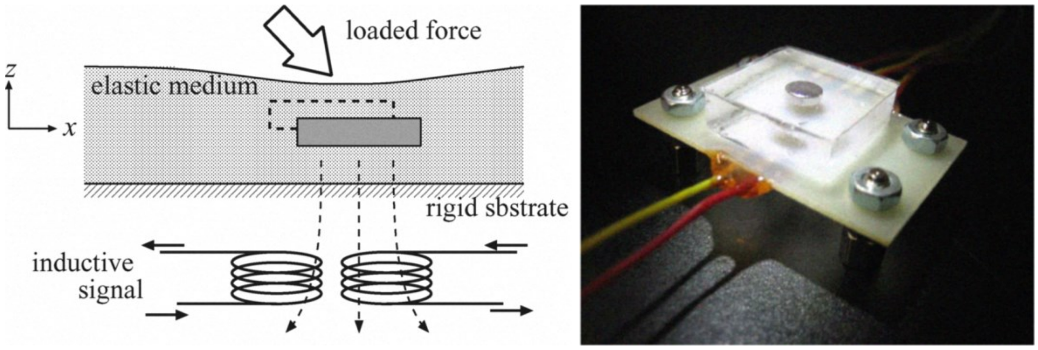

Figure 2-10 Proposed magnetic-based sensor: (a) sensing principle, (b) photo of sensor prototype. [60].

Magnetic-based sensing is physically robust with virtually no mechanical hysteresis [61]. However, it has low repeatability, is bulky in size, and requires more complex electronics than normal resistive tactile sensors, making it unsuitable for tactile array sensors.

2.2.6. VISION-BASED SENSING

Vision-based sensing [62] [63] has caught many researchers’ interest due to the availability of well-established computer vision systems and techniques [64]. Vision-based tactile sensing systems make use of small-sized cameras integrated within the tip of the probing tool and allow force or stiffness detecting via image processing [65] [66].

Kamiyama *et al.* developed a vision-based sensor for measuring surface traction fields called Gelforce technology, shown in Figure 2-11 [67]. When force is applied on the transparent elastic body, the movement of both blue and red markers in two layers is captured by a CCD (charge-coupled device) camera. This technology is capable of detecting force magnitude, distribution and vector by calculating the movement and displacement change between blue and red markers.

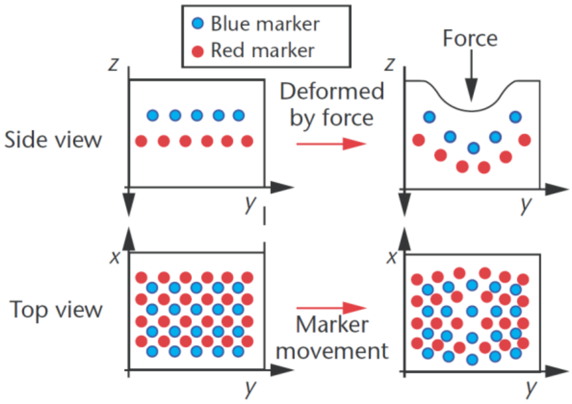

Figure 2-11 Illustration of markers movements caused by force applied on the elastic body [67].

Based on Gelforce technology [68], Sato *et al.* developed a vision-based finger-shaped tactile sensor which enables robot arms to perform grasping tasks [69]. As shown in Figure 2-12, both blue and red markers are distributed according to the shape of a fingertip instead of a flat surface. A wide-angle lens CCD camera is attached to the plastic base of a robot hand to capture the movement of all markers. The surface of the sensor is covered by a black sheet of silicone rubber to block out light noise from the outside environment. The total size of this finger-shaped tactile sensor is $18\times23\times36\ mm^3$, which is close to the size of a real human finger.

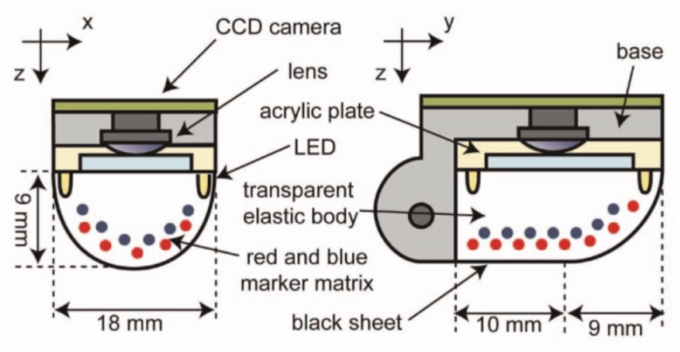

Figure 2-12 Configuration diagram of the finger-shaped vision-based sensor [69].

However, vision-based sensing involves considerable computational complexity and could be widely used if its precision was increased.

2.2.7. OPTICAL-BASED SENSING

Fibre optic-based sensing [70] [71] [72] is an area of great interest, as it allows the creation of small-sized and light-weight sensors, capable of operating in harsh environments. In addition, sensors based on this principle can be used in MR scanners. In the four main types of fibre optics sensing approaches currently employed the modulation of the sensor signal is based on the wavelength, the phase, the polarization and the intensity. Fibre Bragg gratings (FBG) sensor [73], the most commonly used wavelength modulated sensor, reflects light of a particular wavelength depending on the placing of a periodic variation of the refractive index within a fibre core. It is sensitive to temperature and the associated measurement system may be expensive or complex. Using phase modulation, applied forces are determined interferometerically by comparing the phase of a signal fibre and reference fibre using an interferometer, such as those based on Mach-Zehnder and Fabry-Perot principles [74]. This approach is usually highly sensitive and accurate; however, sophisticated manufacturing is required to build the sensor system in its entirety. The main types of polarization-based sensing [75] include linear, elliptical and circular polarization methods. The output signal is detected by the polarization state change due to stress or strain. Polarization modulated sensors are usually more expensive and difficult to use compared to other sensor types. Intensity modulated sensors make use of the light intensity which is altered depending on the reflection, transmission or micro fibre bend which in turn is affected by the magnitude of the causing variable, such as applied force. Its versatility, simple design, inexpensiveness and insensitiveness to temperature changes make it a strong contender for many applications.

Yussof *et al.* [76] developed an optical three-axis tactile sensor based on the optical waveguide transduction method, shown in Figure 2-13. This sensor is mounted on a robot hand to improve the sensitivity of the robot hand system by providing tactile feedback for actuators. The system consists of a light source, a fibre scope, a CCD camera and 41 sensing elements made of silicone rubber. When force is applied on the sensing elements, the rubber will come in contact with the acrylic dome causing light to diffuse as the rubber has a higher reflective index. The diffused light, which appears as bright spots, is captured by the optical fibre scope connected to the CCD camera as image data. This data is then processed by the computer to provide information on the contact force.

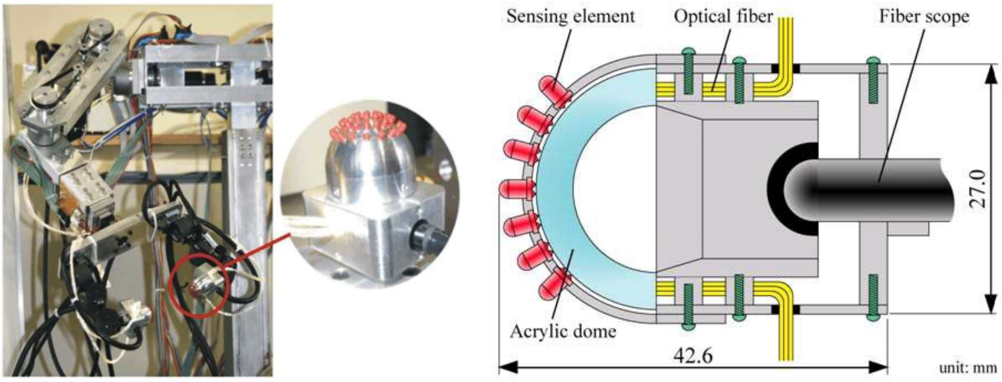

Figure 2-13 (a) Optical three-axis tactile sensor mounted on robot arm, (b) hardware structure of the proposed sensor [76].

Heo *et al.* [77] developed two types of flexible tactile sensor arrays based on FBG method, shown in Figure 2-14: the first is a large area sensor which has a low spatial resolution (25 mm), while the other one provides a better spatial resolution (5 mm). The first one is designed in a diaphragm type and the second one is a bridge type. 9 FBGs with their own Bragg wavelengths are embedded in a sensor array, with each FBG generating different peak points detected by a photodiode. The signal is measured by Fabry-Perot filter, interfaced with LabVIEW to calculate the applied force information.

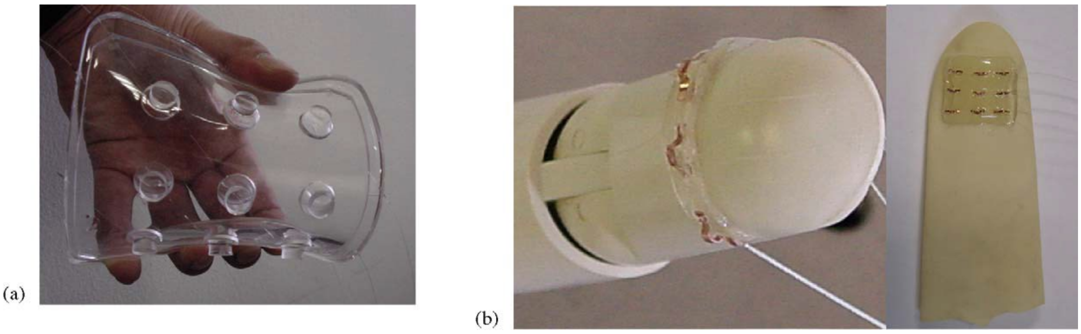

Figure 2-14 Flexible FBG tactile sensor: (a) diaphragm type, (b) bridge type [78].

2.3. CONCLUSION

To sum up, several main sensing methods have been explored in the literature. Piezoresistive based sensing needs few electronic components and easy to fabricate, however, it is sensitive to temperature variations as well as hysteresis effect. Piezoelectric based sensing is not suitable for static measurements. Strain gauge is a direct measurement method but there is a trade-off between sensitivity and stiffness of the structure. Capacitive based suffers from sudden electrostatic discharge introducing noise, required complex electronics to filter out. The physically robust magnetic based sensing is bulky in size with low repeatability. Vision based sensing requires complex image processing technique and the sensor size is limited by the size of the camera.

More importantly, in MRI environment, none of these sensing methods above can be employed as they all involve metallic components which will distort MR images and be disturbed by the MR environment. Optical based sensing is one of the few methods that can be applied [14] as it requires no metallic parts for sensing. Also, its nature of low cost, small in size, lightweight, water and corrosion resistant makes it suitable for MIS applications.

Chapter 3 MR-Compatible Tactile Array Sensor using Optical Fibres and 2D Vision Sensor

This chapter presents the development of a 3 × 3 tactile sensor prototype using optical fibres. It first introduces intensity modulation method, and then describes a mathematical model to further explain this method. Based on the model, hardware and software designs of the proposed sensor type are developed. After sensor calibration and hysteresis analysis, tests of static and dynamic responses together with shape detection are carried out.

3.1. INTRODUCTION TO LIGHT INTENSITY MODULATION

Previous work on intensity modulated fibre optic sensors uses a pair of parallel optical fibres [79] with one projecting light into the other fibre via a reflecting surface. Once the distance between the fibres and the surface changed in response to external environment changes, the variation of the light intensity received will be detected to measure the related physical factor, such as force. The use of a coupler to couple two individual fibres into one single fibre [80] is one of the popular ways to design a fibre optic sensor. In such a design, the light is transmitted and received in the same fibre thus more light can be collected compared to parallel displaced fibre optic sensors. The disadvantage of using a coupler is the high cost and manufacturing difficulties in displacing the fibres and connecting them. Another approach is using a pair of bent-tip optical fibres [81] to augment the performance by avoiding the loss of light during transmitting and receiving in the transduction procedure. The comparison of bent-tip optical fibres and parallel optical fibres has been presented by Puangmali [82], in which force is calibrated by voltage generated from the light intensity through an optoelectronic circuit. Puangmali et al. conclude that bent-tip optical fibres are more sensitive than parallel displaced optical fibres whether laterally or longitudinally moving and provide a wider working range. However, this approach suffers from light loss caused by fibre tip bending. The approach adopted for the tactile sensor presented in this chapter took advantage of the bent-tip method to reduce light loss during transmitting and receiving, together with no light loss caused by fibre tip bending thanks to the microstructure of parallel fibres and mirror system, as shown in Figure 3-1.

The aim is to create a general-purpose tactile array sensor that can be employed in the MR environment to obtain organ properties that cannot be estimated using vision only. Acknowledging the potential of intra-operative MR imaging, a force sensing paradigm based on fibre optics and the principles of light modulation and capable of augmenting images from MR scanners is proposed. This approach requires a complete design of the sensor system to ensure appropriate miniaturisation and MR compatibility. Commercial tactile and force sensors, such as the PPS TactArray and ATI Nano17, are not suitable because they are not MRI compatible.

MRI has become popular in many areas, ranging from medical surgery to brain science due to its advantage of being non-invasive and providing high resolution images [83]. Compared to the conventional imaging method, CT, MRI emits lower radiation thus it is a safer method to use for both patients and doctors. In the medical field, the MR scanner mainly functions as a diagnostic equipment of automatic palpation and elasticity quantification in deep tissues [84]. Nevertheless, the lack of force feedback limits its usefulness in detection of abnormal tissues whose stiffness is higher than that of their surrounding tissues. For brain research, functional MRI (fMRI) in conjunction with haptics interface has become an important tool to enable neuroscientists to investigate brain functions [85].

As MR compatible surgical-assist robots [86] are more frequently used in hospitals, efficiency and safety during operation can be significantly improved by providing force feedback to the surgeons [87]. However, MRI requires homogeneous and high static magnetic field together with strong RF pulse generated by the MR scanner. Thus the sensors need to be electromagnetically compatible so as not to distort MR images and stay undisturbed by the MR environment. Thus most of the conventional force sensors, such as resistive-based and capacitive-based sensors, are not suitable for use in an MRI environment. Piezoelectric-based sensing [88] is one of the MR compatible sensing method. However, it is only sensitive to time-varying forces and lacks multi-axis measurement capabilities.

This chapter introduces a novel, MRI compatible, fibre optic tactile sensing concept employing a 2D vision system for the acquisition of force information. The actual sensing elements at the tip are envisaged to contain an array of 3 × 3 force sensing tactels integrated with hand-held laparoscopic tools or remotely-operated surgical manipulators and to provide tactile information from the surface of probed organs, in particular soft-tissue organs. The schematic design of the presented sensor is shown in Figure 3-1. Aspects related to the design and fabrication of the array sensor will be addressed and tactile sensor signal acquisition will be investigated.

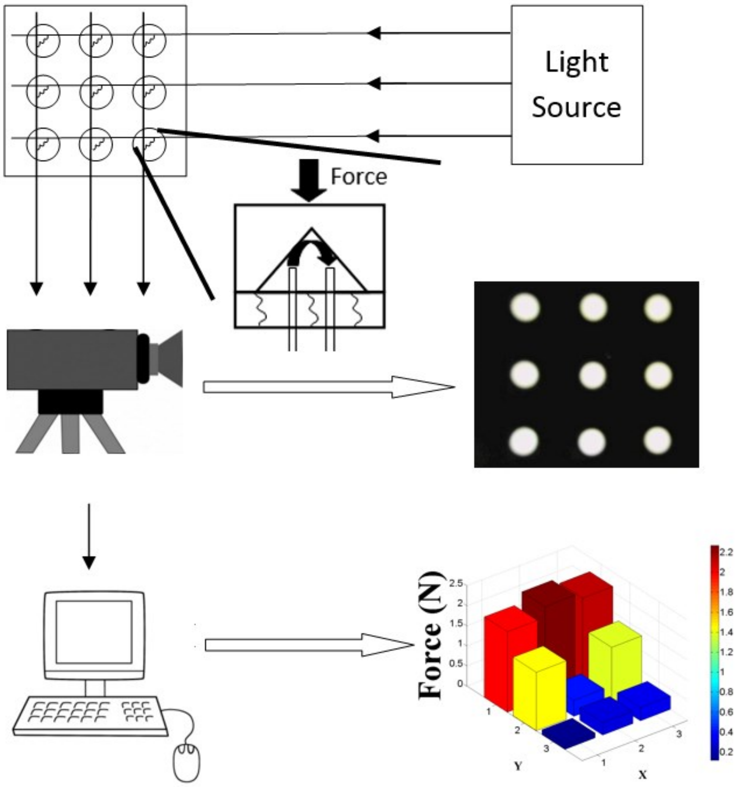

Figure 3-1 Schematic of light intensity based tactile force sensor using camera.

3.2. MATHEMATICAL MODEL

A geometrical representation of the light intensity modulation fibre optic based mechanism is shown in Figure 3-2. Two fibres (a transmission fibre and a receiving fibre) distance d apart, face a 90° double-mirror assembly at an angle of $\theta = 45°$ with regards to the mirror. Virtual transmitting and receiving fibres are introduced to simplify the mathematical derivations; however, the light path between the virtual fibres is exactly the same as between the real fibres, assuming that the employed mirrors are perfectly reflecting the transmitted light. All fibres have the same diameter, D.

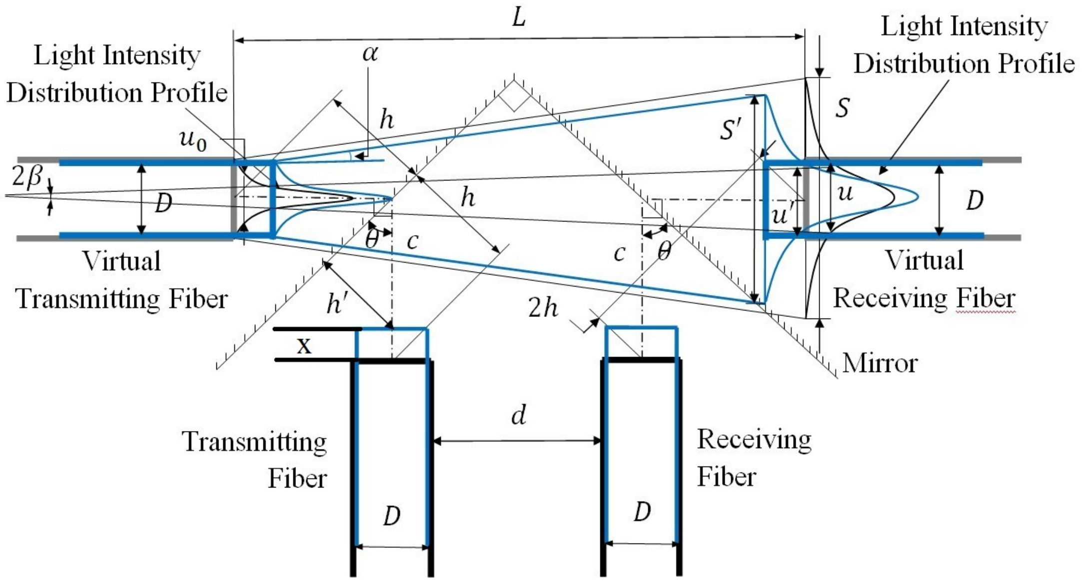

Figure 3-2 Geometry of the light intensity modulation mechanism using prismatic mirror and a pair of parallel optical fibre.

The shortest distance between the centre of the fibre and the mirror is h. The virtual fibres are facing each other directly and their tips are distance L apart, i.e. the length of the light path between the tips of the real fibres is the same as the length of the light path between the virtual fibres,

$$L=\frac{2h}{\sin\theta}+D+d, \tag{3.1}$$

where D is 1 mm and d is 2 mm. The light transmitted to the receiving fibre (virtual and real) has a projection diameter S,

$$S=2\cdot L\cdot tan\alpha+D=2tan\alpha\left(\frac{2h}{\sin\theta}+D+d\right)+D, \tag{3.2}$$

where α is the radiation angle. S is the maximum projection diameter. When a force is applied, the mirror shifts downwards by distance x: this is equivalent to the transmitting and receiving fibres shifting upwards by the same distance of x, also shown in Figure 3-2. Hence, the projection diameter is changing to

$$S' = 2tan\alpha\left(\frac{2h'}{\sin\theta} + D + d\right) + D$$

$$= 2tan\alpha\left[\frac{2(h - x\cdot\cos\theta)}{\sin\theta} + D + d\right] + D. \tag{3.3}$$

The Gaussian form of the light intensity distribution model proposed in [89] is used for this sensor design, and modelled as follows:

$$I_{(r)} = I_o e^{(-\frac{2r^2}{{w_o}^2})}, \tag{3.4}$$

where r is the light beam's radial distance, $I_{(r)}$ is the intensity of the beam, I_o is the beam's maximum intensity and w_o is the mode-field radius, the Gaussian width of the light transmitted out of the fibre, which is a constant parameter close to $0.4D$ [82].

There is no boundary on the Gaussian curve and the light is theoretically distributed up to infinity, so it is assumed that the mode-field diameter is the boundary for calculation. Then the total light flux of the virtually transmitting fibre can be estimated as

$$\Phi_{VT} = \int_0^{\frac{S}{2}} I_{(r)} 2\pi r dr \approx \int_0^{\infty} I_o e^{(-\frac{2r^2}{{w_0}^2})} 2\pi r dr = \frac{I_o \pi {w_o}^2}{4}, \tag{3.5}$$

where Φ_{VT} is the total virtually transmitted light flux. When distance S decreases, the light intensity I increases, while the total light flux stays the same. The change of light intensity is in accordance with mode-field radius w_o. Further explanation is demonstrated in Figure 3-3: by defining I_o' and ΔI_o as the maximum intensity of the light projected at the tip of the virtual transmitting fibre and the variation of maximum light intensity between virtual transmitting and receiving fibres, we obtain the following relations:

$$\Delta I_o = I_o' - I_o = \frac{4\Phi_{VT}}{\pi {w_o}^2} - \frac{4\Phi_{VT}}{\pi w^2} = \frac{4\Phi_{VT}}{\pi}\left(\frac{1}{{w_o}^2} - \frac{1}{w^2}\right), \tag{3.6}$$

where

$$w = \left[\frac{2(\mathrm{h} - \mathrm{x} \cdot \cos\theta)}{\sin\theta} + \mathrm{D} + \mathrm{d}\right] \tan\beta + w_{\mathrm{o}}, \tag{3.7}$$

and where β is the divergence angle which is 3.56º. It is noted that the light flux transmitted to the receiving fibre is the light in the circular area with diameter d, which is the size of the receiving fibre, not the total light flux Φ_{VT}.

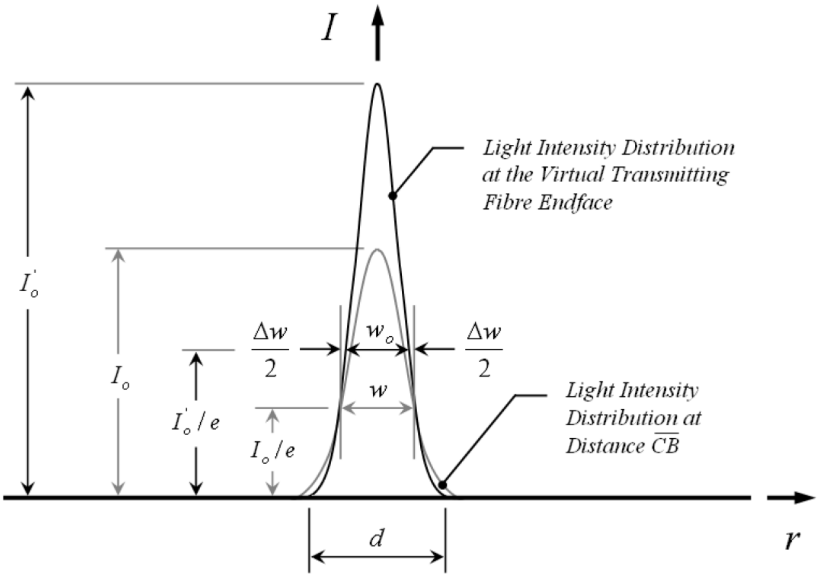

Figure 3-3 Comparison of light intensity distribution profiles [82].

Then the maximum light flux collected by the receiving fibre can be calculated as

$$\Phi_r = \int_0^{\frac{d}{2}} I_{(r)} 2\pi r dr = \frac{I_0 \pi w^2 (1 - e^{-\frac{D^2}{2w^2}})}{2}, \tag{3.8}$$

where Φ_r is the receiving fibre's maximum collected light flux as the minimum distance between optical fibre and reflective surface. Therefore, the light information "seen" at the site of the camera placed at the end of receiving fibre is

$$N = k\Phi_r = \frac{k I_0 \pi w^2 (1 - e^{-\frac{D^2}{2w^2}})}{2}, \tag{3.9}$$

where N is the number of the activated pixels in the sensing area, k is the conversion factor that relates the light flux to the number of activated pixels; hence, we call our approach pixel-based force sensing method. The normalized output can be represented as the ratio between the numerical value and its maximum value N_{max} as follows:

$$\frac{N}{N_{max}} = \frac{\frac{k I_0 \pi w^2 (1 - e^{-\frac{D^2}{2w^2}})}{2}}{max\left[\frac{k I_0 \pi w^2 (1 - e^{-\frac{D^2}{2w^2}})}{2}\right]}. \tag{3.10}$$

Two optical fibres (core diameter 1mm, reflective index 1.49 and numerical aperture 0.53) are placed parallel to each other and with a distance of 2 mm between them - one for transmitting light from a 4 Watt LED torch and the other for receiving light that is coupled into a Microsoft VX-800 camera. The 90° double-mirror attached to an ABS (acrylonitrile butadiene styrene) support is mounted on a linear motion platform. The test is conducted 3 times and the responses from the camera are recorded corresponding to the distance change between mirror and fibre at increments of 0.1 mm from 0 to 1.7 mm. A comparison of experimental data and simulated curve is shown in Figure 3-4.

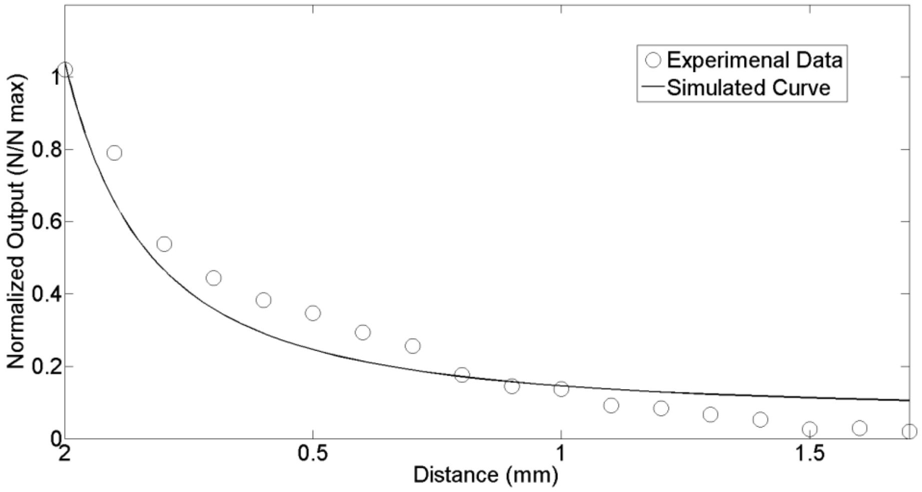

Figure 3-4 Normalized experimental data and output from light intensity modulation model (the simulated curve was calculated using Equation 3.10 with model constant k=1.94 × 10^8).

3.3. SENSOR DESIGN

A 3 × 3 tactile sensor is built based on the principle of light intensity modulation. The main structure of a fibre optic force sensor includes light source, transduction element and optical detector. Existing intensity modulation fibre optic sensors [9] are mostly based on a set of optoelectronics, where each optoelectronic receiver (consisting of a photodiode, photoresistor or phototransistor and a signal conditioning circuit) converts the received individual light signals into voltage signals. It provides a sensitive response with low noise but is limited to high resolution tactile arrays as the high cost and complexity of detection electronic circuits. To overcome this problem, a fibre optic sensor employing a 2D vision sensor (camera system) has been developed. The developed sensor is different from previously described vision-based sensors in that it uses a vision sensor to detect only the light intensity at the end of a receiving fibre rather than attaching it to the sensing tip. Thus, it achieves simplicity, high resolution and low cost in one go.

3.3.1. SENSOR HARDWARE

The tactile sensor structure was developed in SolidWorks based on the schematic design in Figure 3-5 and printed by a rapid prototyping machine using ABS as shown in Figure 3-6. On top of the supporting material, silicone made of RTV6166 (General Electric Corp., CT, US) (ratio: 30/70, density: 1100 kg/ m^3 , attenuation: 3.45Np/m/MHz, Young's modulus: 15.3 kPa [90] [91]) is used as the flexible structure. Its thickness decreases when forces are applied. The contact area used by the sensor to detect applied forces is a cylinder-like sensing element; inside the contact area two mirrors are placed at a 45 degree angle to reflect light as introduced in the mathematical model section. As the sensor is designed to detect z-axis force information, any x and y movements which would affect the sensor performance should be avoided. In this case, a top layer was designed to restrict the x and y movements of the sensing elements.

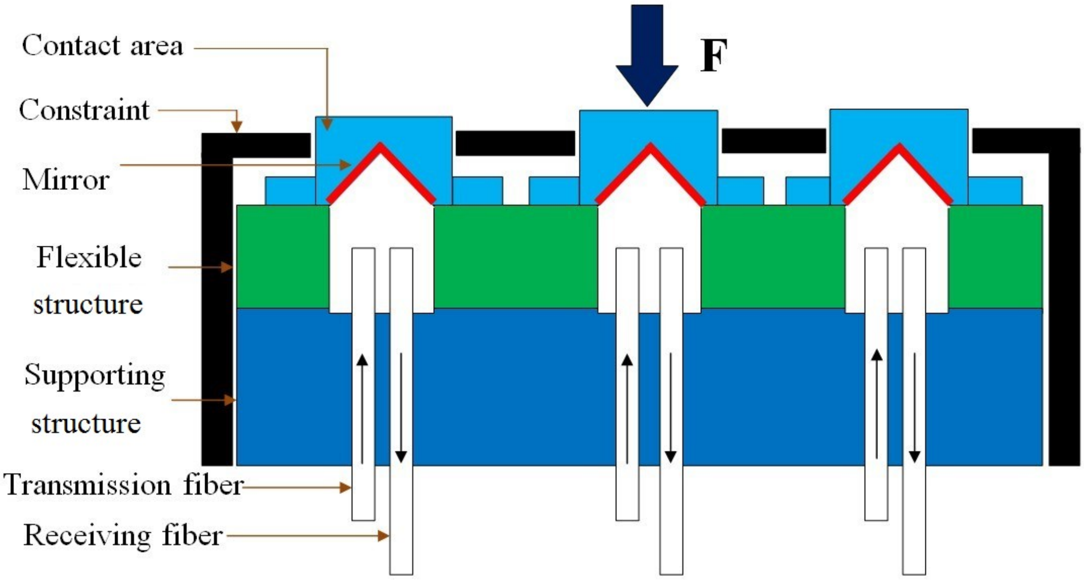

Figure 3-5 Design of the tactile sensor with mirror displacement.

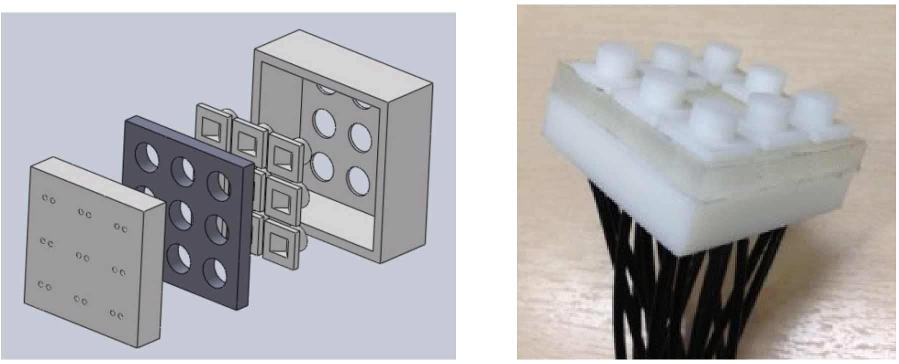

(a) (b)

Figure 3-6 (a) SolidWorks drawing of the sensor, (b) sensor tip without constraint.

3.3.2. SENSOR SOFTWARE

The change of light intensity of each reflected fibre is used to determine the force applied to the sensor array. The methodology in Figure 3-7 illustrates the sequence followed from capturing the real-time image to finally deriving the amount of force. The algorithm is implemented in a Simulink/MATLAB model which follows the routine detailed below:

1. Capturing the real-time video images.
2. The RGB image is transformed into a greyscale image. The following equation was used in the algorithm to convert the intensity image from the three layered RGB image enabling the detection of light changes:

   $$I = 0.2989\,R + 0.5870\,G + 0.1140\,B. \tag{3.11}$$

   where I is the light intensity, R, G and B represents red, green and blue value of each pixel.
3. The intensity image is then transferred to a binary image using a sufficient threshold which is calculated by the algorithm to eliminate the light noise from the outside environment.

   $$n_i = \begin{cases} 0, I_i < I_{threshold} \\ 1, I_i > I_{threshold} \end{cases}, \tag{3.12}$$

   where n is the numerical value of each pixel, $I_{threshold}$ is the defined intensity threshold to eliminate ineffective pixels.
4. As the tactile array sensor contains different force information for specific areas of the sensor, the real-time video data is divided into 9 parts, each representing one sensing element, shown in Figure 3-8.
5. The quantity of black and white pixels detected for each section is calculated:

$$N = \sum_{i=1}^{K} n_i, \tag{3.13}$$

where N and K are the total numerical value and total number of the pixels in each sensing area.

6. Via a calibration algorithm which is introduced in the following section, the force information applied on each sensing element is calculated.

$$F \propto N, \tag{3.14}$$

where F is the force. The MATLAB/Simulink model is shown in Appendix A and the relation between F and N is further investigated and demonstrated in the calibration process below.

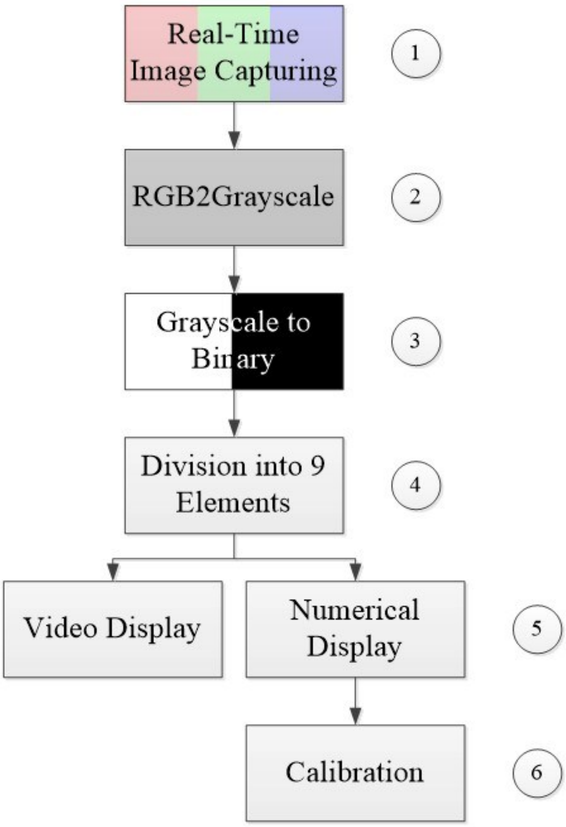

Firgure 3-7 Simulink Flowchart.

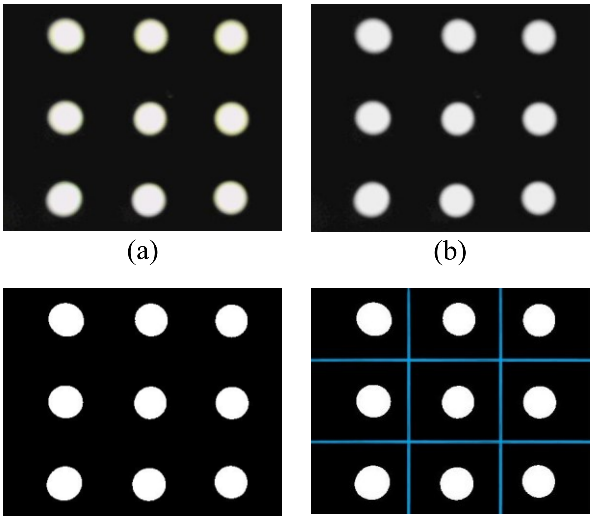

(a) (b)

(c) (d)

Figure 3-8 Sequence of Image Processing: (a) Capturing images, (b) RGB2Greyscale conversion, (c) Binary image, (d) Division into 9 elements.

3.4. TEST SETUP AND RESULTS

A 4 Watt LED torch (Duracell Daylite) with light intensity of 160 lumens is used as the light source. A total of 18 optical fibres with the core diameter of 1mm are used. The core reflective index is 1.49 and the numerical aperture is 0.53. A high speed, low-cost USB camera (Microsoft VX-800) is installed to detect the light intensity changes, which are then transferred to a PC for further analysis. An ATI Mini 40 Force/Torque sensor attached to a National Instruments Data Acquisition Card is used to calibrate and test the static and dynamic response of the proposed sensor. The experimental set up is shown in Figure 3-9.

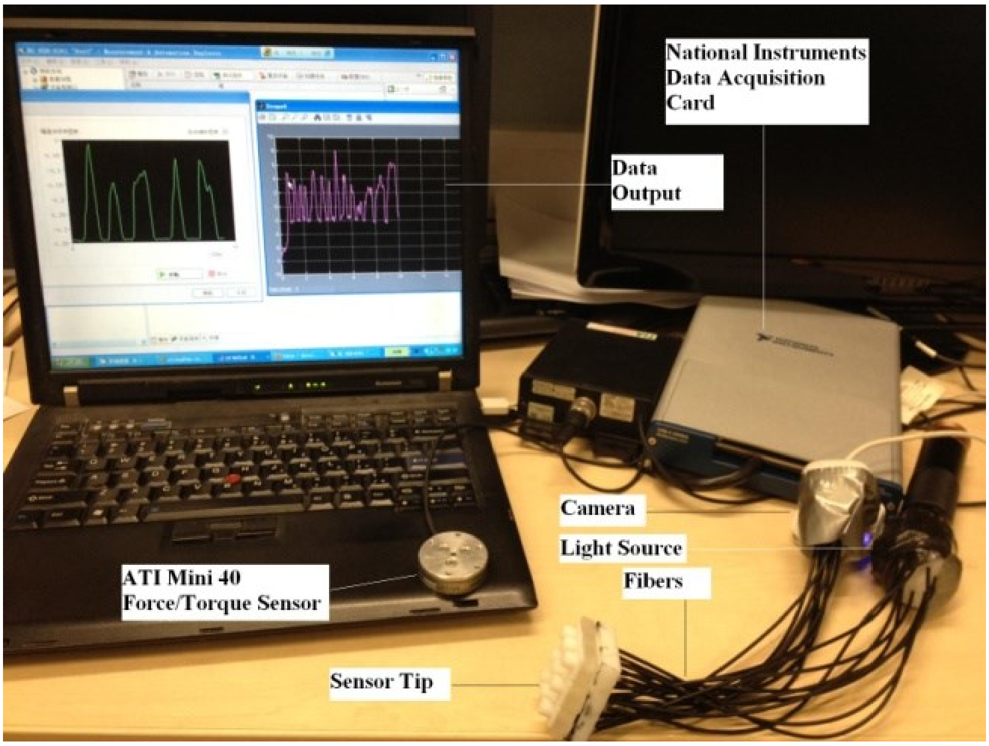

Figure 3-9 Experimental set-up.

3.4.1. VIDEO OUTPUT

Once the sensing system has been switched on, the light information will be transferred from the light source to the unloaded sensing tip and then back to the camera. After the image processing (explained earlier), the binary light intensity images received from the nine sensor elements are displayed, as shown by the camera images of Figure 3-10 (a). Each of the white blobs represents the light intensity projected into the camera by one sensing element. Once a force is applied, the distance between mirror and transmission fibre and receiving fibre is decreased, resulting in an increase of the light intensity. Hence, the number of pixels of the camera image area corresponding to a sensing element will increase as an increased light intensity is received, as can be observed in the central blob of Figure 3-10 (b). A further light intensity display map with different force applied is shown in Appendix B.

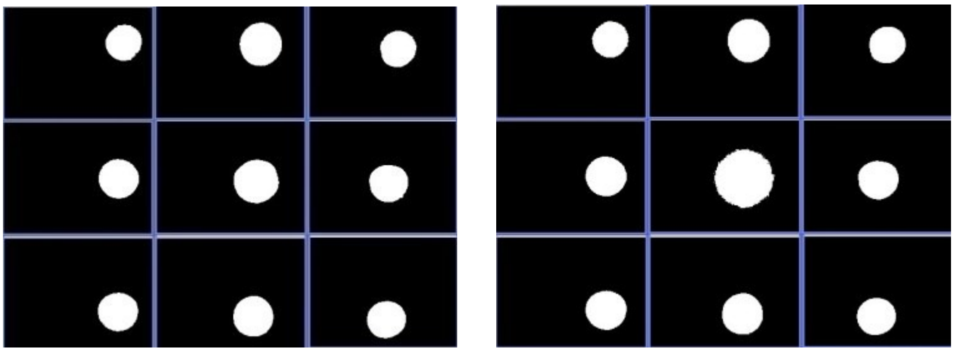
(a) (b)

Figure 3-10 (a) Unload status, (b) Force applied to sensing element that corresponds to the central element of the camera image.

This approach lends itself to a straightforward way of visualizing applied forces. By analysing the number of activated pixels using MATLAB, the relationship between the number of activated pixels and force applied can be used to calibrate the sensor.

3.4.2. CALIBRATION

When forces are applied, the real-time data will be detected and recorded in Simulink. Figure 3-11 below shows the calibration results between applied force and average activated pixel numbers during 10 tests of one single element. Linear and quadratic fitting are also shown in the figure. The same calibration process is applied to all other sensing elements and the coefficients of the quadratic equation ($f = \rho_1 N^2 + \rho_2 N +$

ρ_3, f is force, N is the total numerical value of the pixels in each sensing area) and the linear fitting curve ($f = \sigma_1 N + \sigma_2$) are shown in Table 3-1 and Table 3-2.

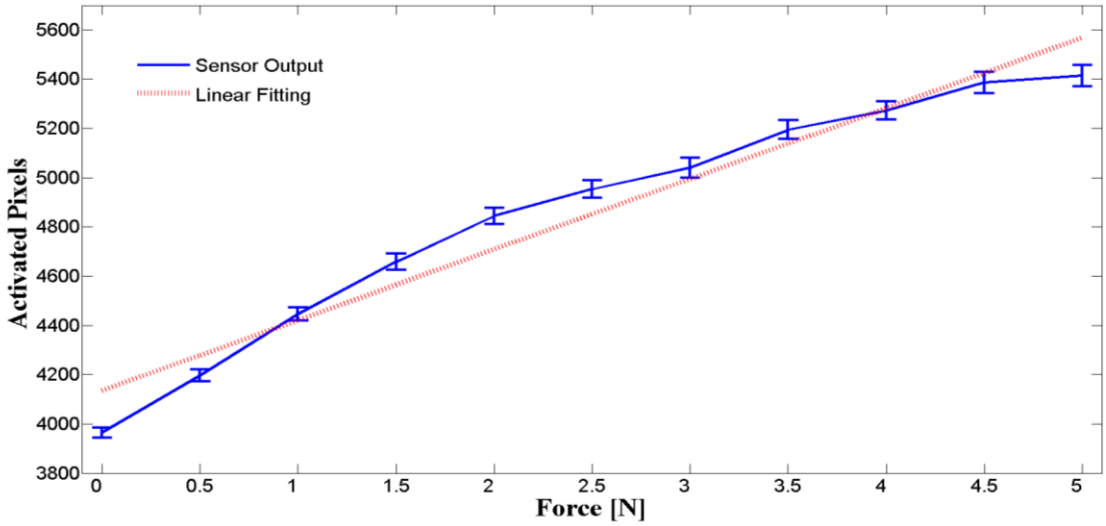

Figure 3-11 Calibration data of the element 5.

Table 3-1 Coefficient of Quadratic Fitting Curve

Sensor Number	**Coefficients**			
	ρ_1	ρ_2	ρ_3	R^2
1	7×10^{-5}	-0.2885	309.3	0.9895
2	2×10^{-5}	-0.1052	111.41	0.9944
3	2×10^{-4}	-0.6379	536.28	0.9796
4	4×10^{-5}	-0.2439	332.66	0.9934
5	2×10^{-6}	-0.0121	22.497	0.9971
6	1×10^{-5}	-0.0814	120.42	0.9943
7	1×10^{-5}	-0.0679	93.697	0.9808
8	5×10^{-5}	-0.3643	625.67	0.9956
9	-1×10^{-4}	0.6784	-1179.2	0.9410

Table 3-2 Coefficient of Linear Fitting Curve

Sensor Number	**Coefficients**		
	σ_1	σ_2	R'^2
1	0.0293	-66.83	0.9707
2	0.0229	-57.911	0.9884
3	0.0313	-52.773	0.9295
4	0.0292	-87.029	0.9856
5	0.0033	-13.683	0.9558
6	0.0081	-23.987	0.9347
7	0.0126	-39.138	0.9698
8	0.0236	-83.946	0.9873
9	0.026	-84.209	0.9323

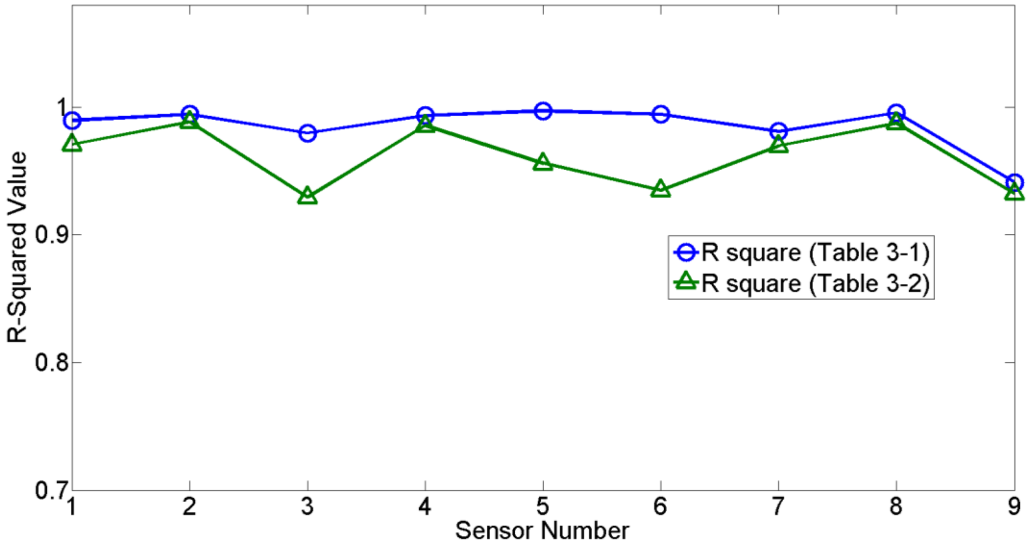

Figure 3-12 Comparison of R-square value between Table 3-1 and Table 3-2.

By comparing the R-squared values between Table 3-1 and 3-2 in Figure 3-12, it can be concluded that the R-squared values of quadratic fitting for each sensing element are higher than those obtained by linear fitting. However, as most of the R-squared values for linear fitting are close to 1 and the offsets from the actual sensor response and the linear response caused by flexible material are within 0.5 N, the system has a reasonable linearity.

3.4.3. STATIC RESPONSE AND HYSTERESIS ANALYSIS

3.4.3.1. Static Response

Using the ATI Mini 40 Force/Torque Sensor to test one element of the developed sensor after the calibration process, we obtain the data shown in Figure 3-13. While some errors exist due to the hysteresis of the silicone material and the noise that is introduced into our experimental system via the transmission and detection procedure, it still can be concluded that the pixel-based sensing principle is a suitable way of detecting tactile information and developing high resolution tactile sensors. For the other 8 sensing elements, shown in Figure 3-14, the same calibration equations with slightly different coefficients are established and further investigated in the following shape detection section. The standard deviation of all sensing elements is shown in Figure 3-15.

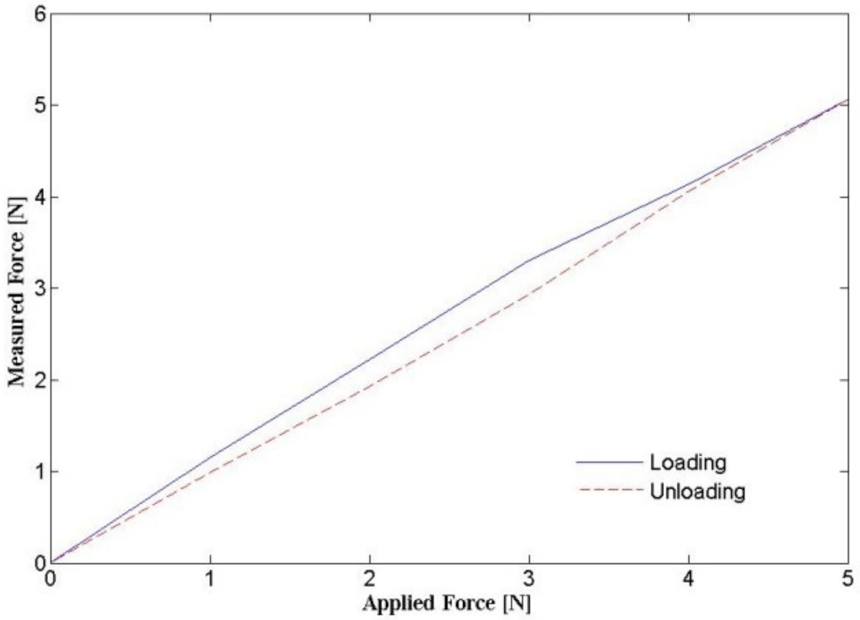

Figure 3-13 Measured static response of a single element during loading and unloading. The hysteresis of the sensor is caused by the silicone.

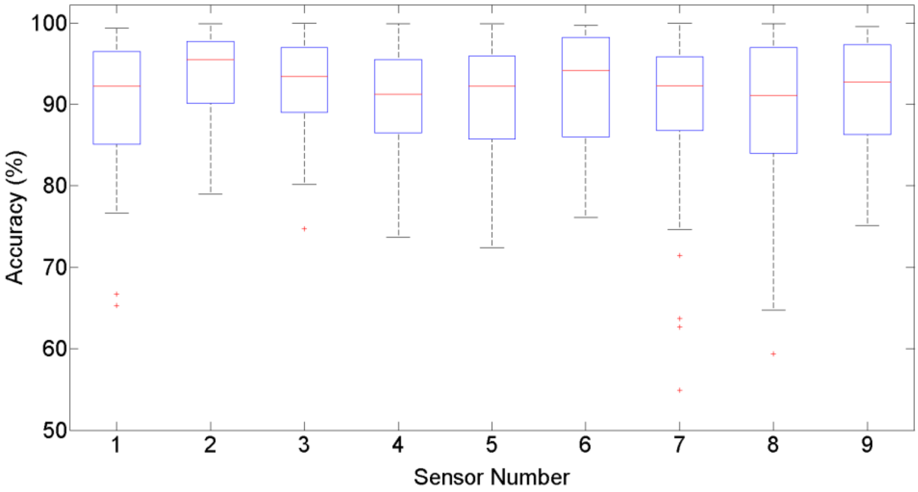

Figure 3-14 Accuracy of all sensing elements, where red line is the median and boxes represent the inter-quartile range.

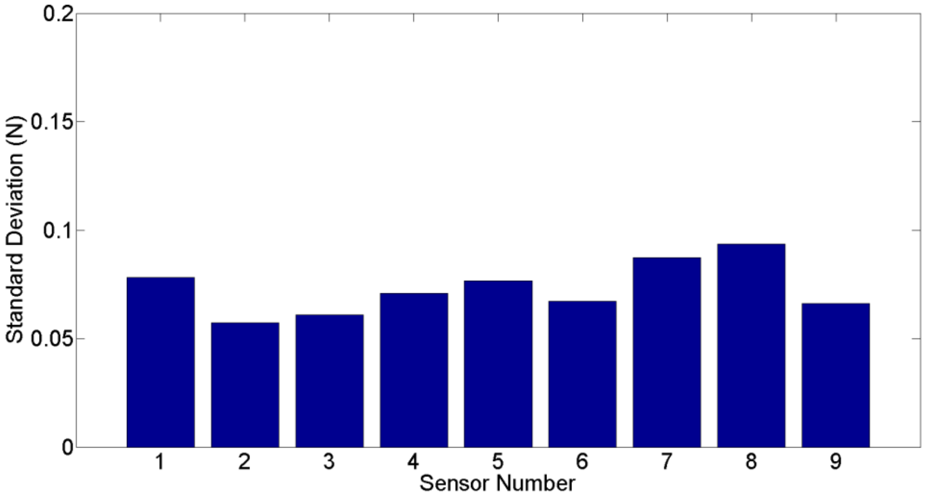

Figure 3-15 Standard deviation of all sensing elements.

3.4.3.2. Hysteresis Analysis

To understand the repeatability and accuracy of the sensor, an analysis on the hysteresis effects on the silicon layer was performed, as shown in Figure 3-16. Only the silicon layer was tested as it is the sensor's sole moving component. Three different areas of the silicon layer were tested: the centre node, bottom centre, and the bottom left corner. The test was performed by indenting the flexible material 2 mm using 10 steps, with a 2 second pause between each step. After a 5 second pause, the motion is reversed and the indenter returned to its original position. An ATI Nano17 force sensor attached to the indenter measured the force resulting from the indentation. Figure 3-16 shows that the amount of hysteresis is 41-42%. It should be noted that the silicone continues to exert a force until the indenter has returned to the zero position, where the indenter is just touching the silicon. Additionally, as seen by the error bars, the standard deviations up to a 0.5 mm indentation are 0.18, 0.20, and 0.25 N for the centre, bottom centre, and bottom left corner, respectively. This indicates that the silicon also has a low amount of hysteresis when the test is repeated. Thus, the results from this analysis suggest that the tactile sensor has a high amount of repeatability as the material is behaving elastically and demonstrates a low amount of change between tests. At greater indentation distances, the standard deviations are larger, which indicates a lower accuracy at high indentations. Overall, the standard deviations are 0.34, 0.45, and 0.55 N for the centre, bottom centre, and bottom left corner, respectively. The results show that even though the stiffness varies depending on the location of the sensor unit, the hysteresis changes only by a small amount (2%). The peak force measured for the centre, bottom centre, and left corner is 6.15, 8.16, and 9.99 N, respectively. Other than the hysteresis effect, sensor signal uncertainty is possibly also caused by other factors, such as crosstalk between sensing elements, light signal loss especially in the connecting parts and mechanical misalignment between fibres. These aspects will be analysed and alleviated as part of future research and development.

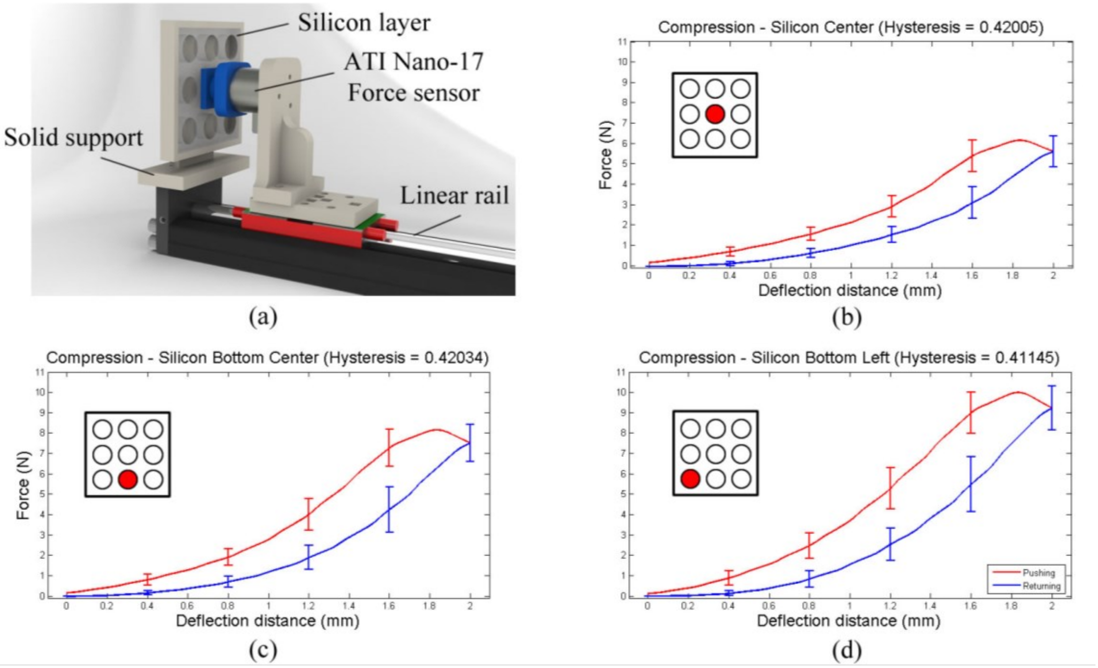

Figure 3-16 Indentation hysteresis testing set-up and results of the silicon layer for the centre, bottom centre, and bottom left corner.

3.4.4. SHAPE DETECTION TEST

To investigate the feasibility of this developed tactile sensor, it was mounted on an industrial robot arm (FANUC M-6iB), which controlled the sensor's position, rotation and movement, as shown in Figure 3-17. After the sensor was recalibrated using the standard force sensor, the robot arm gradually moved down towards the testing platform until it reached the overall output of the tactile sensor around 10 N. Different shapes of the object were attached to the platform and tested by the same procedure and the individual output of each sensing element was recorded and shown in Figure 3-18.

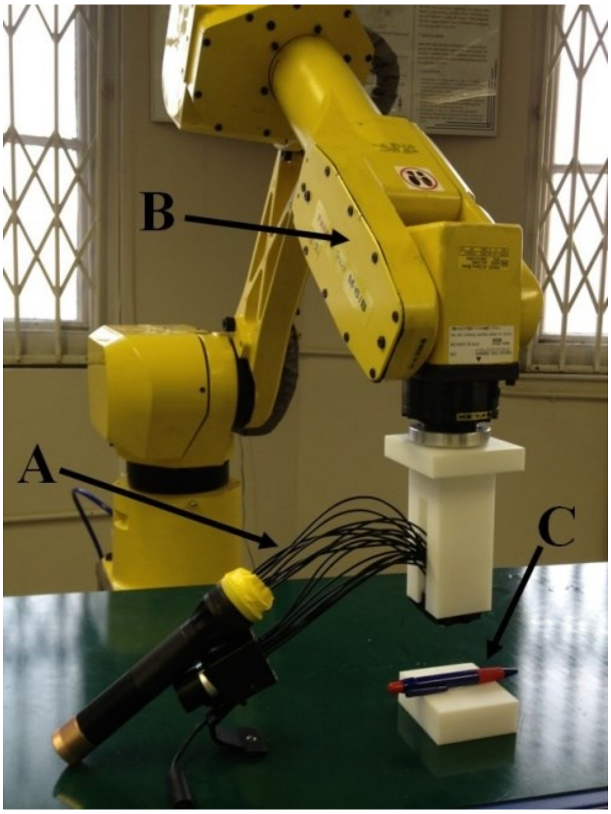

Figure 3-17 Integration of optical fibre tactile sensor with robot arm (A: tactile force sensor, B: Robot manipulator, C: Testing platform).

During the test, the sensor started contacting the object at t=3s and left the object at t=12s, then the average output of each sensing element was calculated and displayed in a tactile image, as shown in Figure 3-19. For the first test, Figure 3-18 (a), forces applied on elements 3, 6 and 9 were successfully detected with a force of about 2.7 N. It can be noted that the noise increases as the applied force increases on each sensing element. Also there exists small crosstalk values (less than 10%), in which the closer to the forces applied area, the bigger the value are (0.2 N–0.5 N). However, both are kept in an acceptable range thus not affecting the usefulness of the sensor in detecting contact area and force, which can also be seen from the following two tests, Figure 3-18 (b), (c). On the contrary, the crosstalk values between the fibres can be used to further expand the resolution of the sensor [92], which is where future work is leading, together with sensor miniaturization.

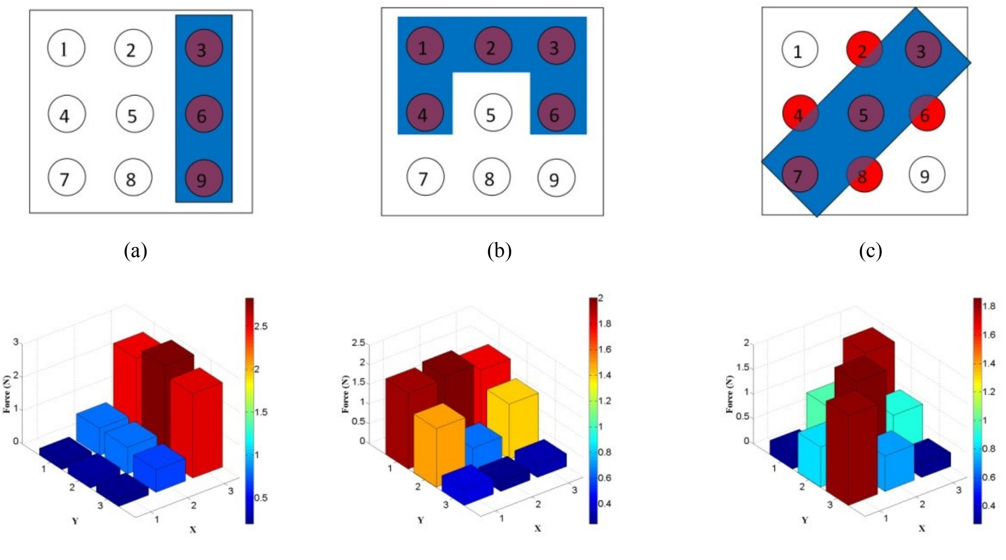

(a) (b) (c)

(d) (e) (f)

Figure 3-18 Response of each individual sensing element during testing with different shapes and displacements (a), (d) a rectangular-shaped object placed on the right side of the sensor, (b), (e) a 'U'-shaped object placed on the top of the sensor, (c), (f) a rectangular-shaped object diagonally placed in the middle of the sensor.

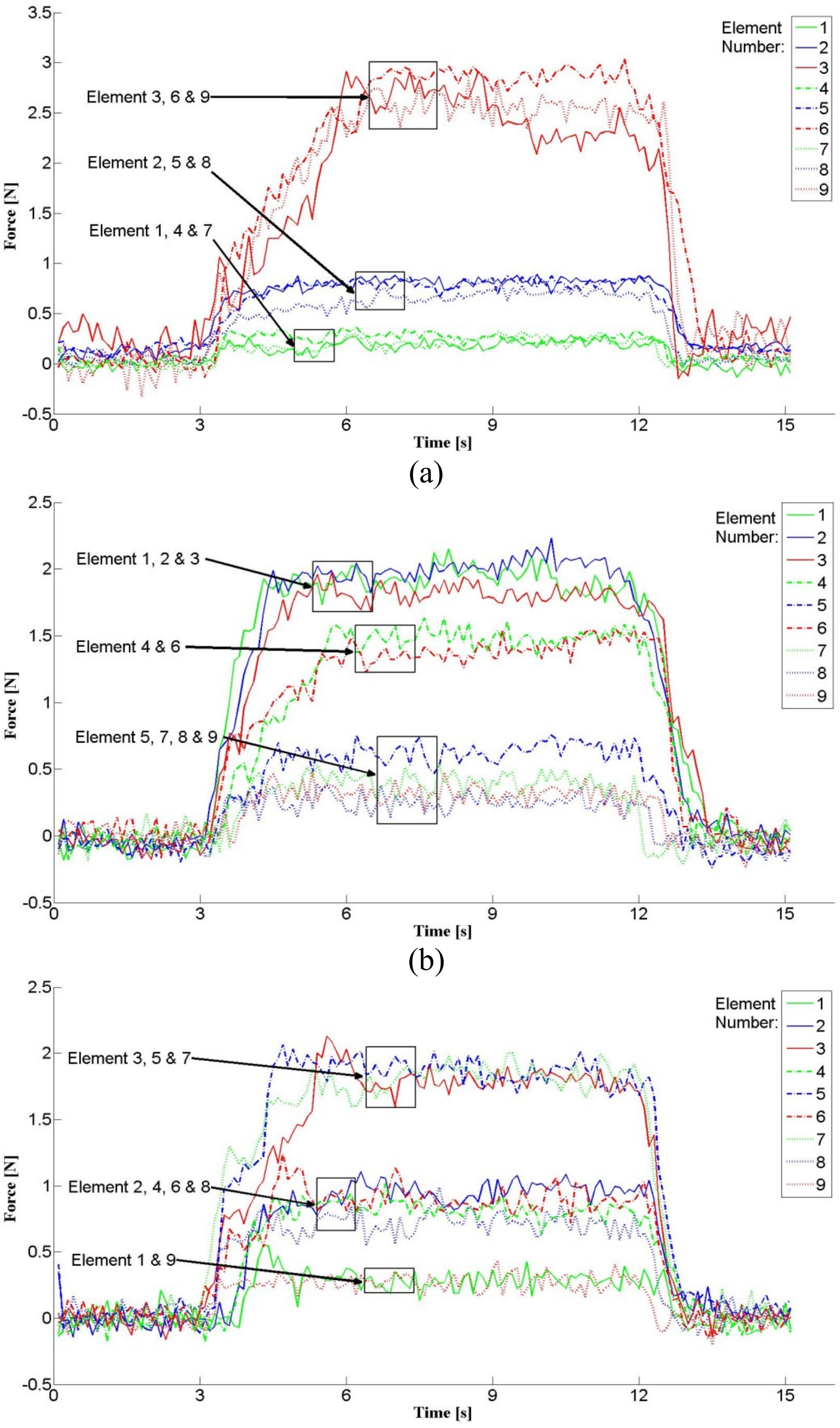

(a)

(b)

(c)

Figure 3-19 Response of each individual sensing element during testing.

3.5. CONCLUSIONS

This chapter presented the design of the laboratory prototype of a tactile array sensor using fibre optics and a 2D vision sensor. In contrast to conventional sensing approaches, such as resistive or capacitive-based sensing methods, which strongly rely on the generation and transmission of electronics signals, here electromagnetically inert optical fibres were utilized to develop the tactile array sensor. The individual sensing elements of the proposed sensor detect normal forces, fusing the information from the individual elements allows the perception of the shape of probed objects. Applied forces deform a micro-flexure inside each sensor tactel, displacing a miniature mirror which, in turn, modulates the light intensity introduced by a transmitting fibre connected to a light source at its proximal end. For each tactel, the light intensity is read by a receiving fibre connected directly to a 2D vision sensor. Computer software, here MATLAB, is used to process the images received by the vision sensor. The calibration process was conducted by relating the applied forces to the number of activated pixels for each image received from a receiving fibre. The proposed approach allows the concurrent acquisition of data from multiple tactile sensor elements using a vision sensor such as a standard video camera. Test results of force responses and shape detection have proven the viability of this sensing concept.

In the following chapter, the issues of size, spatial resolution, hysteresis and crosstalk will be addressed further exploring the proposed sensing concept. Also, the tactile sensor in Chapter 4 is improved further to conduct palpation procedure in MIS and provide tactile feedback information.

Chapter 4 Miniaturized Tactile Probe Head for Palpation in MIS

This chapter presents a miniaturized tactile probe head with 14 sensing elements to provide tactile information for palpation in minimally invasive surgery. It first introduces existing sensing technologies for robot assist palpation and their limitations, and then proposes the method based on Chapter 3 to address these issues. By using optical fibres and ABS material to create sensor structure, our tactile probe head is designed to be MRI compatible. After sensor calibration, tests of dynamic responses and shape detection have been carried out. For validation of the usefulness of proposed probe head, hard nodules have been embedded in both silicone phantom and lamb kidney as tumours, and such soft-tissue imitating phantoms have been used in palpation experiments involving the proposed tactile array sensor. The results from ex-vivo experiments have shown the tactile probe's effectiveness in tumour detection.

4.1. INTRODUCTION

During open surgery, palpation – a process where the clinicians press their fingers on the patient's soft tissue organs to assess tool-tissue interaction forces – is a powerful tool in locating subsurface anatomical structures and assessing tissue properties [93]. The detection of tumours in breast [94] and prostate [95] are good examples. As certain solid tumours are harder than the surrounding tissue, their presence, sizes, and locations can be obtained through tactile feedback. Effective palpation will increase the chance of performing the surgery successfully whilst reducing the error margins. However, direct manual palpation is prohibited by the small incisions used in MIS [26]. Compared to the traditional open surgery, MIS offers many advantages [96] including lower risks, reduced tissue trauma, and accelerated postoperative recovery due to its small incisions. Nevertheless, all these advantages come at the price of the absence of direct tissue interaction and the loss of tactile feedback [97] [28].

In order to provide an alternative to palpation to the surgeons during MIS, a popular approach is to develop surgical instruments with force sensing capability to indent, or grasp of a soft tissue [98]. Based on mechanical soft tissue modelling and measurements of force and tissue local deformation, tissue properties (e.g., size, shape, stiffness and depth) can be identified [99], providing the surgeon with a better understanding of internal organs during the operation [100]. Numerous force and tactile sensing technologies for instrumenting the surgical devices of MIS have been developed [14] [101]. Tholey *et al.* [102] investigated current-based sensing methods in the framework of a specially designed laparoscopic grasper, which proposed a simple way to measure force in MIS. Tadano *et al.* developed a 4 degree-of-freedom pneumatic-driven forceps providing force sensing capabilities based on the measurement of air pressure. In [103], a force-sensitive probe has been created to localize lung tumours by analysing tissue stiffness. In [104], a robotic palpation system equipped with the force/torque sensor has been developed for examining the prostate gland. Furthermore, a rolling palpation probe, which measures the stiffness of soft tissue by rolling over it, was proposed for tissue abnormality localization [105] [26].

The aforementioned instruments are able to measure the local mechanical tissue properties. However, it is time consuming to investigate the tissue properties of a large area using these devices [106]. To provide a surgeon with the ability to rapidly investigate a large tissue area, various palpation tools have been developed using tactile array sensors to mechanically image the interested tissue area. Based on resistive sensing, Schostek *et al.* [107] developed a prototype of a MIS grasper which provides both the spatial distribution and magnitudes of the applied forces. Among certain sensing principles, capacitive-based sensing is comparably efficient for measuring the applied forces and it has been widely applied for palpation. A capacitive tactile array remote palpation system was developed by Howe *et al.* [108]; this palpation system can measure forces with a high resolution over a range of 0 to 2 N. Rajamani's group [109] has developed a microelectromechanical systems (MEMS) tactile sensor by using two capacitive force gauges, which are integrated under a pair of bumps with different stiffness. This sensor can quickly detect elasticity change and is capable of measuring tissue elasticity *in-vivo*. Commercial capacitive-based tactile array sensors have also been implemented for surgical palpation to localize prostate tumours [110] and to locate lung tumours [111] [13]. The main drawbacks [112] of the resistive-based and the capacitive-based tactile array sensor are associated with the sensor sterilization. Based on [113], the electronic components of these sensors could be damaged through the sterilization procedure. In addition, these types of sensors are generally not MRI compatible, since their metallic components can introduce severe MR image distortion, and thus limiting the sensors' applications in MRI environments. Since electrical power is not required by the sensing elements, the operations of the piezoelectric-based sensors are considered more reliable and have a wide range of applications. As an application in MIS, Dargahi *et al*. [73] developed a micro-machined tactile sensor that can be integrated with a jaw of endoscopic graspers. The drawbacks of piezoelectric materials are that they can only detect time-varying forces and are sensitive to changes in temperature [114].

The fibre optic based tactile sensing method is an effective way to equip medical tools with the force measurement capability within a high intensity electromagnetic field. An optical fibre sensor uses four main sensing mechanisms, which are wavelength, phase, polarization and intensity modulation [115]. All of these mechanisms consist of a light source, transduction and detection parts. Here the light intensity modulation method [116] [117] is used as it is versatile, inexpensive, temperature insensitive and easy to fabricate. Most of the existing intensity modulation fibre optic force sensors [118] [119] use individual phototransistors or photodiodes to convert light intensity into voltage signals, which are converted into force information through calibrations.

A different method of light intensity modulation is proposed [120]. Instead of using one optoelectronic receiver for each sensing element, only one low cost CMOS (complementary metal–oxide–semiconductor) USB camera is employed to capture and detect the light intensity changes of all sensing elements. The signals are then processed in MATLAB/Simulink and converted to a tactile map. Previous research work [121] [122] [66] on camera-based tactile sensors focused on analysing image pattern from the small-sized camera integrated at the tip of tactile sensors. In the proposed method the detection camera can be placed away from the tip by using optical fibres to transmit the light signals. It allows the tactile sensor to be further miniaturized regardless of the integrated camera size, and renders it able to work in MR environments by placing the detection camera outside the MR range.

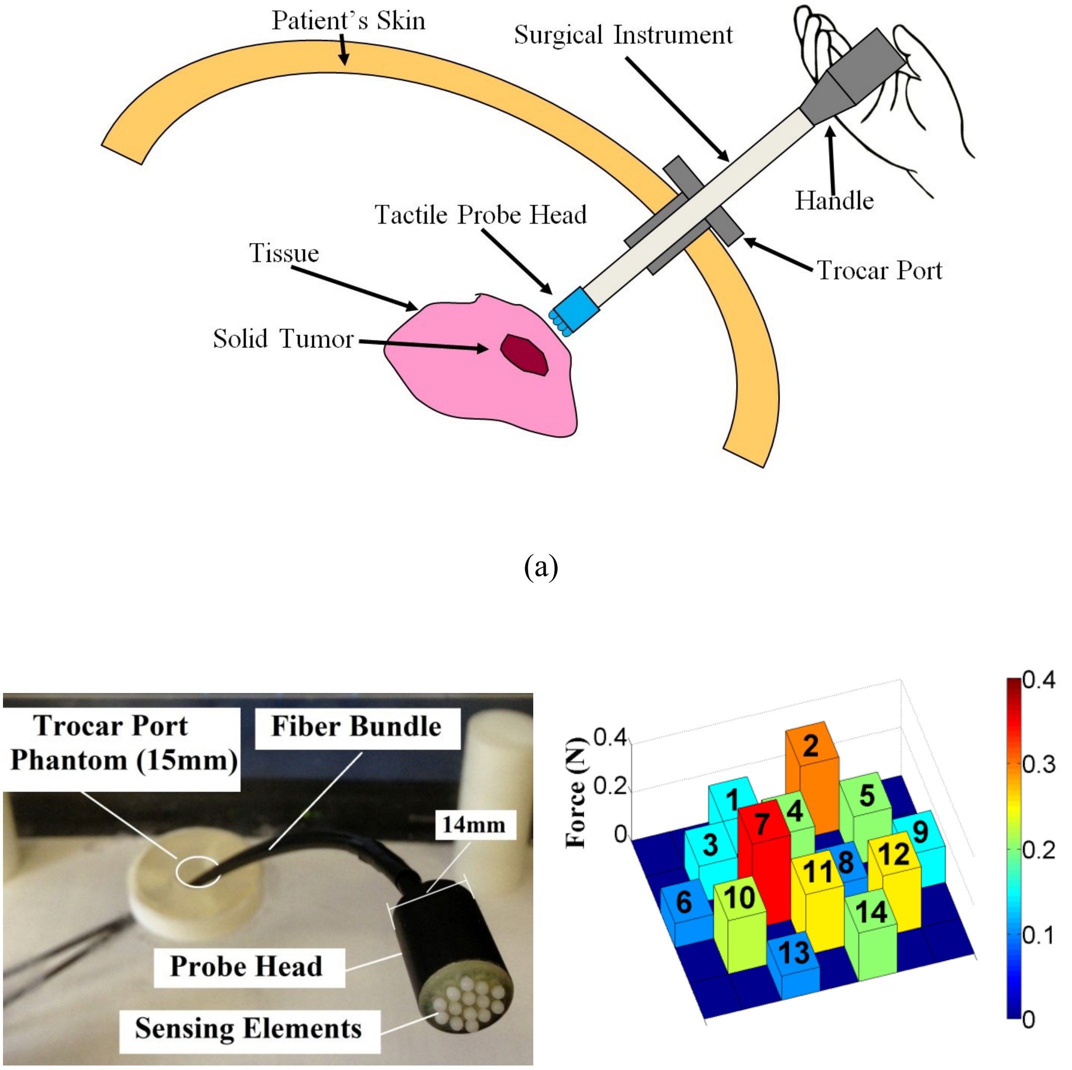

(a)

(b) (c)

Figure 4-1 (a) Application area of proposed tactile probe head, (b) Real size of the developed MRI-compatible tactile probe head, (c) Force feedback from the tactile probe head.

In this chapter, an optical tactile array probe head for tissue palpation during minimally invasive surgery is presented, shown in Figure 4-1. The sensing system developed in this paper is low cost, small in size, lightweight, free from electromagnetic interference, water and corrosion resistant and capable to operate in harsh environments. Advancing from previous work [120], the proposed sensing system is further miniaturized, has increased sensor sensitivity and achieves effective crosstalk elimination. This optical fibre based sensing system is suitable for medical applications because it can be sterilized and is MRI compatible. The developed probe head can be integrated with various types of medical tools during operations. Because of its low manufacturing cost, it can even be disposed after single surgery. The probe head has a diameter of 14 mm thus it can be used through a 15 mm trocar port during MIS [123]. Due to the design simplicity, the proposed tactile probe-head can be readily miniaturized further to fit in smaller trocar ports or even provide tactile force feedback from a catheter-tip (4-8 mm). This probe head advances from previous research work on fibre optic based palpation probe, which is presented in [124]. The relationship between the optimal light response and the displacement change has been investigated, together with the dynamic response of the tactile sensor. Experiments were carried out on silicone phantom and lamb kidney with simulated tumours in order to produce stiffness map. The results demonstrate that the probe head is able to produce a high resolution stiffness map which can clearly indicate tumour locations.

4.2. METHODOLOGY

The schematic design of the presented sensor to explain the sensing methodology is shown in Figure 4-2. The light source transmits the light to the sensing area, which is 14 mm in diameter with 14 sensing elements. When force is applied to a sensing element, the displacement change of the flexible material varies the light intensity observed by the receiving fibre. The image of the light intensity distribution is captured by the camera attached at the end of the receiving fibre, and converted to spatial contact forces through image processing.

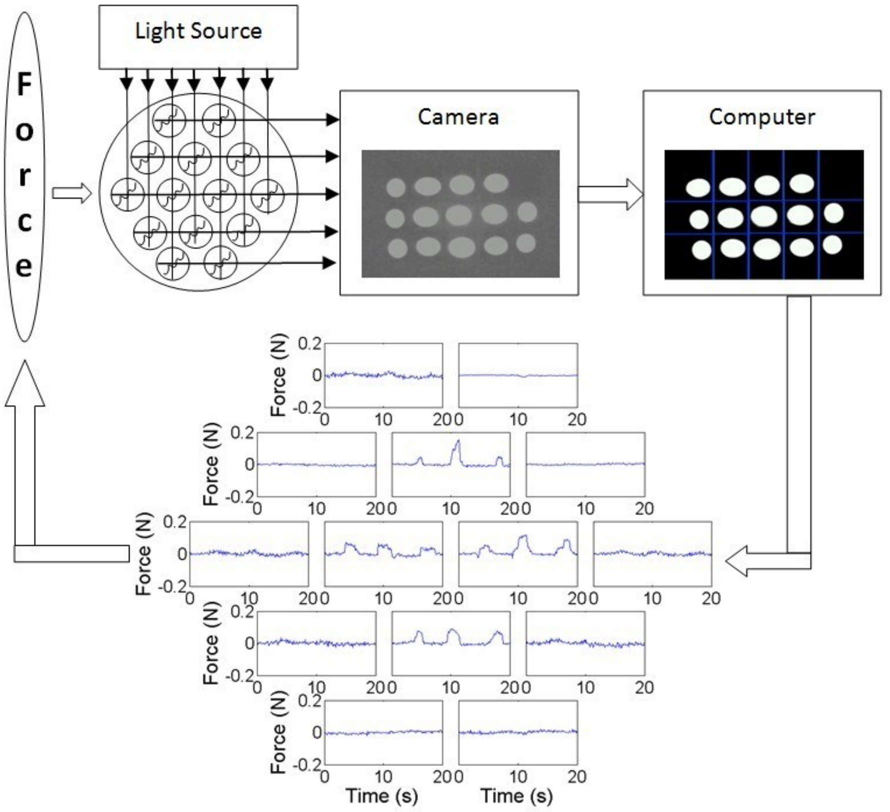

Figure 4-2 Schematic design of proposed tactile sensor using camera.

4.2.1. PROCESSING OF LIGHT INTENSITY IMAGE

In order to extract useful information together with removing background noise of the light intensity image, the greyscale image was converted into binary image (Figure 4-3). A variety of thresholding methods have been proposed in the past, such as point-dependent and region-dependent method [125], where the threshold value is determined either by the grey level of each individual pixel or the local grey level neighbouring each pixel. A global thresholding method [126] is giving one threshold value to the entire picture, while a local one [127] provides different values to sub-images. Due to high contrast of background and object in the light intensity image, a thresholding method is used by defining the valley of the histogram as the threshold value [128]. Compared to previous described thresholding methods, this is more straightforward with less computational complexity. We define $g(x, y)$ as the grey value of the pixel coordinate at (x, y) in the image with a size of x_{max} by y_{max}.

$$g(x, y) \in \{0,1,2 \dots ,255\}, \tag{4.1}$$

where $1 \leq \mathrm{x} \leq \mathrm{x}_{\mathrm{max}}$, $1 \leq \mathrm{y} \leq \mathrm{y}_{\mathrm{max}}$, 0 stands for the darkest pixel and 255 for the brightest pixel. Each pixel value is converted from greyscale (0-255) to either 0 or 1 utilizing the following equation:

$$g_T(x, y) = \begin{cases} 0, if\ g(x, y) < I_{threshold} \\ 1, if\ g(x, y) > I_{threshold} \end{cases}, \tag{4.2}$$

where $I_{threshold}$ is the threshold value to eliminate ineffective pixels from the background, $g_T(x, y)$ is the value of pixel at (x, y) after thresholding. The real-time image is divided into 14 sections, each representing one single sensing element. The segmentation is processed via MATLAB using coordinates of pixels, which are predefined. The activated pixel number N of each section is given by:

$$N = \sum g_T(x, y), \tag{4.3}$$

where N is the total value of the pixels in each sensing area, the size of the section is x_{max} by y_{max}. The relation between force f and pixel value N is further investigated and demonstrated in sections below.

4.2.2. PROBE HEAD DESIGN

The proposed probe head design consists of two plastic optical fibre bundles (SH1016, Mitsubishi Rayon Co., Ltd., Tokyo, Japan). Each bundle has 16 individual optical fibres inside with a core diameter of 0.231mm to 0.279mm. The core refractive index of each fibre is 1.49 and the numerical aperture is 0.50. One fibre bundle is used for transmitting light from the light source and the other one for receiving light to the camera. The individual fibres are fixed on the supporting base (Figure 4-4). The developed sensor prototype, shown in Figure 4-5, was designed in Solidworks (Solidworks Corp., MA, US) and printed by a rapid prototype machine (ProJet HD 3000, 3D-Systems, SC, US). The sensor is fabricated using ABS (acrylonitrile butadiene styrene) material which is lightweight, free from the chemical corrosion and MRI compatible.

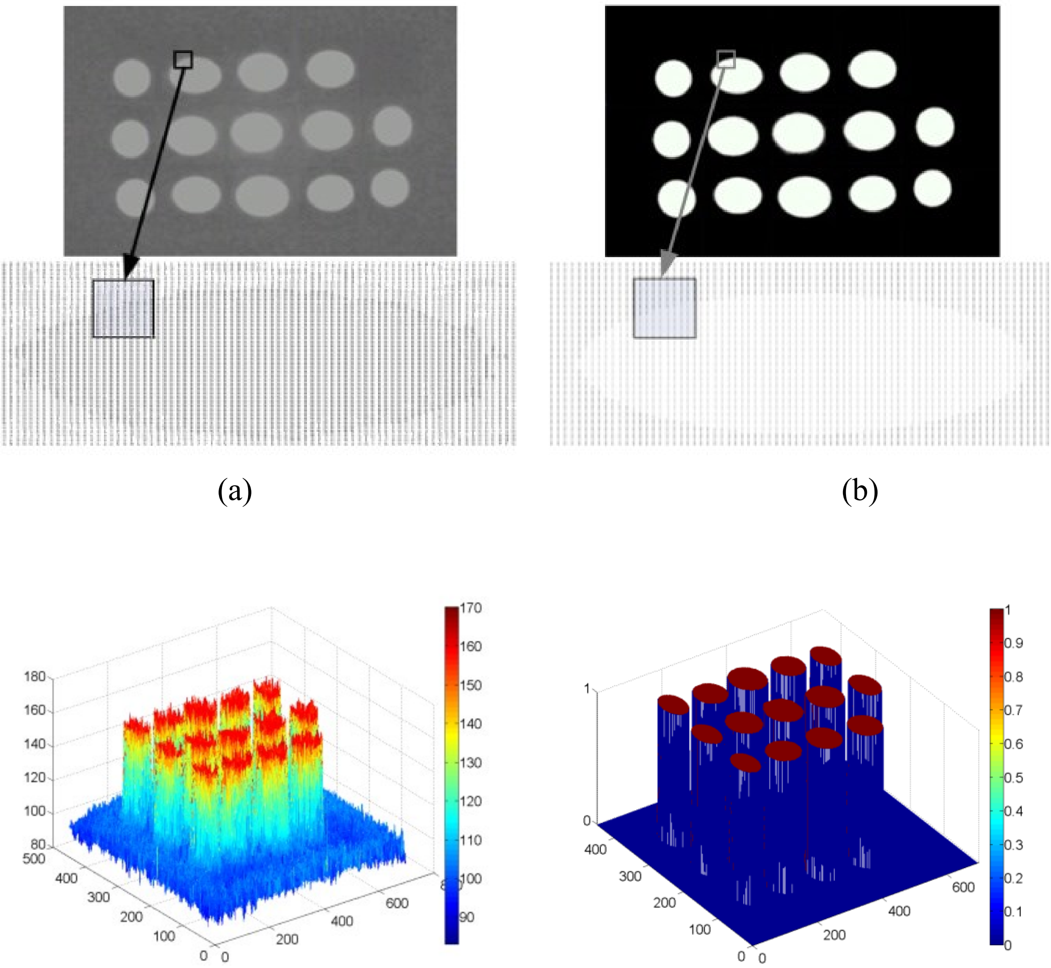
(a) (b)

(c) (d)

Figure 4-3 Sequence of Image Processing before and after thresholding: (a) greyscale images captured by camera, (b) binary image after thresholding, (c) intensity map of greyscale picture, (d) intensity map after thresholding.

Latex rubber is used as the flexible structure between the supporting material and sensing tip. The supporting structure is designed with 14 separate grids to isolate the deforming area of each individual sensing element from the adjacent elements, preventing crosstalk. There are 14 cylindrical sensing units each with ball shape tip. Below each unit, a concave aluminium surface (mirror) is attached to reflect light from the transmitting fibre to the receiving fibre, enabling more effective light transmission between fibres. As the sensor detects z-axis force information only, a top layer is designed to constrain the x and y-axis movements of the sensing units.

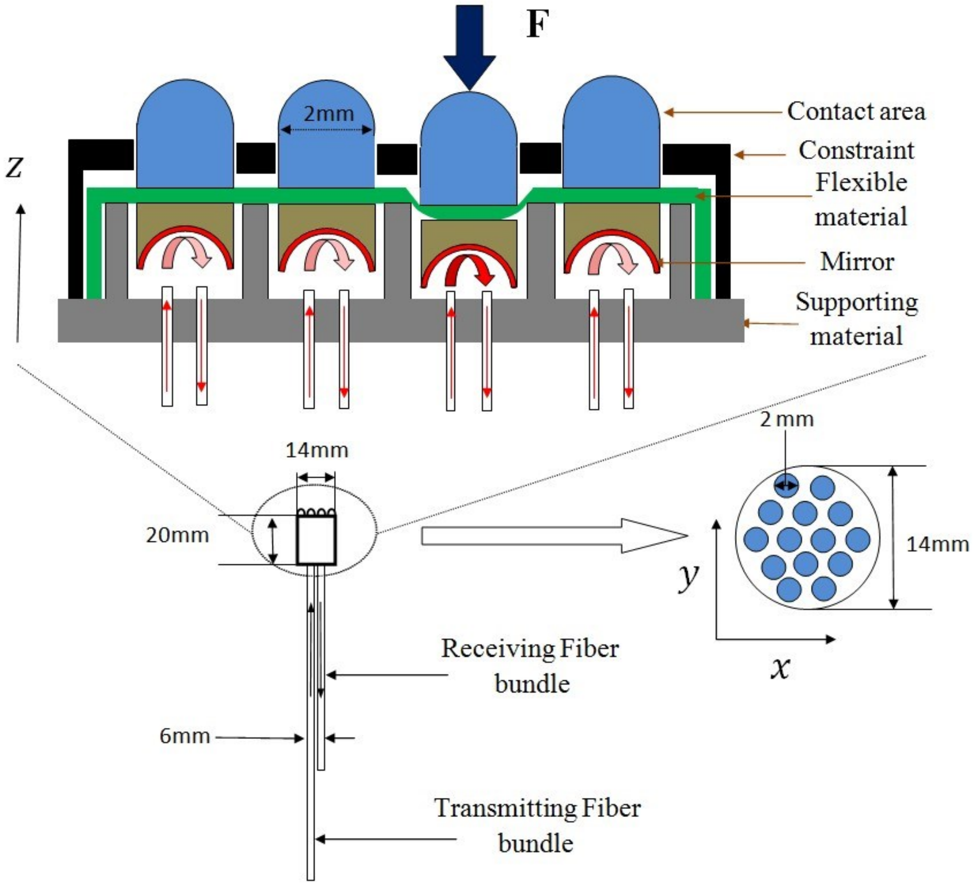

Figure 4-4 Detailed sensor design and assemblies.

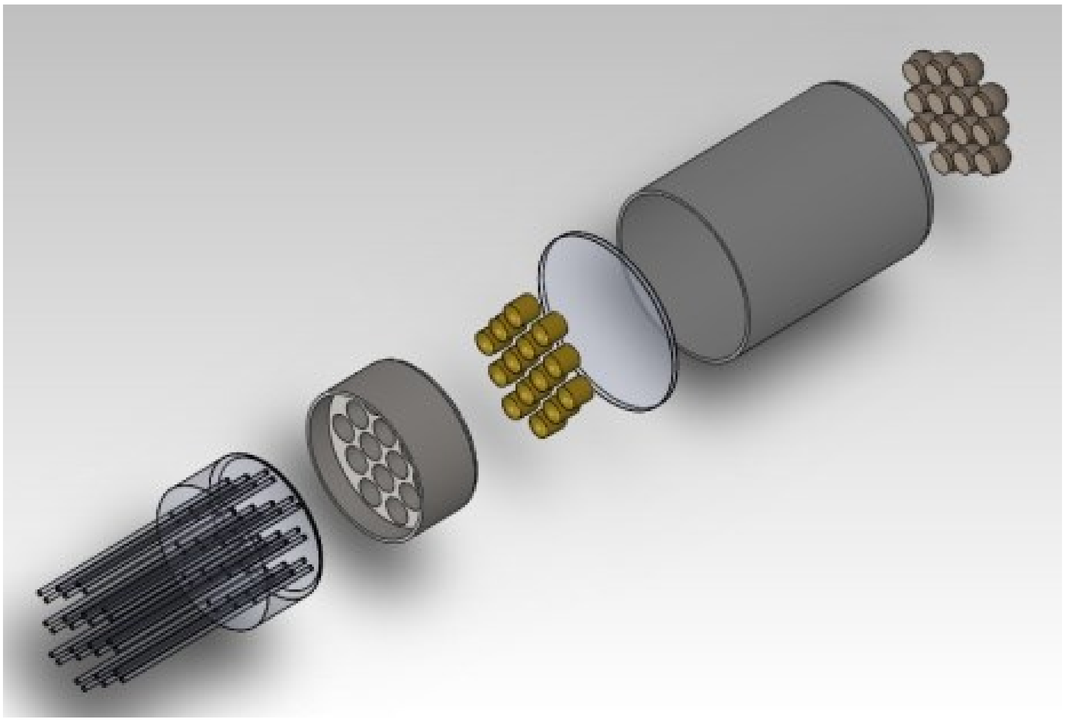

(a)

(b)

Figure 4-5 (a) SolidWorks drawing of proposed sensor, (b) photograph of proposed sensor.

Four different patterns of the reflective surface have been investigated as shown in Figure 4-6. One reflective surface is flat while the other three have an ellipsoidal concave shape with same minor radius of 1 mm but different major radius *r* (0.5 mm, 1 mm and 2 mm). A pair of transmitting and receiving fibres (core diameter 0.25mm, refractive index 1.49 and numerical aperture 0.50) is placed in parallel with a distance of 1mm between them. A fibre optic illuminator (Fibre-Lite 3100, Dolan-Jenner Industries, MA, US) is used to provide a stable light source at a wavelength of 560 nm; a low-cost CMOS HD camera (Microsoft LifeCam Studio, Microsoft, WA, US) is used as the receiver and controlled by MATLAB (Mathworks Inc., MA, US). All parameters of the camera (e.g. autofocus, zoom, white balance and aperture) were kept constant during the test. The aluminium tape (Maplin Electronics Ltd, UK) is used as reflective surface attached to ABS support.

To evaluate different reflective surface, the light intensity images are recorded while the distance between the reflector and fibre changes in increments of 0.1mm from 0 to 2.5mm. For each reflective surface, tests are repeated 10 times. The results are shown in Figure 4-7. It was found that the flat reflector introduced a high level of error and no light signal can be detected after 1.5 mm which may be caused by the scattering of the light. In contrast, with a concave reflector the error is relatively low and the light signal starts to decrease significantly at 1.5 mm until 2-2.5 mm. The proposed sensor achieves a relatively linear response within a displacement range of at least 0.5 mm, allowing the flexible structure to deform to detect forces. From the test results, the concave reflector with medium radius (*r*=1 mm) is chosen, utilizing its response range of 2-2.5 mm. The variance of the results in Figure 4-7 is caused by fibre misalignment and the light noise from environment.

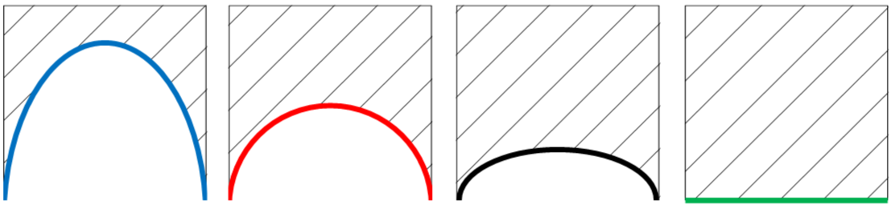

(a) (b) (c) (d)

Figure 4-6 Different patterns of reflection shape for testing the relationship between displacement and light intensity change: (a) reflector with small major radius ($r = 0.5\ mm$), (b) reflector with medium radius ($r = 1\ mm$), (c) reflector with big radius ($r = 2\ mm$), (d) flat reflective surface ($r = \infty$). r is the major radius of the ellipse.

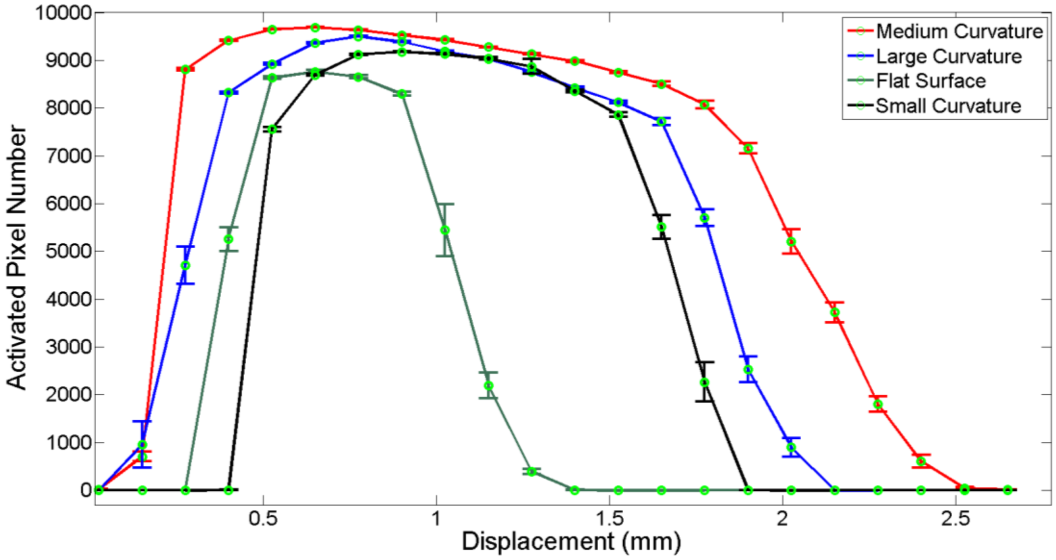

Figure 4-7 Relationship between light intensity (activated pixel numbers) and displacement change.

4.3. EXPERIMENTAL RESULTS

The experimental set-up for tactile probe head testing is shown in Figure 4-8. The same light source (Fibre-Lite 3100 Dolan-Jenner Industries, MA, US) is used during the test. A USB camera with high-definition is used to transfer the image of light intensity to the computer for further analysis. An ATI Nano 17 Force/Torque sensor together with a data acquisition card (NI USB-6341, National Instruments, TX, US) is used for calibrating the proposed tactile probe head.

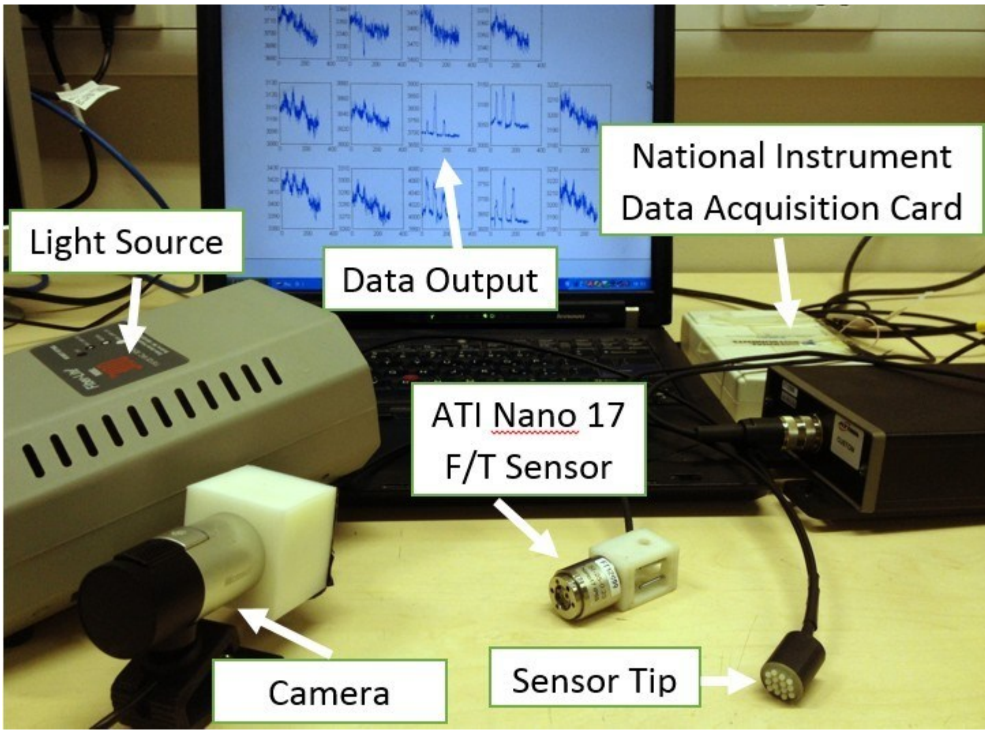

Figure 4-8 Equipment Set-up.

In order to find the appropriate light intensity from light source and camera brightness compensation level, the noise level of three different brightness compensation levels and three different intensities of light from the light source were investigated on the proposed sensor. The results of all 9 tests are shown in Appendix D. As can be seen from Table 4-1, low light intensity with medium brightness compensation demonstrates the minimum noise level. However, during tests, low light intensity is accompanied with low sensitivity. In this case, we choose medium scale light intensity from light source and medium brightness compensation from the camera to achieve both low noise and high sensitivity.

Table 4-1 Noise Level

Light Intensity	Brightness Compensation		
	High	Medium	Low
High	25.5358%	6.293%	3.454%
Medium	8.4086%	1.053%	3.737%
Low	0.7154%	0.478%	17.539%

4.3.1. CALIBRATION

Before using the tactile probe for palpation, calibration is essential. To conduct calibration, the tactile sensor was mounted on a rigid static support, as shown in Figure 4-9, and the 14 sensing elements were loaded individually using the ATI Nano 17 Force/Torque sensor. Each sensing element has been tested 10 times at increments of 0.05 N from 0 N to 0.4 N. The real-time image data is recorded by the camera and converted to distributed force information through the image processing procedure elaborated in Section II.A. Figure 4-10 shows the relations between activated pixels and applied forces of sensing element 14 for both linear and quadratic fitting, while the other 13 sensing elements are shown in Appendix C. The quadratic and linear relationship between the sensor output, which is the pixel number and applied force, is represented by

$$N = \gamma_1 f^2 + \gamma_2 f + \gamma_3, \tag{4.4}$$

$$N = \delta_1 f + \delta_2, \tag{4.5}$$

where N is the output of the sensor, f is the force on individual sensing element and $\gamma_1, \gamma_2, \gamma_3, \delta_1, \delta_2$ are the calibration coefficients, which are listed in Table 4-1 and Table 4-2 together with respective R-squared values.

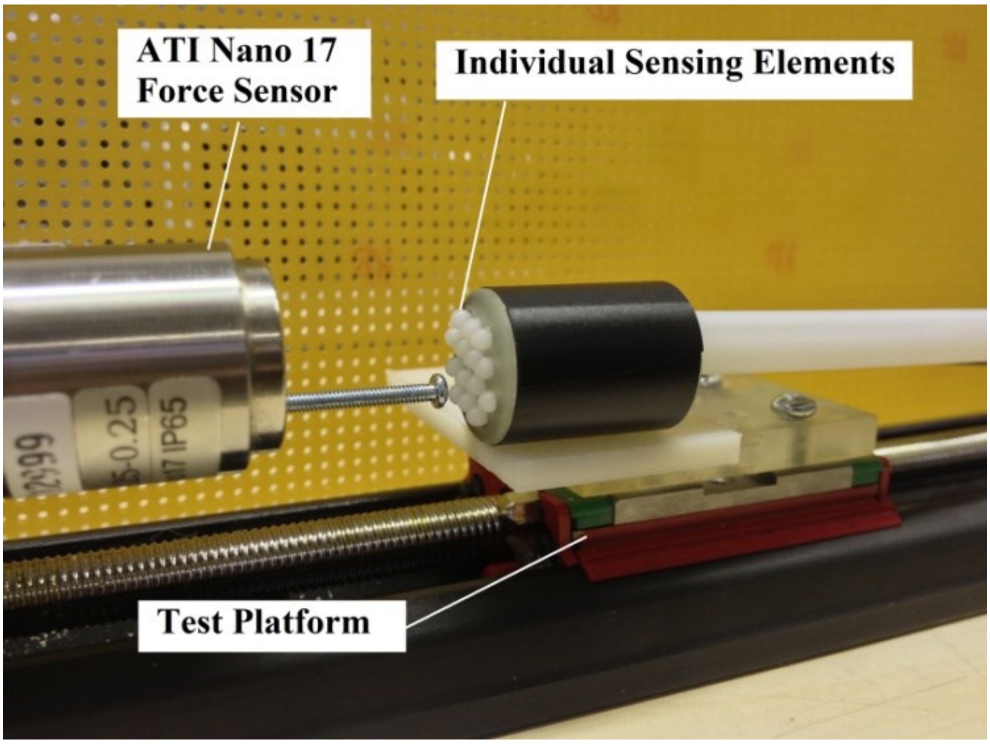

Figure 4-9 Sensor calibration set-up.

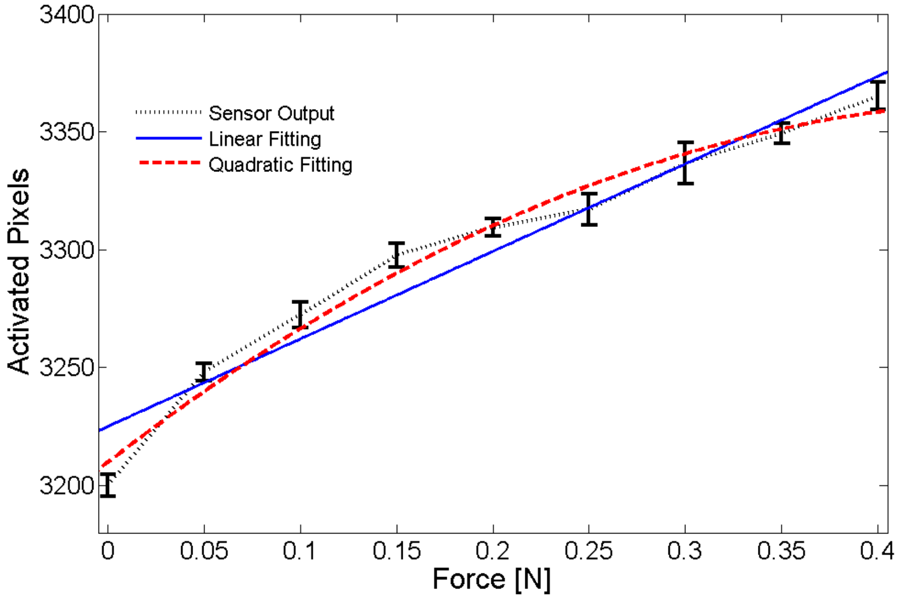

Figure 4-10 Measured output responses of sensing element 14.

Table 4-2 Coefficient of Linear Fitting Curve

Sensor Number	**Coefficients**		
	δ_1	δ_2	R_o^2
1	18.559	3206.7	0.9435
2	14.995	3548.8	0.8814
3	8.4941	3022.7	0.688
4	19.297	3721.5	0.9735
5	9.1086	3246.1	0.963
6	8.2409	3349.8	0.7241
7	37.468	3423.1	0.9797
8	24.012	3662.2	0.8967
9	55.899	3443.9	0.924
10	34.74	3065.4	0.7354
11	47.833	3202.1	0.9246
12	46.17	3544.8	0.8083
13	48.63	3114.2	0.9386
14	13.612	3088.4	0.9301

Table 4-3 Coefficient of Quadratic Fitting Curve

Sensor Number	**Coefficients**			
	γ_1	γ_2	γ_3	R^2
1	-1.6259	34.817	3176.9	0.9807
2	-1.3906	28.901	3523.3	0.9203
3	-1.997	28.464	2986.1	0.8832
4	0.1055	18.242	3723.4	0.9737
5	-0.399	13.099	3238.8	0.9724
6	-1.8894	27.135	3315.2	0.9195
7	-1.0061	47.529	3404.6	0.9833
8	-2.84	52.412	3610.1	0.961
9	-2.3967	79.866	3400	0.9328
10	7.6529	41.789	3205.7	0.9186
11	-2.7513	75.346	3151.6	0.9403
12	-8.2542	128.71	3393.5	0.9409
13	-0.5315	53.945	3104.4	0.9392
14	0.9179	4.4338	3105.3	0.9518

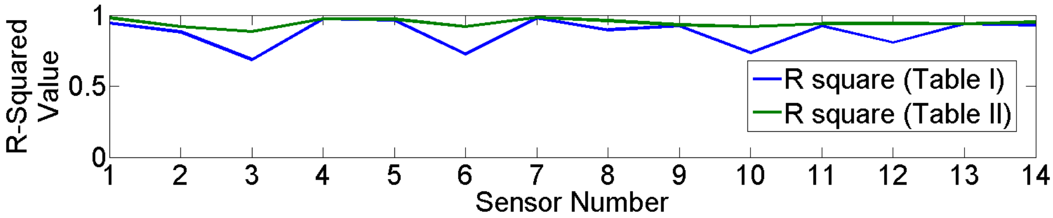

Figure 4-11 Comparison of R-square value between Table 4-1 and Table 4-2.

By comparing the R-squared values between Table 4-1 and 4-2 in Figure 4-11, it can be concluded that quadratic fitting for each sensing element have higher R-squared values than linear fitting. However, as shown in Table 4-3 the sensor has a reasonable linearity between sensor output and applied force with most of the R-squared values close to 1.

4.3.2. ACCURACY AND SHAPE DETECTION

After calibration, the accuracy of the proposed sensor is investigated. As for the static calibration procedure, the sensor is placed onto the linear actuator controlled manually and is in contact with the Force/Torque Nano17 sensor. The responses of one single sensing element and Nano17 sensor are illustrated in Figure 4-12. The test results demonstrate that the proposed sensor is capable of providing accurate measurements with a frequency of up to 10 Hz. In addition, it can be seen that the crosstalk between sensing elements is relatively small by using the particular mechanical design of the sensor. The root mean square error (RMSE) is 0.0184 N (less than 5% of total amplitude range). The accuracy of all sensing elements is presented in Figure 4-13, with the minimum value of 90%. The error is mostly due to the hysteresis effect of the rubber and light signal loss by fibre bending and connection [129], which will be considered in the future research related to both hardware and software.

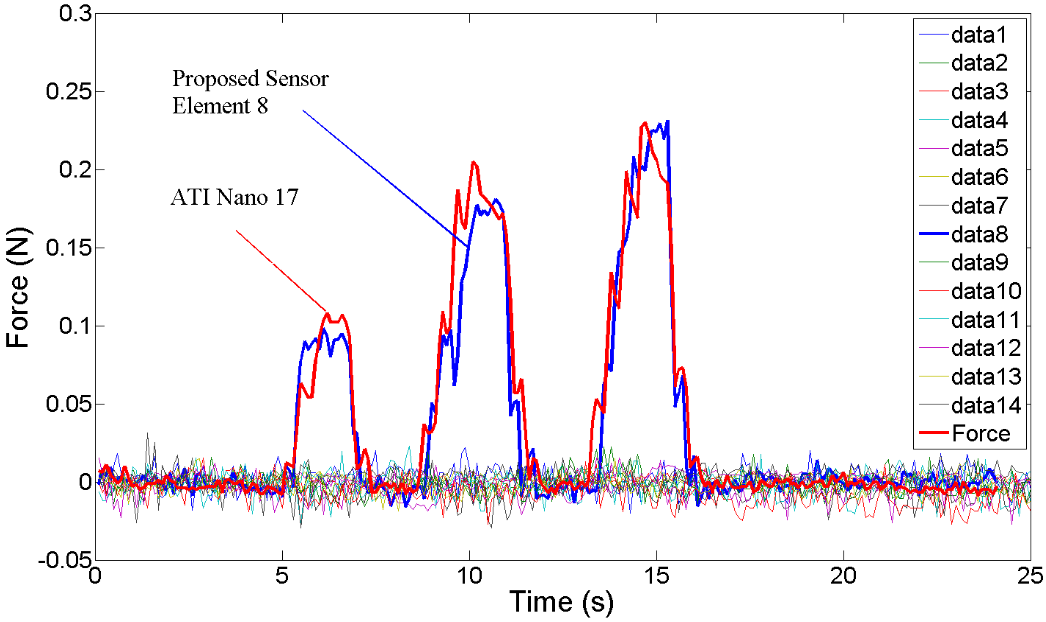

Figure 4-12 Proposed sensor responses under inputs with variable amplitudes from commercial force sensor.

After evaluating individual sensing elements of the probe head, shape detection tests are conducted using a cylindrical plastic object with flat round tip fixed on the platform. Then the probe head is placed vertically downward to the object until a firm contact with the object occurs, shown in Figure 4-14. To intuitively view the test results, the responses of all sensing elements are displayed according to their placement shape on the probe head, as shown in Figure 4-15. From the results, it can be seen that the four sensing elements which are in contact with the object detect forces larger than 0.05 N, while the other 10 sensing elements' responses are measured within the noise range of ± 0.03 N. The uneven force distribution on four contacting sensing elements may be caused by different contact angles between sensor and object, mechanical misalignment and the hysteresis effect. However, the detecting forces are all within0.05-0.15 N which guarantees the usefulness of shape detection.

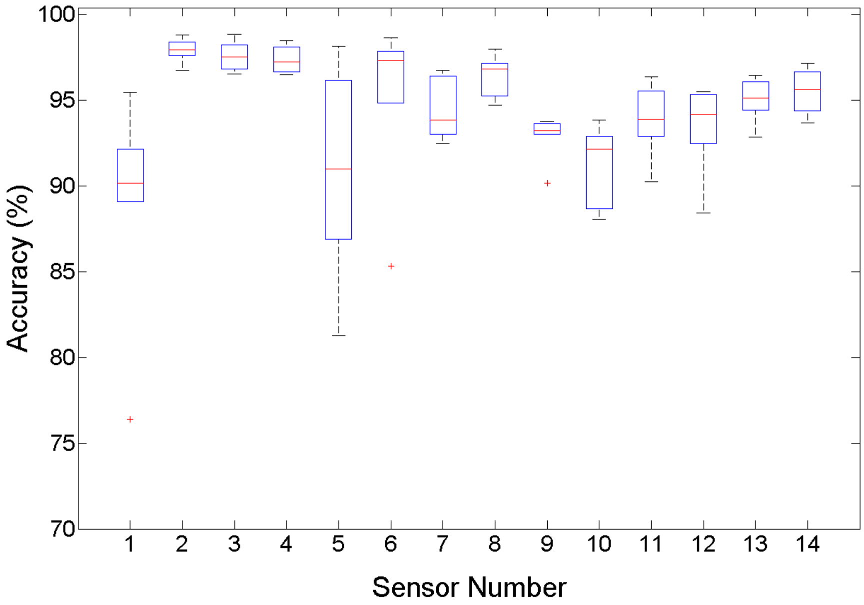

Figure 4-13 The accuracy of each sensing element on the tactile array probe head, where red line is the median and boxes represent the inter-quartile range.

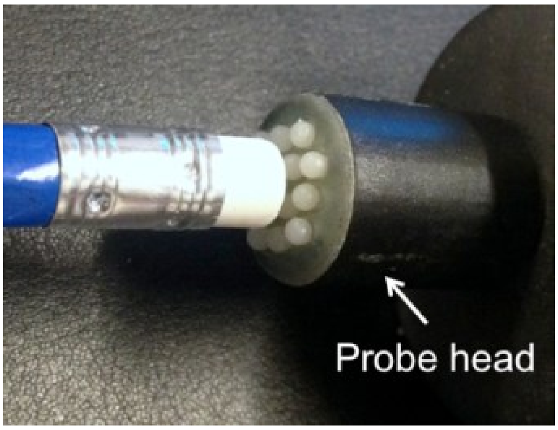

Figure 4-14 Shape detection test; a cylindrical object with flat round tip is in contact with four central sensing elements on the probe head.

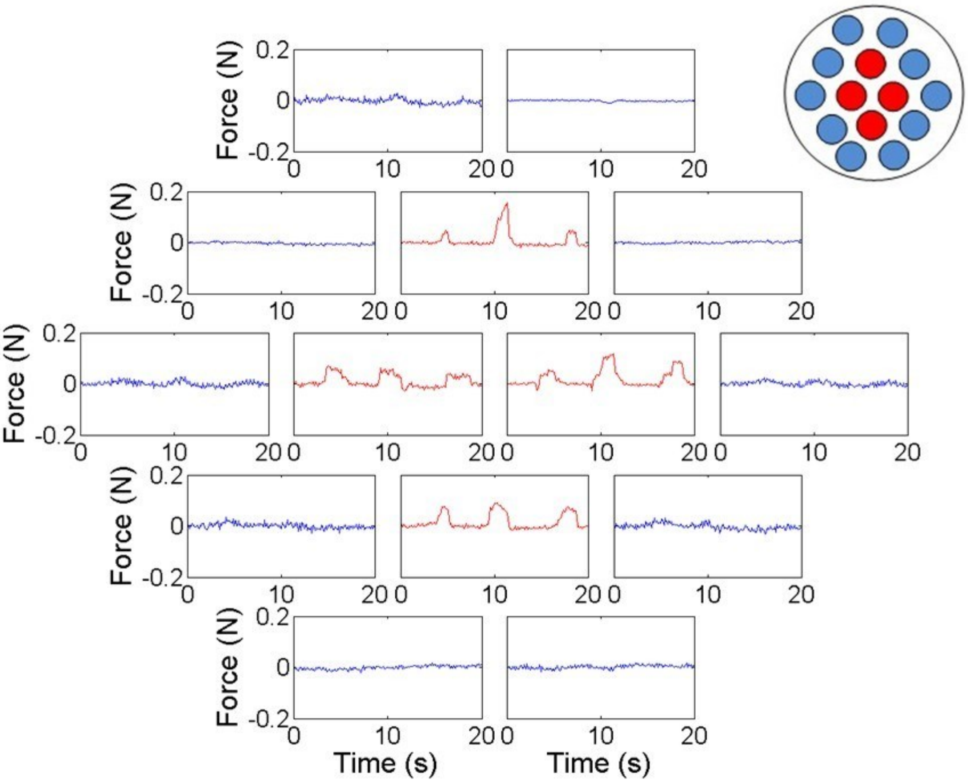

Figure 4-15 Displacements of the output of each sensing element on the probe head.

4.3.3. EXPERIMENTAL RESULTS OF TISSUE PALPATION

The tissue palpation experiment was conducted by mounting the tactile probe head on a robot arm (Mitsubishi RV-6SL). The connector between tactile probe head and robot arm is designed in SolidWorks shown in Figure 4-16. It consists of two parts: the top part with three M2 screw holes connects to the platform on the robot arm, the bottom part in two pieces connects the probe head and top part. The bottom part has a hollow structure enabling optical fibres to go through.

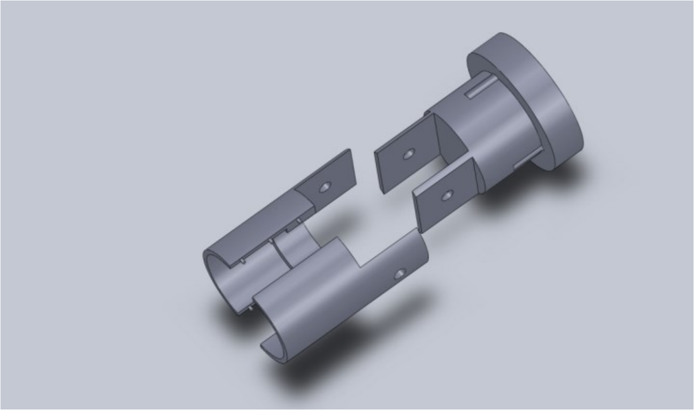

Figure 4-16 SolidWorks design of the connector between the tactile probe head and the robot arm.

During the tests, the probe head palpated on a planar surface silicone phantom tissue made of RTV6166 (General Electric Corp., CT, US) (ratio: 30/70, density: 1100 kg/m^3, attenuation: 3.45Np/m/MHz, Young's modulus: 15.3 kPa [90] [91]), shown in Figure 4-17. The silicone phantom has two spherical nodules (Staedtler Mars plastic 526-50, Staedtler Mars GmbH, Nurnberg, Germany) with the hardness of 47-50 Shore A, which are embedded at a depth of 6mm, as shown in Figure 4-18 (a). The tactile probe head was used to conduct a series of indentations on the phantom tissue surface to cover the area A where the 2 nodules were located (Figure 4-17). The indentation depth was 2mm; the lateral distance between two adjacent indentations was 14 mm which is the size of the probe head. Considering the light loss due to fibre bending, the tactile sensing units of the probe head were recalibrated after mounting on the robot arm. The palpation tests were repeated ten times, during which the bend radius of fibres was approximately constant. By fusing the palpating locations of the probe head and the locally measured force distributions by the probe, a force map was generated after palpating area A, as shown in Figure 4-18 (b), together with the standard deviation of each sensing element, shown in Figure 4-18 (c). Through a force map, locations of the hard nodules can be easily visualized. It was found from the tests that the interaction forces measured by the sensing elements exceeded the value 0.4 N when the probe was in contact with the nodule. Also, it can be seen that force measured on the left nodule is higher than on the right one, which is mainly due to the size of the nodule [26]. In the nodule free area, outputs of each sensing element varied mostly in the range of 0.15–0.25 N within which the noise level is of an acceptable range compared to the interaction force level. By increasing the spatial resolution of the tactile sensor, the shape of the nodule can also be detected.

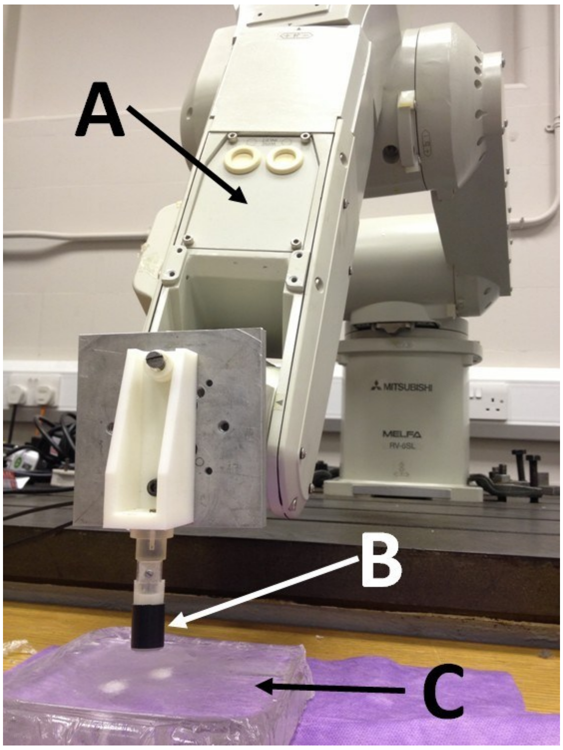

Figure 4-17 Integration of fibre optics tactile probe head with robot arm (A: Robot manipulator, B: Tactile probe head, C: Silicone phantom).

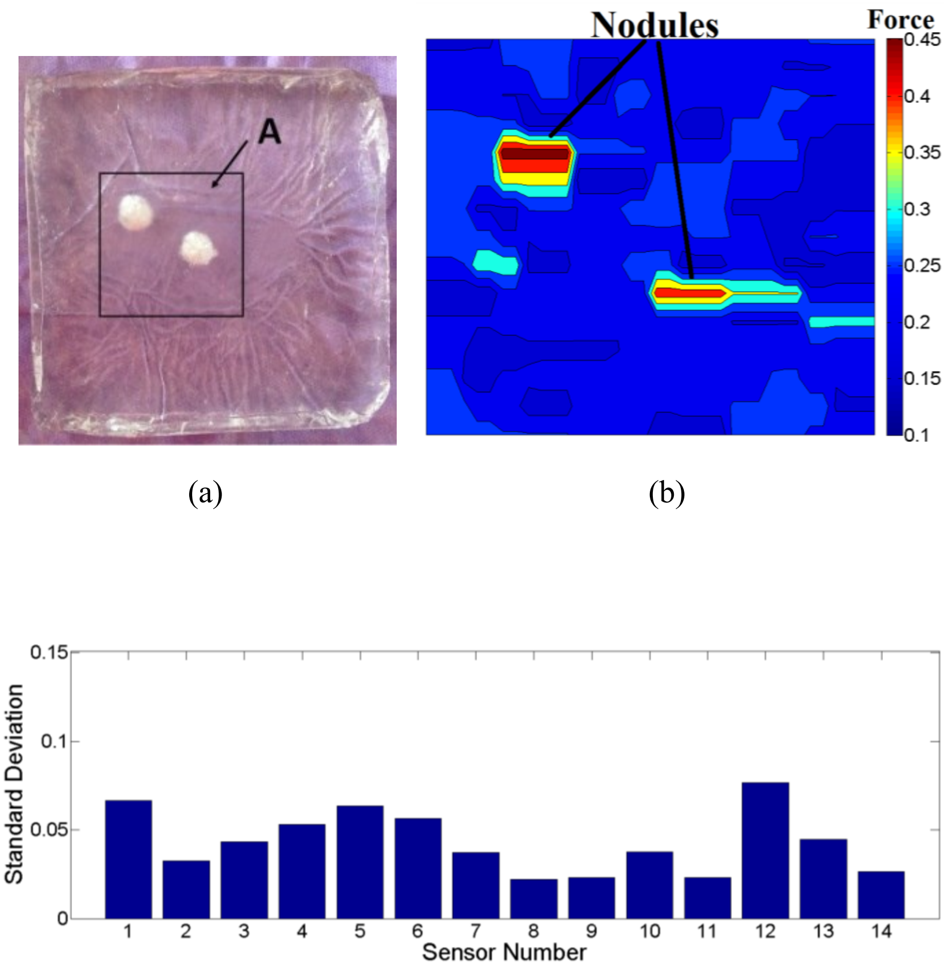

(a) (b)

(c)

Figure 4-18 (a) Palpation test in area A on silicone phantom tissue with two nodules embedded (diameter: left: 10 mm, right: 8 mm), (b) Test results of area A, (c) Standard deviation of each sensing element.

After evaluating the performance on silicone phantom tissue, a lamb kidney with an embedded nodule was tested. The nodule is made of rubber with the elastic modulus of 79.5 kPa tested by Instron 5565 (Instron, Canton, MA, US) [130]. The diameter of the nodule is 8mm and it is much stiffer than the lamb kidney, with a Young’s modulus of 5.9±0.7 kPa [131]. It was buried close to the kidney surface, shown in Figure 4-19 (a). As uneven tissue surface will influence the effectiveness of the stiffness map [132] generated by the developed tactile probe head, the hard nodule was embedded beneath a relatively flat area B for palpation testing. During tests, the probe palpated the kidney following the same procedure of palpating the silicone phantom to cover the area B. The test result for kidney palpation is shown in Figure 4-19 (b) (c). By combining sensor outputs and the palpating positions of the probe head, the force map of area B is created. It can be clearly seen from the force map that the forces concentrate in the central area of B which coincides with the location of the hidden nodule. The uneven force distribution from the rest of this stiffness map and the standard deviation of each sensing element during the repeated tests may be caused by the non-flat property of the tissue, together with the noise from shear force and fibre bending. Nevertheless, these values were kept in the range of 0–0.1 N which did not affect the effectiveness of tumour localization accuracy by using the tactile probe head. Compared to the silicone phantom tissue, lamb kidney is softer and can be easily damaged. This requires the palpation device to be flexible and sensitive, and the proposed one shows its capability of conducting accurate and effective tissue palpation for tissue abnormality detection.

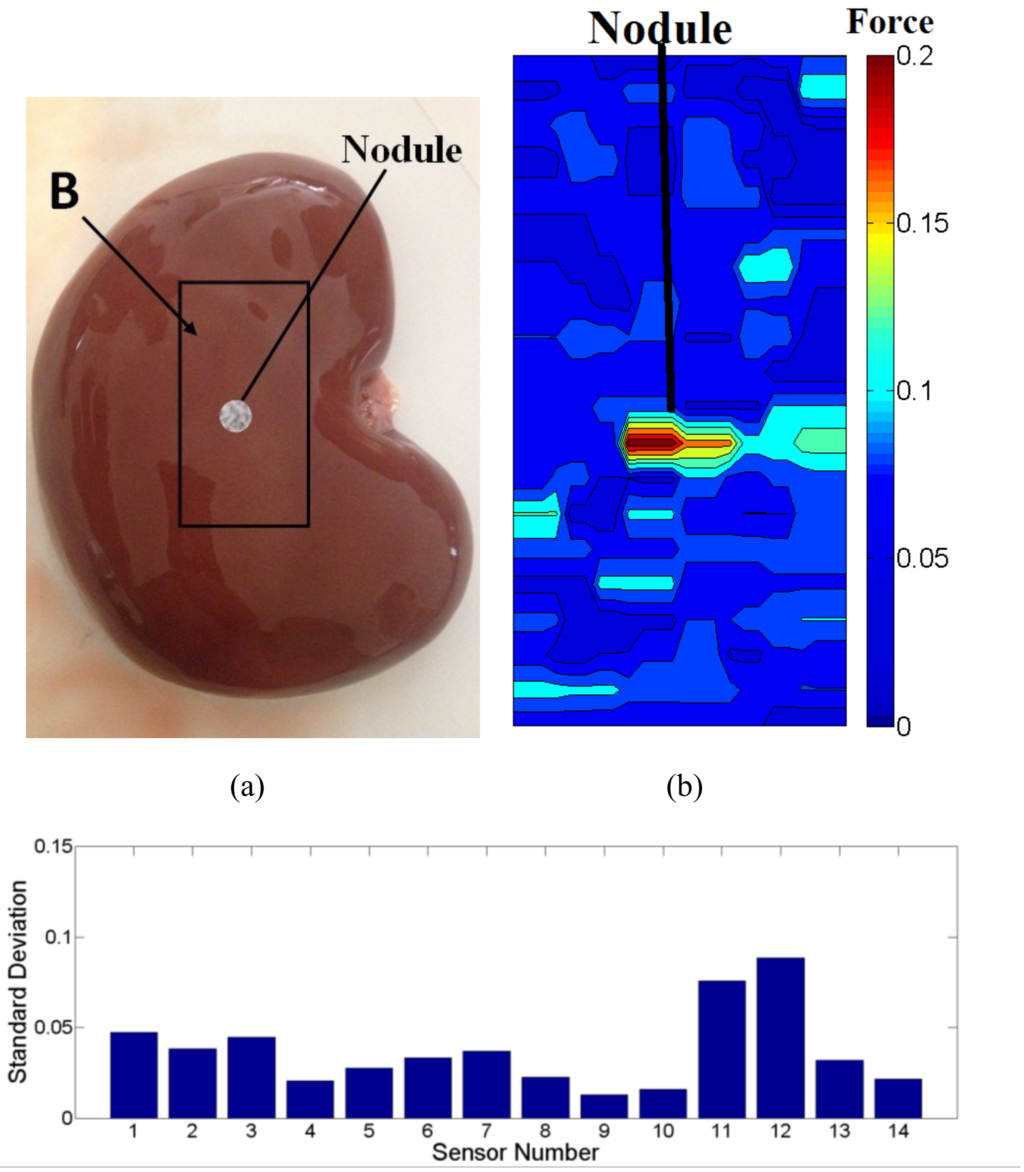

(a) (b)

(c)

Figure 4-19 (a) Lamb kidney sample with invisible nodule buried in area B, (b) Test results of the tactile sensor, (c) Standard deviation of each sensing element.

4.4. CONCLUSIONS

The proposed laboratory prototype tactile probe head can measure the normal force and its spatial distribution over the sensor's surface based on light intensity modulation, and shows potential for detecting abnormal tissue during palpation both in an open surgery and during MIS. Each tactile element has a micro-structure inside converting tissue reaction force applied to sensing nodes into a circular image pattern through transmitting and receiving fibres. The image patterns of all the sensing elements are captured by a camera attached at the proximal end of receiving fibres and are converted to tactile force feedback through image processing. Validation tests showed that each sensing element of the tactile probe head can measure forces from 0 to 0.5 N with a resolution of 0.05 N. Experiments were performed for testing the probe's capability of detecting the tissue abnormality through spatial distribution of tactile force feedback. Results show that the proposed tactile probe head can accurately and effectively detect a nodule embedded inside soft tissue. The proposed sensing probe is low cost, lightweight, sterilizable and easy to be miniaturized. As no metallic material and no electrical signals are used in the sensing area, this sensor could be used in an MRI environment. As the current tactile probe head provides only uniaxial force feedback, the missing force information in x- and y-directions will be addressed in the following chapter.

Chapter 5 A Two Axis Ring-Shaped Tactile Sensor using Optical Fibres

This chapter presents a two dimensional ring-shaped tactile sensor to provide the information of both magnitude of applied force and contact location. This tactile sensor is developed to equip the tactile probe in Chapter 4 with a sensation of force in x- and y-directions. The chapter first introduces the importance of tactile information in x- and y-directions. Then a mathematical model is developed to illustrate the sensing principle of the proposed sensor. Sensor design and silicone manufacturing is presented. It is worth mentioning that the proposed sensor is also MRI compatible, as is the tactile probe presented in earlier chapters. After evaluating the relationship between displacement/angle and force/voltage, the model of force calculation based on 3 voltage outputs is established. During model validation tests, results from sensor outputs and simulation outputs are compared and analysed.

5.1. INTRODUCTION

In the previous chapter the development of a uniaxial tactile array probe head was presented and tested. However, the proposed tactile probe head lacks the capability of force measurement in x- and y-directions. As the currently designed sensing elements are constrained by a structure to avoid shear forces, this information, can be further utilized for understanding tissue properties. There are several multi-axis sensors measuring tool-tissue contact force during MIS [133] [134] [135]. However, they are mostly single point sensors and not MRI compatible.

In the context of minimally invasive surgery, it is necessary to consider the medical equipment used and the forces introduced. Apart from the tip area of medical instruments which comes into contact with human tissues, there are many other contact points between instruments and environment that need to be carefully optimized [87]. A description of forces applied to the medical instruments in MIS is shown in Figure 5-1 [136]. Those interference factors are: friction between trocar and instrument shaft, the resistance of the abdominal wall during a lever movement; scaling and mirroring of tip forces and inefficiency of the instruments mechanism [31]. In a continuum robotic instrument, such as a catheter, forces applied along the access channel also need to be considered. In Figure 5-1, surgeons apply force directly or through a master-slave system at the handle and this force is influenced by the internal structure and friction of the instruments. Normally the force at the handle is two to six times bigger than the force at the tip [137]. At the trocar port location, other than the friction on the trocar, the force applied on the instrument is also caused by the movements of the instrument, such as tilting, against the abdominal wall [138]. At the instrument shaft, forces from nearby organs or tissues may be introduced to the system, especially to flexible instruments in natural orifice and catheter-based procedures [136]. The measurement of friction force generated between surgical instruments and the inner part of the trocars have been achieved by several researchers [139] [140]. However, the measurement of forces along the instrument shaft caused by surrounding tissues is yet to be investigated.

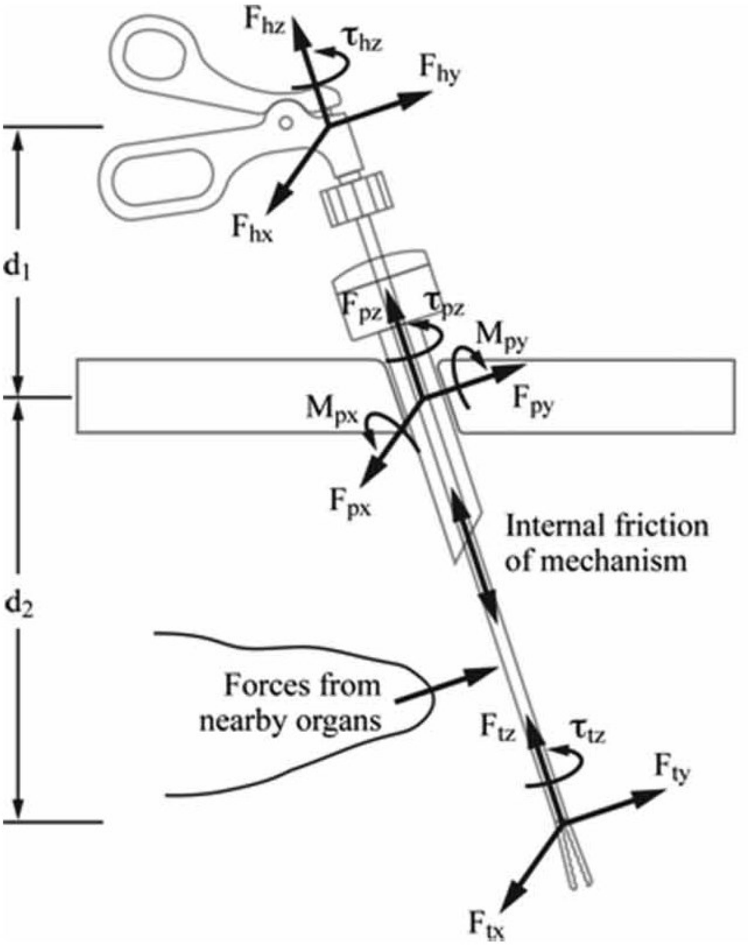

Figure 5-1 Forces acting on minimally invasive instruments [136].

This chapter presents a two axis contact sensor that can be incorporated into medical instruments along the shaft for use in minimally invasive surgery. As force at the instrument tip can be easily affected or masked by other forces applied on the instrument [141], it is important to equip the uniaxial tactile probe head in Chapter 4 with additional sense of touch on x- and y-directions. The fibre optic sensing system has been explored as it is small in size, lightweight, free from electromagnetic interference, water and corrosion resistant and capable of operating in harsh environment. When only a small number of optical fibres is employed in this system, the previously described camera system loses its advantage in multi-elements detection. Thus in this case, Keyence (FS-N11MN, KEYENCE CO., Japan) was used due to its advantage in high sensitivity, high frequency and less noise. By detecting the intensity change of three pairs of optical fibres, contact location together with force magnitude can be determined. In contrast to conventional sensing principles, the proposed sensor is capable of working in the highly electromagnetic MRI environments by utilizing fibre-optics sensing.

5.2. METHODOLOGY

5.2.1. SENSING PRINCIPLE

An optical fibre-based force sensor consists of a light source, transduction element and optical detector. It is small in size, lightweight, has low power consumption and is capable of working in high electromagnetic noise environment. There are four main modulations of optical fibre, which are wavelength, phase, polarization and intensity.

The light intensity modulation mechanism is being used due to its low-cost, easy fabrication and temperature insensitivity. The schematic design of the proposed sensor is shown in Figure 5-2.

The sensor comprises three main parts, namely, the outer ring, inner cylinder, and flexible material in between. Six optical fibres are embedded in the inner ring, of which three are light transmitting fibres and three are light receiving fibres. Light is transmitted from light source to the tip of the transmitting fibre, and it is then received by the receiving fibre by the reflection of a mirror placed against them. The angle between transmitting and receiving fibres is 60° as it is able to achieve good sensitivity without too much bending of fibre tips [129]. When force is applied along the x-y directions, the flexible material will deform causing the stiff outer ring to shift. The three mirrors attached to the outer ring will shift accordingly changing the displacement between the fibre tips and the mirrors. Based on the optical fibre-based intensity modulation model [82], this displacement change is observed by the light intensity change of the receiving fibre, which is then detected by an optical detector. The detector, coupled at the end of each receiving fibre, transforms the light signal into voltage data. The data is collected by a DAQ (Data Acquisition) card and sent to the computer for analysis. By applying a geometry-based algorithm, which will be further explained in the following section, the contact point and the magnitude of force applied can be determined.

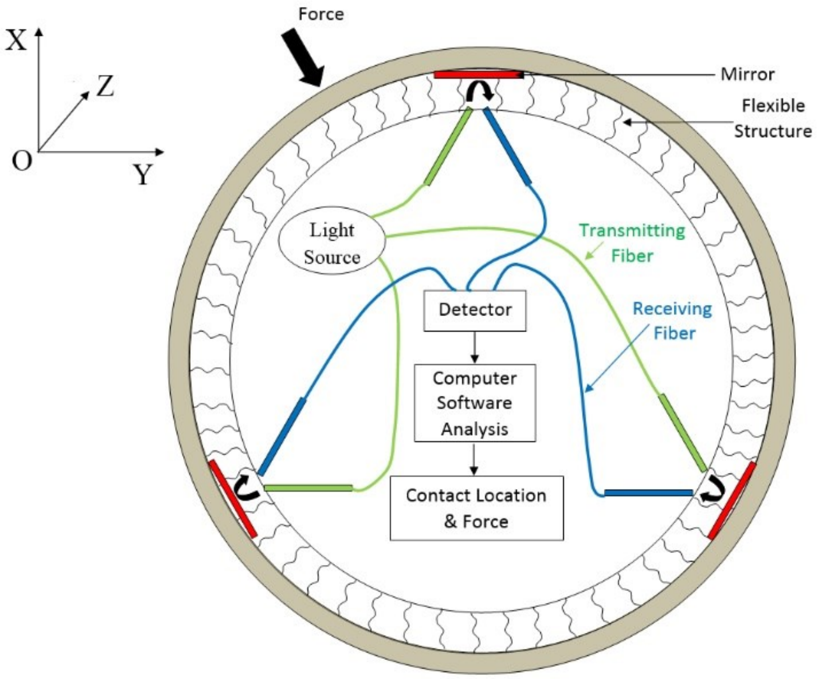

Figure 5-2 Schematic design of proposed tactile sensor.

5.2.2. SENSOR DESIGN & FABRICATION

Based on the schematic design shown in Figure 5-2, a 3-D drawing of the proposed sensor is created in SolidWorks 2013 (Dassault Systems, MA, US), exported as an STL-file, and manufactured by a 3D printer (ProJet HD 3000 Plus, 3D-Systems, SC, US), shown in Figure 5-3. Using acrylonitrile butadiene styrene (ABS) material which is lightweight and compatible with MRI, the 3D objects are sliced horizontally by the printer based on the STL file and created via the additive process which deposits ABS material layer by layer on a bed of supporting material [142]. Afterwards, the supporting material was removed from the prototype by putting it into an oven at a temperature of 75 degrees.

The section view together with the size description of the design is shown in Figure 5-3. The diameter of the inner cylinder is 7 mm with a hole in the middle, allowing the sensor to be fixed by a M2 thread on the calibration platform. Three pairs of optical fibres are embedded in the cylinder at an angle of 120^o, while fibre tips of each pair are facing each other at 60^o as explained earlier. The outer ring is 14 mm in diameter and 1.5 mm in thickness, with three reflective surfaces (aluminium foil tape, Maplin Electronics Ltd, UK) attached inside to transmit light from three pairs of optical fibre. The optical fibre (SH1001, Mitsubishi Rayon Co., Ltd., Tokyo, Japan) chosen for this prototype has a diameter of 1 mm (with jacket), shown in Figure 5-3.

In order to make the appropriate flexible structure for the proposed sensor, a mould is designed in SolidWorks and printed by the 3D printer, shown in Figure 5-4 (a) (b). To successfully remove the silicone after moulding, the mould consists of three parts which can be easily disassembled, base, inner cylinder, and is constrained with three inner protrusions. The protrusions are designed to allow the silicone to have three rectangular holes, which are the same size as the mirror on the outer ring. The holes enable light to be freely transmitted from transmitting fibres to receiving fibres, and without being blocked by any silicone material. The silicone is fabricated by mixing Ecoflex 0050 (Smooth-on Inc., PA, US) at a ratio of A: B=1: 1 (Shore Hardness = 00-50 Tensile Modulus = 83 kPa) and pouring it into the mould. After the silicone is cured, the mould is disassembled. The silicone prototype is shown in Figure 5-4 (c). The silicone has an outer diameter of 11 mm and an inner diameter of 7 mm. The size of each of the three interspaces on the side of silicone is $2mm \times 4mm$, allowing the reflection of light from transmitting fibre to receiving fibre.

The tips of optical fibres are cut using a fibre cutter (POF Cutter Block, Industrial Fibre Optics Inc., AZ, US) and inserted into the inner cylinder. The sensor prototype is shown in Figure 5-5.

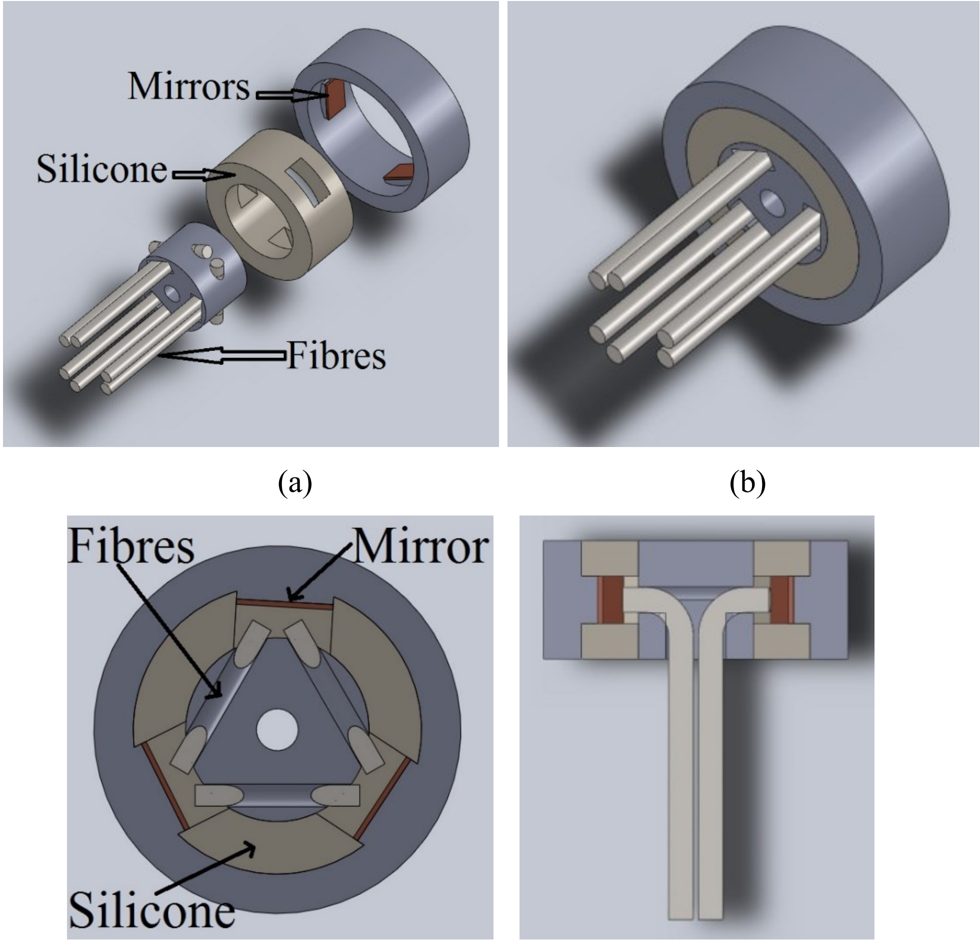

(a) (b)

(c) (d)

Figure 5-3 3D model of developed tactile sensor: (a) before assembly, (b) assembled, (c) top view, (d) side view.

(a) (b) (c)

Figure 5-4 Manufacturing process of silicone model: (a) 3D mould design, (b) mould after 3D printed, (c) flexible silicone structure.

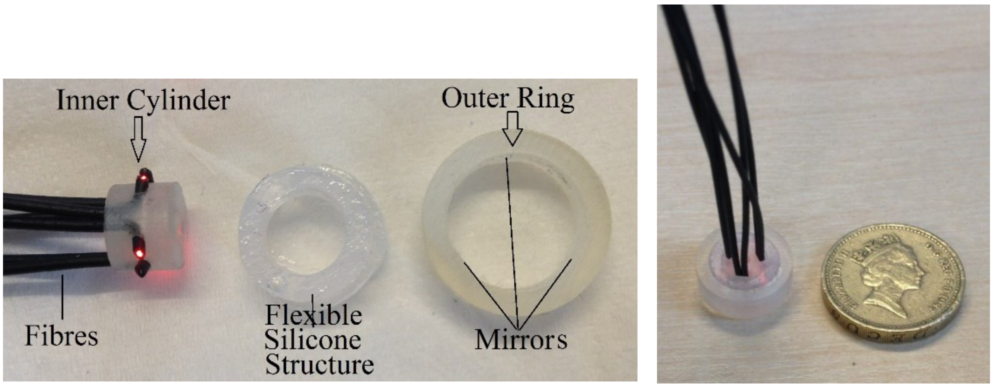

(a) (b)

Figure 5-5 Sensor realization: (a) before assembly, (b) assembled.

5.2.3. MATHEMATICAL MODEL

To further illustrate the sensing principle of the proposed tactile sensor, a geometric model is established using three sensing elements, shown in Figure 5-6. The inner circle represents the inner cylinder which is used for fixing fibres and the outer circle represents the outer ring which has three mirrors attached. The optical fibres are assembled in a way that the centres of their tips are fixed at points D, E and G. The mirrors (marked in red) on the outer ring are perpendicular to the fibres and their middle points on x-y axis are marked as A, B and C. When force is applied on the sensor, the outer ring will shift causing a position change of the three mirrors (marked in dashed red). The light intensity modulation mechanism is based on the light intensity change caused by distance changes between mirrors and fibres - AD, BE and CG in this model. The light transmitted to the detector is converted into an electrical signal, in this case into voltage. By utilizing the linear range of the light intensity model [82], the relation between outputs of the detectors ($\mathrm{V_a}$, $\mathrm{V_b}$ and $\mathrm{V_c}$) and displacement between fibres and mirrors (AD, BE and CG) are defined as

$$\mathrm{V_a} \propto -\mathrm{K_a} \cdot |\mathrm{AD}|, \tag{5.1}$$

$$\mathrm{V_b} \propto -\mathrm{K_b} \cdot |\mathrm{BE}|, \tag{5.2}$$

$$\mathrm{V_c} \propto -\mathrm{K_c} \cdot |\mathrm{CG}|, \tag{5.3}$$

where $\mathrm{K_a}$, $\mathrm{K_b}$, $\mathrm{K_c}$ are the transforming factors of detectors converting distance to voltage. Due to the symmetric structure of the ring shaped sensor, the distances from the tip of fibres to mirrors are

$$|\mathrm{AD}| = |\mathrm{BE}| = |\mathrm{CG}|. \tag{5.4}$$

Considering the different properties of individual detectors and the errors during fibre assembly, it is assumed that the factors are different and will be determined individually during the calibration process in the following section.

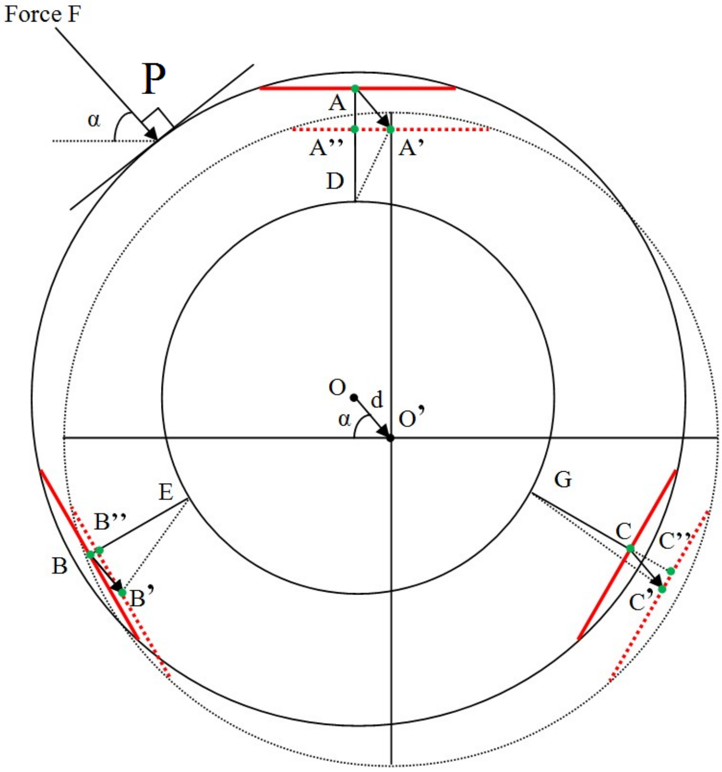

Figure 5-6 Geometric model of tactile sensor.

The sensing area is divided into 6 sections (Figure 5-7), and the relationship between distance changes of each sensing element and contact location is analysed, Table 5-1.

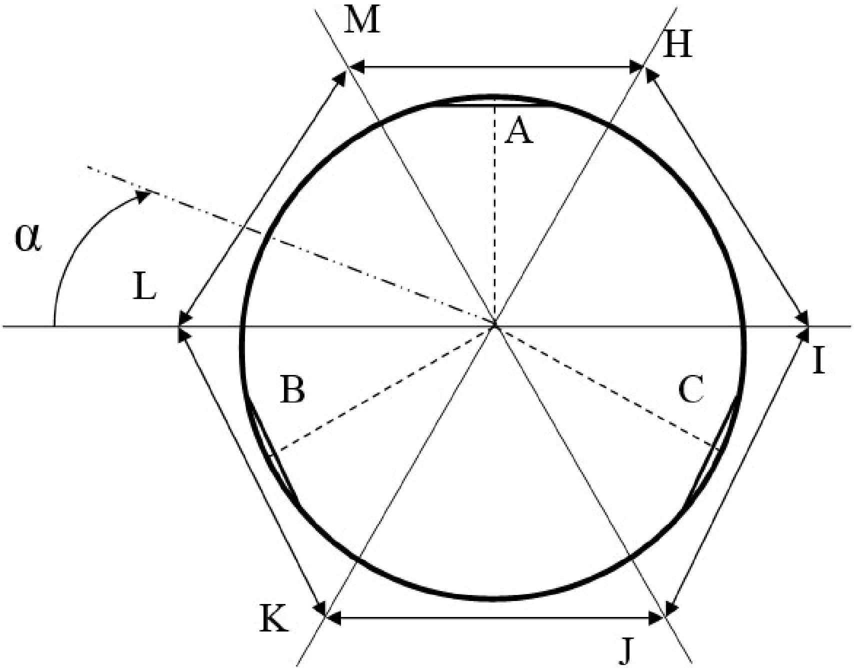

Figure 5-7 Geometric Segmentation.

Table 5-1 Relation between contact location and displacement change of three sensing points

Displacement change	H to I	I to J	J to K	K to L	L to M	M to H
$\|AD\| - \|A''D\|$	+	-	-	-	+	+
$\|BE\| - \|B''E\|$	-	-	+	+	+	-
$\|CG\| - \|C''G\|$	+	+	+	-	-	-

where '+' means positive and '-' means negative. Due to the inverse relation between displacement and voltage (Equation 5.1-5.3), the relation between voltage and contact location are shown in Table 5-2.

Table 5-2 Relation between voltage change and contact location

Voltage	H to I	I to J	J to K	K to L	L to M	M to H
$V_a - V_a'$	-	+	+	+	-	-
$V_b - V_b'$	+	+	-	-	-	+
$V_c - V_c'$	-	-	-	+	+	+

The direction of the force can be detected between those six sections only by looking into the positive/negative changes of the voltages from the three detectors (i.e. increase/decrease of voltage outputs compared to no-load voltage). For example, if the voltage from the detector B decreases while the voltage from the other two increases, it can be concluded that the force is applied in the area of K to L.

In the presented model, the inner cylinder is fixed while the outer ring is capable of x-y axis movements. When a force F is applied on the sensor at point P with an angle of α (Figure 5-6), in respect to the x-axis, the outer ring shifts with a distance of d_s while the inner cylinder stays the same. The centre point of the outer ring shifts from O to O' according to the vector of F, together with the centre points of three mirrors A, B and C to A', B' and C' with the same distance d_s and angle α,

$$|AA'| = |BB'| = |CC'| = |OO'| = d_s, \tag{5.5}$$

$$\angle AA'A'' = \alpha,\ \angle BB'B'' = \frac{\pi}{3} - \alpha,\ \angle CC'C'' = \frac{2\pi}{3} - \alpha. \tag{5.6}$$

The distances of points D, E and G to their relevant mirrors then changes from L to $|A''D|$, $|B''E|$ and $|C''G|$ accordingly,

$$|A''D| = |AD| - |AA''|, \tag{5.7}$$

$$|B''E| = |BE| - |BB''|, \tag{5.8}$$

$$|C''G| = |CG| + |CC''|. \tag{5.9}$$

By analysing the geometric model, they can be expressed as

$$|AA''| = |AA'| \cdot \mathit{sin}\angle AA'A'', \tag{5.10}$$

$$|BB''| = |BB'| \cdot \sin\angle BB'B'', \tag{5.11}$$

$$|CC''| = |CC'| \cdot \sin\angle CC'C''. \tag{5.12}$$

Then the outputs of detectors are changed accordingly to

$$V_a' \propto -K_a \cdot |A''D|, \tag{5.13}$$

$$V_b' \propto -K_b \cdot |B''E|, \tag{5.14}$$

$$V_c' \propto -K_c \cdot |C''G|. \tag{5.15}$$

Substituting (5.1) to (5.12) into (5.13), (5.14) and (5.15), we get

$$d_s \propto \frac{\Delta V_a}{K_a \cdot \sin\alpha} = \frac{\Delta V_b}{K_b \cdot \sin(\frac{\pi}{3} - \alpha)} = \frac{\Delta V_c}{K_c \cdot \sin(\frac{2\pi}{3} - \alpha)}, \tag{5.16}$$

where $\Delta V_a = V_a' - V_a$, $\Delta V_b = V_b' - V_b$, $\Delta V_c = V_c' - V_c$. Thus

$$\alpha = \mathit{arctan}\frac{\sqrt{3}K_b \cdot \Delta V_a}{K_b \cdot \Delta V_a + 2K_a \cdot \Delta V_b}$$

$$= \mathit{arctan}\frac{\sqrt{3}(K_b \cdot \Delta V_c - K_c \cdot \Delta V_b)}{K_b \cdot \Delta V_c + K_c \cdot \Delta V_b}$$

$$= arctan\frac{\sqrt{3}\mathrm{K_c}\cdot\Delta\mathrm{V_a}}{\mathrm{K_c}\cdot\Delta\mathrm{V_a}+2\mathrm{K_a}\cdot\Delta\mathrm{V_c}}, \tag{5.17}$$

$$d_s = \frac{2\sqrt{(\mathrm{K_b}\cdot\Delta\mathrm{V_a}+\mathrm{K_a}\cdot\Delta\mathrm{V_b})^2-\mathrm{K_a}\mathrm{K_b}\cdot\Delta\mathrm{V_a}\Delta\mathrm{V_b}}}{\sqrt{3}\mathrm{K_a}\cdot\mathrm{K_b}}.$$

$$= \frac{2\sqrt{(\mathrm{K_b}\cdot\Delta\mathrm{V_c}-\mathrm{K_c}\cdot\Delta\mathrm{V_b})^2+\mathrm{K_b}\mathrm{K_c}\cdot\Delta\mathrm{V_b}\Delta\mathrm{V_c}}}{\sqrt{3}\mathrm{K_b}\cdot\mathrm{K_c}}$$

$$= \frac{2\sqrt{(\mathrm{K_a}\cdot\Delta\mathrm{V_c}+\mathrm{K_c}\cdot\Delta\mathrm{V_a})^2-\mathrm{K_a}\mathrm{K_c}\cdot\Delta\mathrm{V_a}\Delta\mathrm{V_c}}}{\sqrt{3}\mathrm{K_a}\cdot\mathrm{K_c}} \tag{5.18}$$

In this model, $\mathrm{K_a}$, $\mathrm{K_b}$, $\mathrm{K_c}$ and $\mathrm{V_a}$, $\mathrm{V_b}$, $\mathrm{V_c}$ are known parameters, $\mathrm{V_a}'$, $\mathrm{V_b}'$, $\mathrm{V'_c}$ are the outputs of the sensor, thus the angle and displacement α and d which are caused by the force can be calculated. The validation of this model and the relation between the magnitude of applied force and the displacement change will be further discussed in the following section.

5.3. EXPERIMENTAL RESULTS

5.3.1. TEST SET-UP

The experimental set-up for tactile sensor testing is shown in Figure 5-8. A standard Force/Torque sensor (Nano 17, ATI Industrial Automation, NC, US) together with a data acquisition card (NI USB-6341, National Instruments, TX, US) is used for calibrating the proposed tactile sensor. Another data acquisition card (NI USB-6341, National Instruments, TX, US) is used for controlling and collecting movement data from a linear actuator powered by a brushless motor (Maxon EC-30, Switzerland). Three pairs of optical fibres (core diameter 0.25 mm, 1 mm with jacket, reflective index

1.49, and numerical aperture 0.50) are used for transmitting and receiving light. Three Keyence (FS-N11MN, KEYENCE CO., Japan) are used as both light sources and detectors.

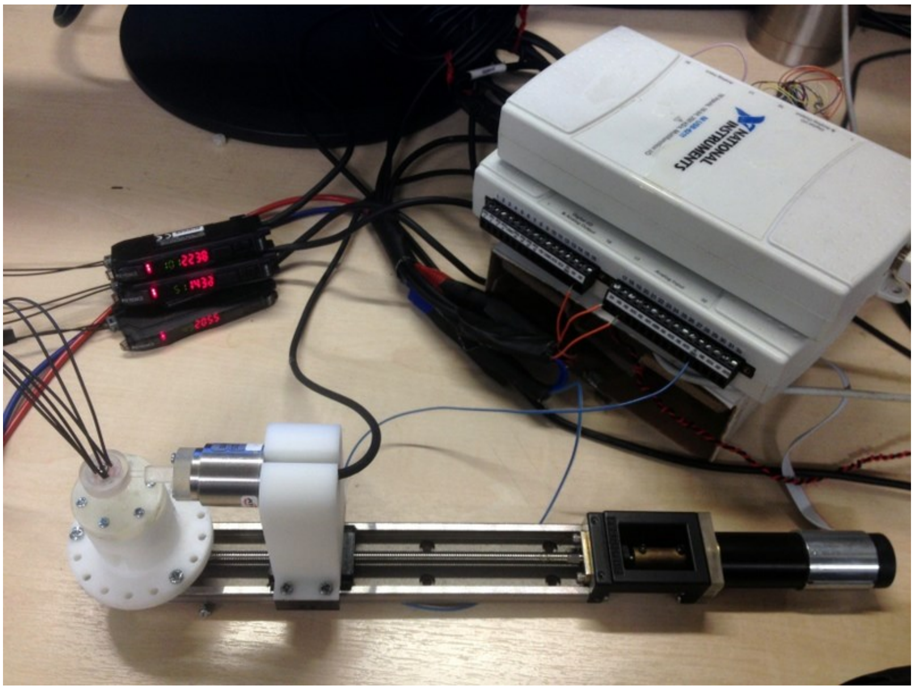

Figure 5-8 Equipment set-up.

5.3.2. SENSOR CALIBRATION

To determine the parameters from the above mathematical model, a series of tests has been conducted. The proposed sensor was mounted on a rigid static base which has 12 marked points at its circular edge, at the angle of 30 degrees. The base is fixed at the end of the linear actuator, which has a resolution of 1.5 µm. The Nano 17 sensor is connected to the linear rail with a probe fixed at its tip. By moving the probe towards the proposed sensor on the x-y directions, shown in Figure 5-9, real-time data from the proposed sensor and the ATI sensor are acquired and sent to the computer.

Figure 5-9 Calibration procedure.

In order to find out the relationship between the magnitude of applied force and silicone deformation, the experiment is conducted on the points A, B and C, shown in Figure 5-6. At these three points, the displacement change of silicone is equal to the displacement change (voltage) from one of the three mirrors and its corresponding fibre tips, thus the relationship between force and silicone deformation can be determined. The tests are conducted 3 times and the data from the linear actuator, Nano 17 sensor and Keyence are recorded at a sampling rate of 100Hz. Figure 5-10 demonstrates the experiment results of point A, including the movement of linear actuator, optical sensor response at point A, point B, point C and the response force measured using the Nano 17.

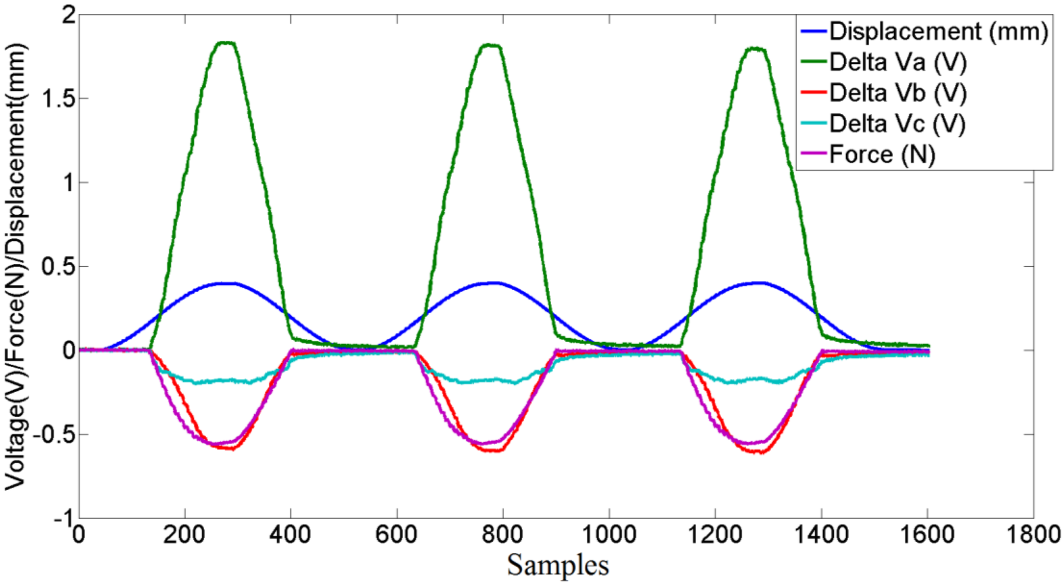

Figure 5-10 Experiment results at point A. Displacement indicate the linear rail's movement, Delta Va, Delta Vb, Delta Vc denote the voltage changes at A, B and C.

The relationship between distance change (between fibre tip and mirror) and voltage output is shown in Figure 5-11. The linear relationship of point A, B and C between displacement change and voltage output are represented by

$$\Delta V_a = K_a \cdot d_a + \mu_a, \tag{5.19}$$

$$\Delta V_b = K_b \cdot d_b + \mu_b, \tag{5.20}$$

$$\Delta V_c = K_c \cdot d_c + \mu_c, \tag{5.21}$$

where $\Delta V_a, \Delta V_b, \Delta V_c$ are the changes of voltage outputs of three sensing elements, d_a, d_b, d_c are the displacements at three points, K_a, K_b, K_c, μ_a, μ_b, μ_c are the calibration coefficients, which listed in Table 5-3 together with respective R-squared values.

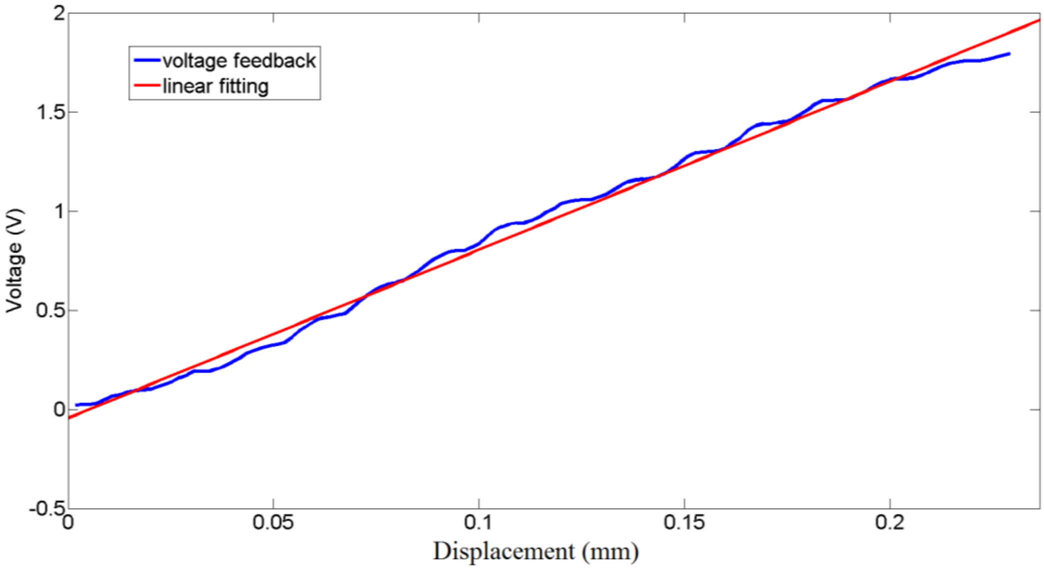

Figure 5-11 Relationship between displacements and voltage outputs at the point A.

Table 5-3 Coefficient of Linear Fitting Curve Between Voltage and Displacement

Point	**Coefficients**			**Variance**
	KV	μ	R_o^2	
a	8.25	0.044	0.995	0.0152
b	3.19	-0.09	0.9418	0.0832
c	0.88	-0.1	0.5608	0.0181

The relationship between silicone deformation and magnitude of applied force is shown in Figure 5-12. The linear relationship of the points A, B and C between the displacement and a magnitude of applied force are represented by

$$f = Kf_a \cdot d_1 + \varepsilon_a, \tag{5.22}$$

$$f = Kf_b \cdot d_2 + \varepsilon_b, \tag{5.23}$$

$$f = Kf_c \cdot d_3 + \varepsilon_c, \tag{5.24}$$

where f is the magnitude of applied force, d_1, d_2, d_3 are the displacements of the outer ring during three tests and Kf_a, Kf_b, Kf_c, ε_a, ε_b, ε_c are the calibration coefficients, which are listed in Table 5-4 together with respective R-squared values.

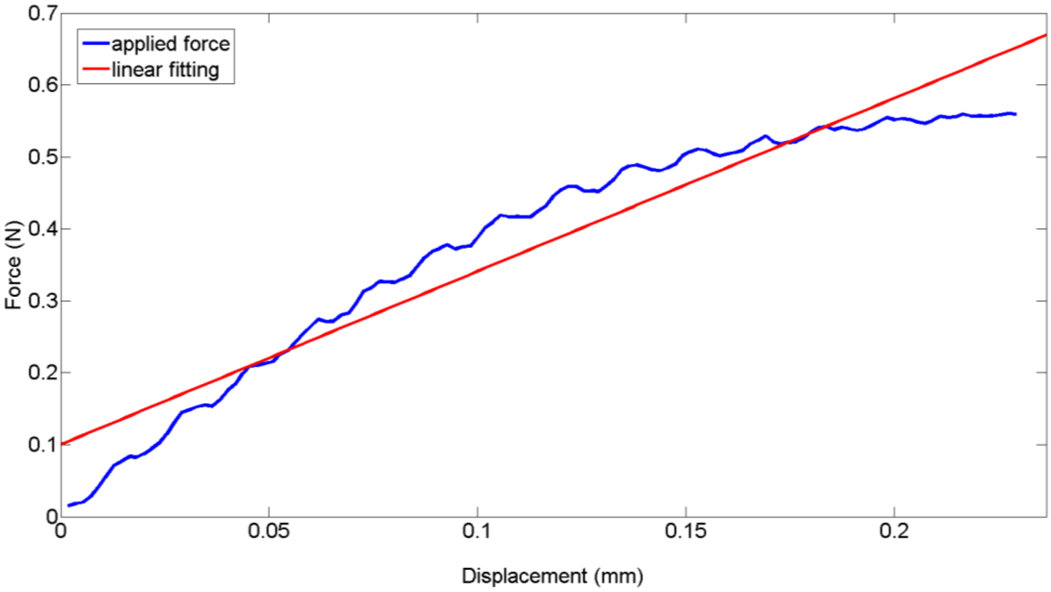

Figure 5-12 Relationship between displacements and magnitude of applied force at point A.

Table 5-4 Coefficient Linear Fitting Curve Between Force and Displacement

Point	**Coefficients**			**Variance**
	Kf	ε	R_o^2	
a	2.42	0.1	0.9231	0.0037
b	3.41	0.024	0.9875	0.0128
c	2.64	0.036	0.991	0.0145

5.3.3. MODEL VALIDATION

As explained in the previous section, $d_1 = d_a$ at point A, $d_2 = d_b$ at point B, and $d_3 = d_c$ at point C. Substituting (5.19) to (5.24) into (5.16), we get

$$f = \frac{\Delta \mathrm{V_a}}{\frac{\mathrm{K_a}}{Kf_a}\cdot \sin\alpha} = \frac{\Delta \mathrm{V_b}}{\frac{\mathrm{K_b}}{Kf_b}\cdot \sin(\frac{\pi}{3}-\alpha)} = \frac{\Delta \mathrm{V_c}}{\frac{\mathrm{K_c}}{Kf_c}\cdot \sin(\frac{2\pi}{3}-\alpha)} \tag{5.25}$$

Thus

$$\alpha = arctan\frac{\sqrt{3}\frac{\mathrm{K_b}}{Kf_b}\cdot \Delta \mathrm{V_a}}{\frac{\mathrm{K_b}}{Kf_b}\cdot \Delta \mathrm{V_a}+2\frac{\mathrm{K_a}}{Kf_a}\cdot \Delta \mathrm{V_b}}$$

$$= arctan\frac{\sqrt{3}(\frac{\mathrm{K_b}}{Kf_b}\cdot \Delta \mathrm{V_c}-\frac{\mathrm{K_c}}{Kf_c}\cdot \Delta \mathrm{V_b})}{\frac{\mathrm{K_b}}{Kf_b}\cdot \Delta \mathrm{V_c}+\frac{\mathrm{K_c}}{Kf_c}\cdot \Delta \mathrm{V_b}}$$

$$= arctan\frac{\sqrt{3}\frac{\mathrm{K_c}}{Kf_c}\cdot \Delta \mathrm{V_a}}{\frac{\mathrm{K_c}}{Kf_c}\cdot \Delta \mathrm{V_a}+2\frac{\mathrm{K_a}}{Kf_a}\cdot \Delta \mathrm{V_c}}\,. \tag{5.26}$$

$$f = \frac{\sqrt[2]{(\frac{\mathrm{K_b}}{Kf_b}\cdot \Delta \mathrm{V_a}+\frac{\mathrm{K_a}}{Kf_a}\cdot \Delta \mathrm{V_b})^2 - \frac{\mathrm{K_a}}{Kf_a}\cdot\frac{\mathrm{K_b}}{Kf_b}\cdot \Delta \mathrm{V_a}\Delta \mathrm{V_b}}}{\sqrt{3}\frac{\mathrm{K_a}}{Kf_a}\cdot\frac{\mathrm{K_b}}{Kf_b}}$$

$$= \frac{\sqrt[2]{(\frac{\mathrm{K_b}}{Kf_b}\cdot \Delta \mathrm{V_c}-\frac{\mathrm{K_c}}{Kf_c}\cdot \Delta \mathrm{V_b})^2+\frac{\mathrm{K_b}}{Kf_b}\cdot\frac{\mathrm{K_c}}{Kf_c}\cdot \Delta \mathrm{V_b}\Delta \mathrm{V_c}}}{\sqrt{3}\frac{\mathrm{K_b}}{Kf_b}\cdot \mathrm{K_c}}$$

$$= \frac{\sqrt[2]{(\frac{\mathrm{K_a}}{Kf_a}\cdot \Delta \mathrm{V_c}+\frac{\mathrm{K_c}}{Kf_c}\cdot \Delta \mathrm{V_a})^2-\frac{\mathrm{K_a}}{Kf_a}\cdot\frac{\mathrm{K_c}}{Kf_c}\cdot \Delta \mathrm{V_a}\Delta \mathrm{V_c}}}{\sqrt{3}\frac{\mathrm{K_a}}{Kf_a}\cdot\frac{\mathrm{K_c}}{Kf_c}}\,. \tag{5.27}$$

From Table 5-1 and Table 5-2, the parameters between force and voltage can be calculated as

Table 5-5 Parameters between the force and voltage

Parameter	Value
$\frac{K_a}{Kf_a}$	3.4091
$\frac{K_b}{Kf_b}$	0.9355
$\frac{K_c}{Kf_c}$	0.3333

Using above parameters and given a force applied with the angle of $\alpha = 0$ and $\alpha = 30^o$, the comparisons of experimental data and simulated curve are shown in Figure 5-13 and Figure 5-14.

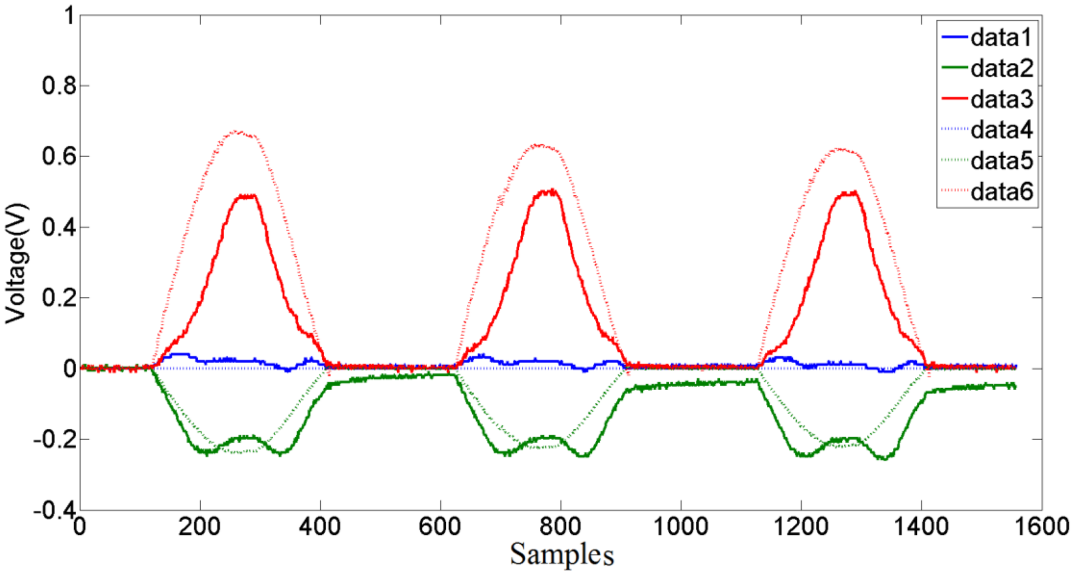

Figure 5-13 Experimental data (data 1-3: a-c) and output from the mathematical model (data 4-6: a-c) at $\alpha = 0$.

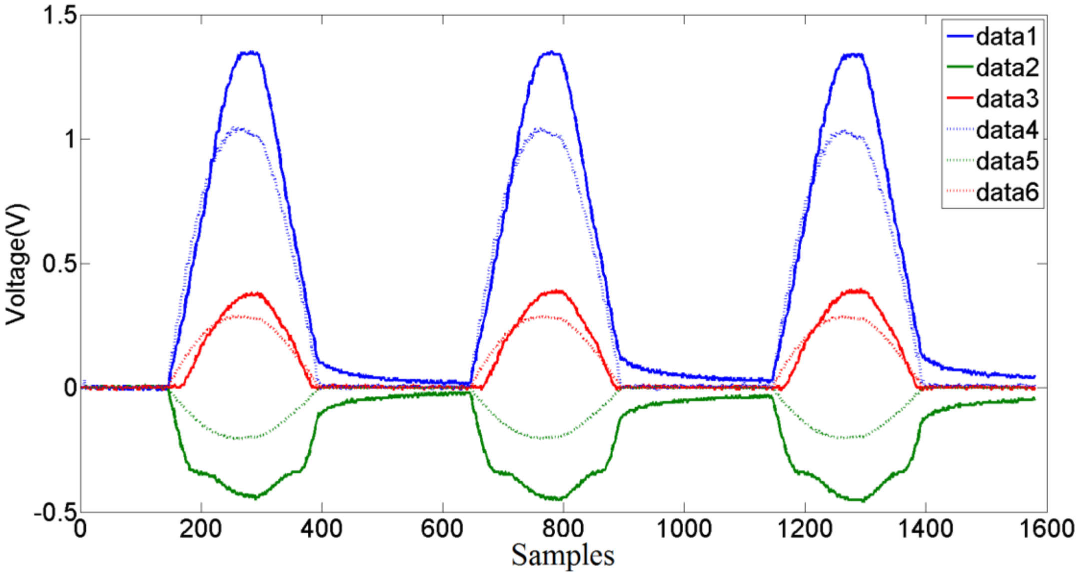

Figure 5-14 Experimental data (data 1-3: a-c) and output from mathematical model (data 4-6: a-c) at $\alpha = 30^o$.

The RMSE error and accuracy data are listed in Table 5-6 and Table 5-7 below. From the data, it can be concluded that the mathematical model is verified based on the similarity between the simulation data and experimental data. At certain locations, the accuracies are lower caused by the misalignment of fibres and different stiffness through the flexible material.

Table 5-6 RMSE between experimental data and simulated data

Angle	RMSE (a)	RMSE (b)	RMSE (c)	RMSE (average)
0	0.0143	0.1398	0.0526	0.0689
30^o	0.1300	0.0447	0.1530	0.1092
60^o	0.2011	0.0336	0.2864	0.1737
90^o	0.1824	0.0409	0.2386	0.1539
120^o	0.5309	0.1058	0.0937	0.2434
150^o	0.1084	0.0693	0.2855	0.1544
180^o	0.0407	0.1711	0.1309	0.1142
210^o	0.2274	0.1612	0.0842	0.1576
240^o	0.2703	0.0420	0.3155	0.2093
270^o	0.2634	0.0502	0.2552	0.1896
300^o	0.8258	0.1096	0.0385	0.3246
330^o	0.1469	0.1210	0.4417	0.2365

Table 5-7 Accuracy [%]

Angle	Accuracy (a)	Accuracy (b)	Accuracy (c)	Accuracy (average)
0	64.30	72.55	79.68	72.18
30^o	90.37	88.84	66.77	81.99
60^o	91.25	45.66	54.88	63.93
90^o	90.04	79.70	60.99	76.91
120^o	42.25	86.29	47.60	58.71
150^o	91.97	86.41	58.45	78.95
180^o	41.00	54.45	73.18	56.21
210^o	69.75	73.21	60.68	67.88
240^o	83.71	60.06	65.82	69.86
270^o	88.03	83.62	66.52	79.39
300^o	21.24	88.25	59.57	56.35
330^o	90.18	87.73	33.56	70.49

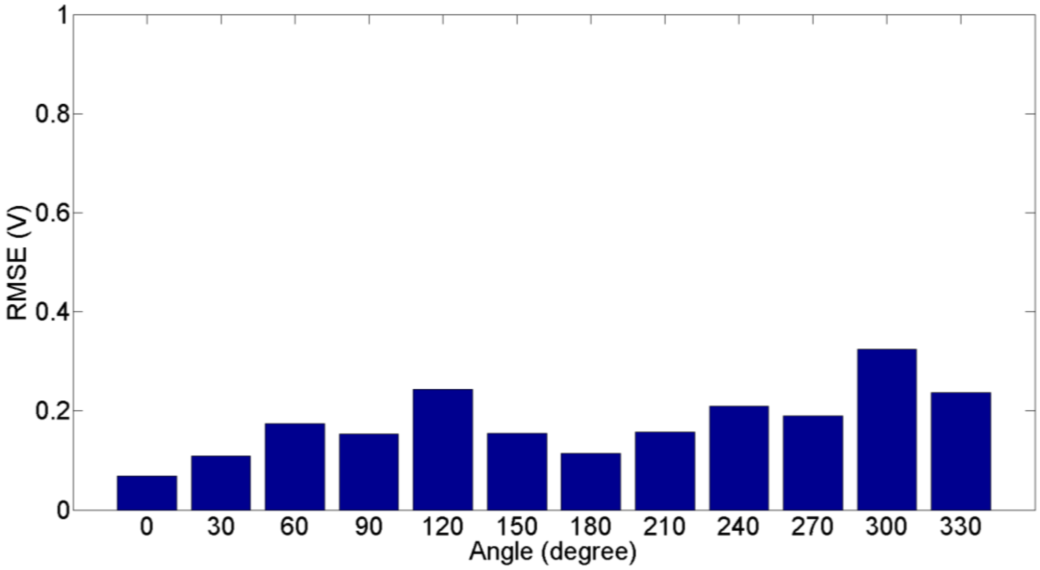

Figure 5-15 Average RMSE for different angles.

The root mean square error (RMSE) between experimental data and simulated data is shown in Table 5-6. The average RMSE of sensing element a, b and c are presented in Figure 5-15 and the average of all RMSE is 0.1780 V. The accuracy between experimental data and simulated data is shown in Table 5-7. The average of all RMSE is 69.4048%.

5.3.4. TEST RESULTS - FORCE AND ANGLE

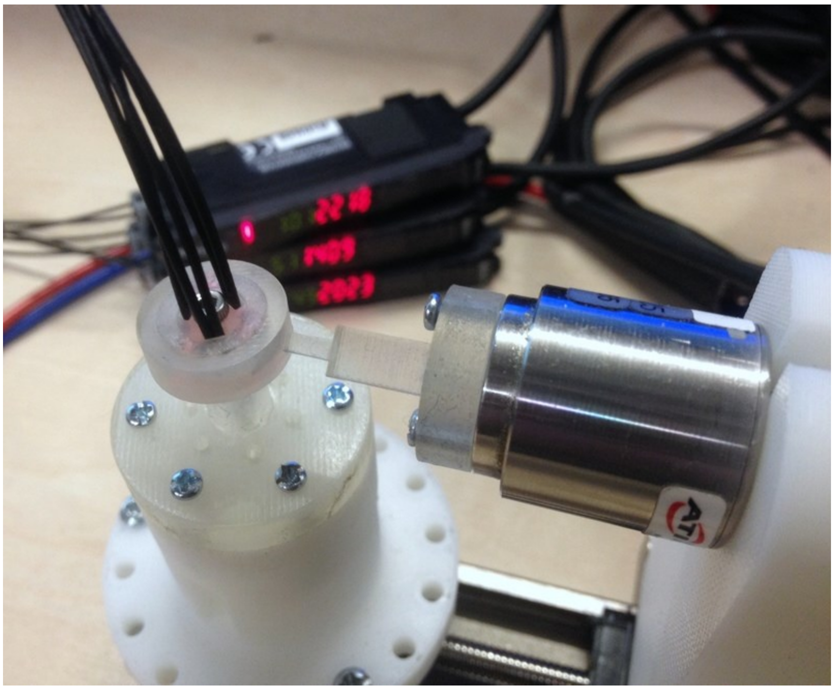

Figure 5-16 Test rig.

After calibration, the force and angle measurements of the proposed sensor are investigated using the same procedure as during calibration, shown in Figure 5-16. Tests were carried out on 12 points on the outer ring of proposed sensor, with a 30-degree gap between each point. The linear actuator drives the Nano 17 sensor into contact with the proposed sensor at a speed of 0.15mm/s at increments of 1.5 µm. The responses of the proposed sensor and the Nano 17 sensor are recorded on all 12 contact points. Figure 5-17 demonstrates the force measurements at $\alpha = 90^o$; 11 more results are shown in Figure 5-18. The root mean square error (RMSE) of force in this test is 0.0533 N (less than 10% of the total amplitude range), shown in Figure 5-19, and the standard deviation of the angle is 2.5652^{o} (with an angle error of 4.5769^{o}). Figure 5-20 shows the angle output from proposed sensor compared with input angle.

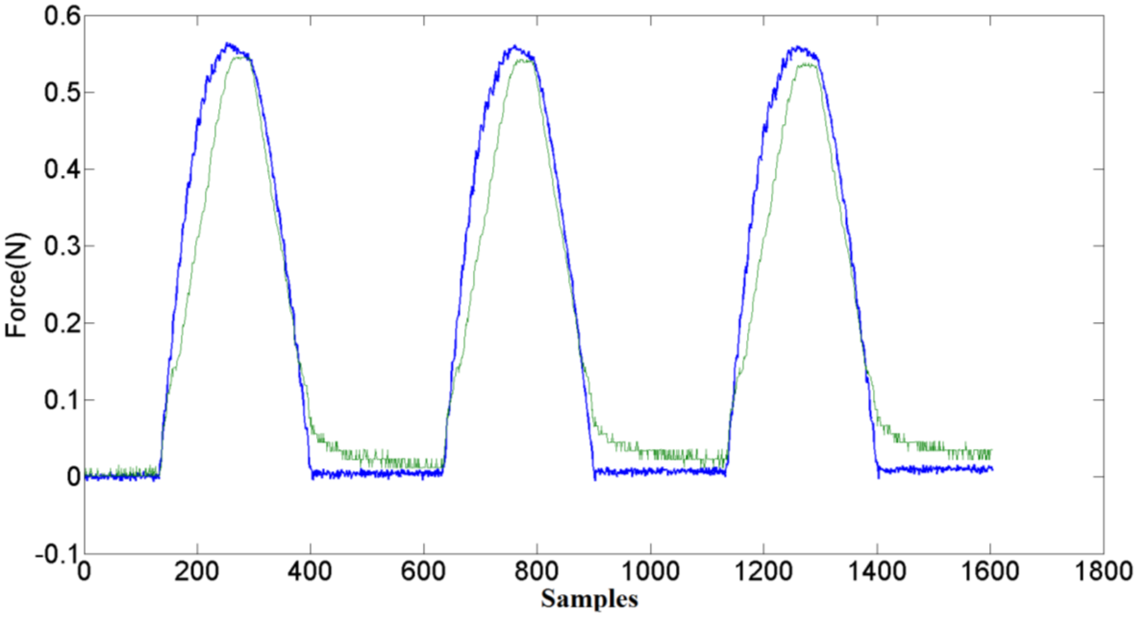

Figure 5-17 Force input measured by Nano 17 (blue) and force output measured by proposed sensor (green) at $\alpha = 90^{o}$.

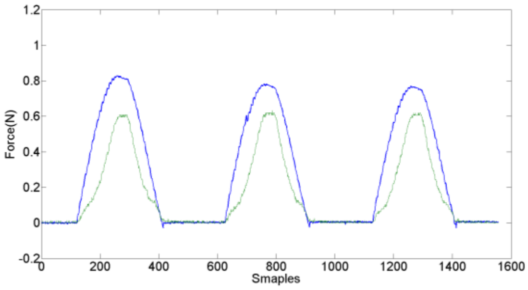

$\alpha = 0$

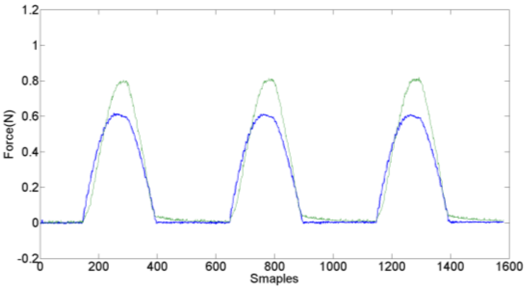

$\alpha = 30^o$

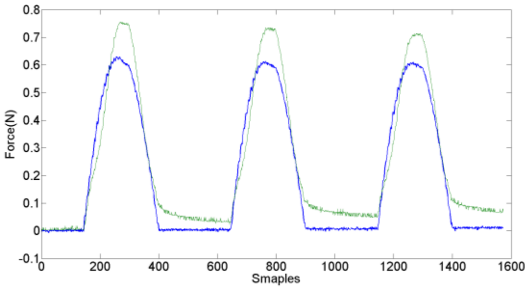

$\alpha = 60^o$

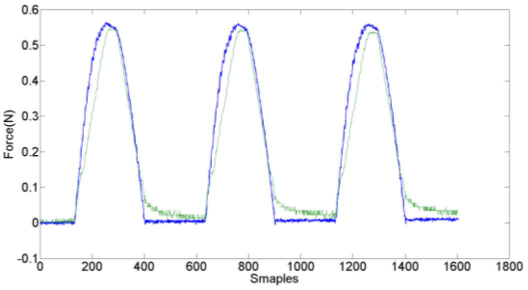

$\alpha = 90^o$

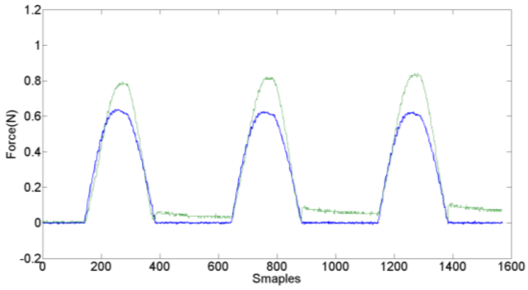

$\alpha = 120^o$

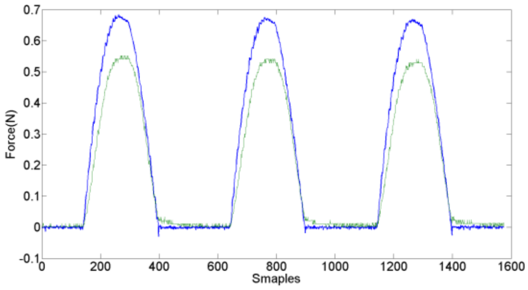

$\alpha = 150^o$

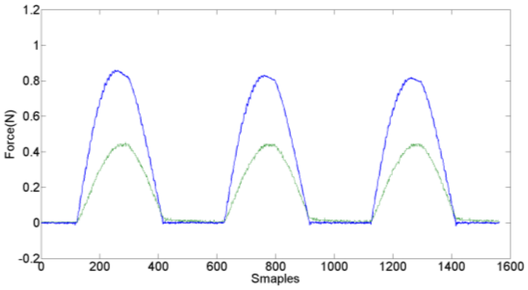

$\alpha = 180^o$

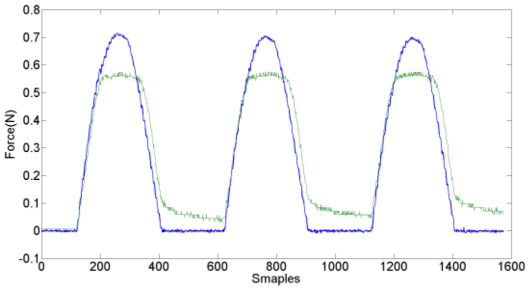

$\alpha = 210^o$

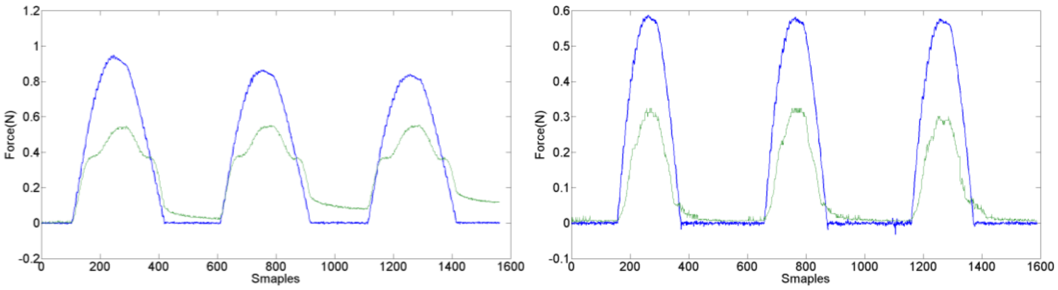

$\alpha = 240^o$ $\alpha = 270^o$

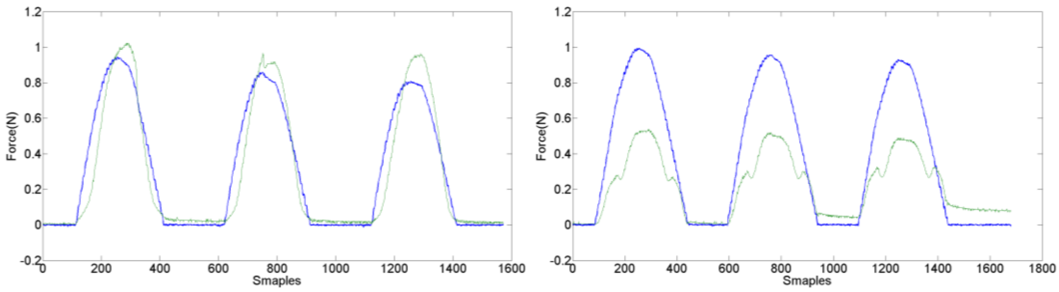

$\alpha = 300^o$ $\alpha = 330^o$

Figure 5-18 Force input measured by Nano 17 (blue) and force output measured by proposed sensor (green) at different locations.

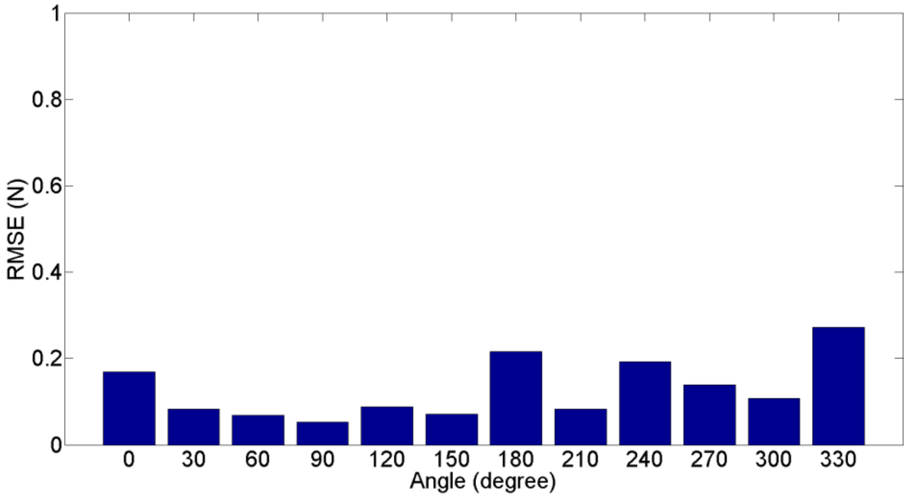

Figure 5-19 RMSE of force measurement at different angle locations.

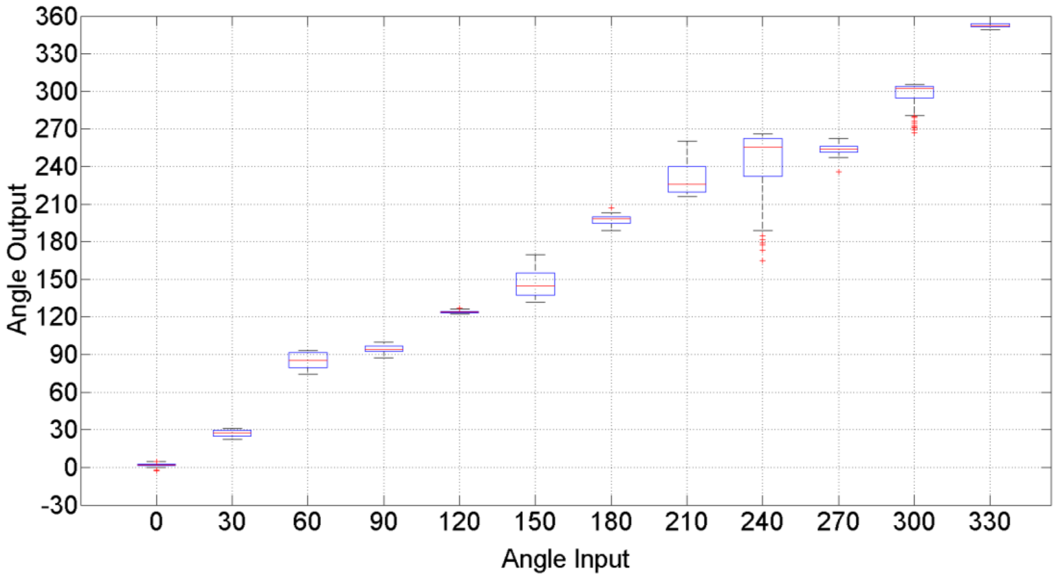

Figure 5-20 Experimental data of angle output.

Table 5-8 Force and Angle Accuracy and error

Angle	Force RMSE (N)	Force Accuracy (%)	Angle Output (º)	Angle Error (º)	Angle SD (º)
0	0.1694	79.5686	1.8756	1.8756	1.3507
30^o	0.0830	86.5691	27.3416	2.6584	2.5846
60^o	0.0691	89.0327	85.0790	25.0790	5.9230
90^o	0.0533	90.5541	94.5769	4.5769	2.5652
120^o	0.0884	86.1612	124.1403	4.1403	0.9328
150^o	0.0714	89.5652	146.4925	3.4925	10.0281
180^o	0.2159	74.9152	197.3262	17.3262	3.6130
210^o	0.0832	88.3707	230.5393	20.5393	12.6458
240^o	0.1927	79.7043	243.3032	3.3032	25.5472
270^o	0.1388	76.3589	254.2484	15.7516	3.5551
300^o	0.1082	88.5627	298.1597	1.8403	9.0543
330^o	0.2725	72.6195	352.1775	22.1775	1.4584

The RMSE and accuracy of force magnitude in 12 tested points are presented in Table 5-8 column 2&3, with the average RMSE value of 0.1288 N and average accuracy value of 83.4985 %. The error and SD of angle in 12 tested points are presented in Table 5-8 column 5&6, with the average error of 10.2301 degree and average SD value of 6.6048 degrees. At certain positions of the contact sensor, the standard deviation or accuracy is low compared to the overall performance (angle input at 240 degree for example). It is mostly due to the mechanical inconsistency of silicone caused by the manufacturing process, together with hysteresis effect of the silicone and light signal loss by fibre bending and connection [129]. The test results demonstrate that the proposed sensor is capable of providing accurate measurement of both force and contact point (angle).

5.4. CONCLUSIONS

In this section, a new two axis contact sensor that can detect force in x- and y-directions was presented. Because optical fibres are used, the sensor is able to work in MRI environments. A mathematical model is developed to illustrate the sensing principle of the proposed sensor. Sensor design and silicone manufacturing is presented. After evaluating the relationship between displacement/angle and force/voltage, the model of force calculation based on 3 voltage outputs is established. It is worth mentioning that a camera system previously described can be applied to the proposed sensor. Instead of voltage outputs, activated pixel numbers can be calculated via the camera system to obtain the applied force and angle information. During model validation tests, results from sensor outputs and simulation outputs are compared and analysed.

Test results have shown the proposed sensor has an accuracy of 83.4985% for force magnitude measurement and an average error of 10.2 degrees for contact location measurement. In addition, it can be integrated with the developed tactile probe head described in Chapter 4. The details can be found in appendix F.

Chapter 6 Conclusions & Future Work

This study investigated tactile sensing concepts based on optical fibres and developed sensor systems for MIS. The sensing concepts were verified mathematically and validated using developed sensor prototypes. This chapter provides the conclusion of the thesis and a discussion on future work.

6.1. CONCLUSIONS

The thesis presents research in tactile sensor design, fabrication and testing based on light intensity modulation using optical fibres. The aim of this study has been achieved by the creation of tactile sensors for minimally invasive surgeries, including tactile force detection in z-axis and contact force detection in x- and y-directions.

Basing the development of a tactile array sensor on light intensity modulation using optical fibres, the construction of a sensing system is able to achieve low cost, small in size, lightweight, free from electromagnetic interference, water and corrosion resistant and able to operate in harsh environments. A mathematical model has been developed to illustrate the translation from force information to light intensity information. A 3 × 3 tactile sensor prototype is developed in SolidWorks and manufactured using a 3D printer. Applied forces deform a micro-flexure inside each sensor tactel, displacing a miniature mirror which, in turn, modulates the light intensity introduced by a transmitting fibre connected to a light source at its proximal end. For each tactel, the light intensity is read by a receiving fibre connected directly to a 2D vision sensor. MATLAB is used both to control the camera and to process the images received by the vision sensor. The calibration process was conducted by relating the applied forces to the number of activated pixels for each image received from a receiving fibre. The proposed approach has allowed the concurrent acquisition of data from multiple tactile sensor elements using a vision sensor such as a standard video camera.

The miniaturized tactile probe head developed thereafter experienced the following improvements when compared to the first sensor prototypes (as described in Chapter 3): increased spatial resolution, and decreased tactile sensor size, hysteresis effect and crosstalk. The tactile probe head has a diameter of 14 mm using 14 sensing elements, 2.5 mm spaced apart. The replacement of the thick silicone material used previously with a thin latex rubber was found to reduce the hysteresis effect from which the earlier 3×3 tactel sensor prototype suffered. The design of separate grids in the microstructure isolated the deformation area of each individual sensing element and thus prevented crosstalk. It was found that the manufacturing process can be simplified by choosing an appropriate shape mirror with an acceptable linear response range. The sensitivity of this tactile probe head is 0.05 N with a sensing range from 0 to 0.5 N. Observer error may be caused by internal friction, the stiffness variation caused by the used rubber and the hysteresis effect. Experiments were performed for testing the probe's capability of detecting the tissue abnormality through spatial distribution of tactile force feedback. The results from ex-vivo experiments have shown that the proposed tactile probe head can accurately and effectively detect nodules embedded inside soft tissue, when probing the tissue in axial direction, demonstrating the promising application of this probe head for surgical palpation during MIS.

Advancing in the direction of creating a probe that can measure axial and lateral forces, a two-axis ring-shaped tactile sensor with a similar diameter as the probe head has been created. This sensor is capable of measuring the magnitude of lateral force and the contact location. A mathematical model based on a geometry-based algorithm is developed to illustrate the sensing principle of the proposed sensor. The sensor has three main parts: an outer ring, silicone as flexible material, and an inner cylinder. Three pairs of optical fibres are embedded in the inner cylinder to detect displacement change caused by applied force, utilizing light intensity modulation. After evaluating the relationship between displacement/angle and force/voltage, a model of determining the force and its direction based on the three voltage outputs is established. During model validation tests, results from sensor outputs and simulation outputs are compared and analysed. Test results have shown the proposed sensor has an accuracy of 83.5% for force magnitude measurements and an average error of 10.2 degree for contact location measurement.

In general, single-point force sensors have reached maturity while multiple, tactile array sensors are still in their infancy. However, there is high market demand for the latter, especially in the field of robotic surgery [4] [25]. For surgical use, tactile sensors need to be low cost because they are usually disposed off after single use – by utilizing optical fibres this requirement can be achieved. The 2D vision system allows the acquisition of signals from all sensing elements, together with providing a potential for high density tactile array sensing, employing a low-cost vision sensor. Combined with 3D printing technology, a miniature tactile probe head was designed - capable of palpation in MIS. Additional sense of touch on x- and y-directions is provided to the tactile probe head by a ring-shaped contact sensor. All sensor systems developed in this thesis are MRI compatible and immune to electromagnetic noise. The proposed sensing structures and principles indicate that the proposed sensors can be further miniaturized and achieve a high resolution, and thus are suitable to be integrated with medical tools.

6.2. FUTURE WORK

The tactile sensing methods proposed in the thesis have many potential applications, not only in robotics surgery, but also in humanoid robot manipulation, bomb diffusion in a confined space, disaster response and rescue operations. Future research can be focused on the following aspects:

- Further miniaturization: The proposed sensing structures and principles allow further miniaturization by using advanced 3D printing technology, thinner optical fibres and smaller reflective surface. The size can be significantly decreased if fibre couplers (effectively using one fibre per tactel only to transmit and receive light) are used, reducing the number of fibres to half of what it is currently. However, it is worth noticing that there is a trade-off between size and force sensing range and sensitivity due to the loss of light intensity during miniaturization, which is likely to be caused by sub-standard connections and misalignments of fibres.

- Rapidness of palpation: The developed tactile probe head has addressed the issue of time consuming investigation of large tissue areas. To further improve the rapidness of soft tissue abnormality identification, rollers can be developed to replace the cylinder shape contact feeler of each sensing element. Instead of a discrete process of indenting and lifting the probe head, a continuous and time saving process of rolling action can be carried out to construct a stiffness map of a large continuous tissue area.

- Integration of tactile array probe head and 2-axis tactile sensor: These two sensor systems are developed separately in this thesis. Future work can be focused on two aspects: the modification of the mechanical structure of both sensor systems, and the detection of light intensity information of all optical fibres using one camera.
- Sensitivity: Currently the force information is detected by analysing activated pixel numbers of the tactile array sensor. In future studies, a further analysis of the image information from the camera system, such as the individual pixel values (i.e., the light intensity of pixels), could improve the sensitivity of the proposed tactile array sensor.

APPENDIX

A.MATLAB/SIMULINK MODEL

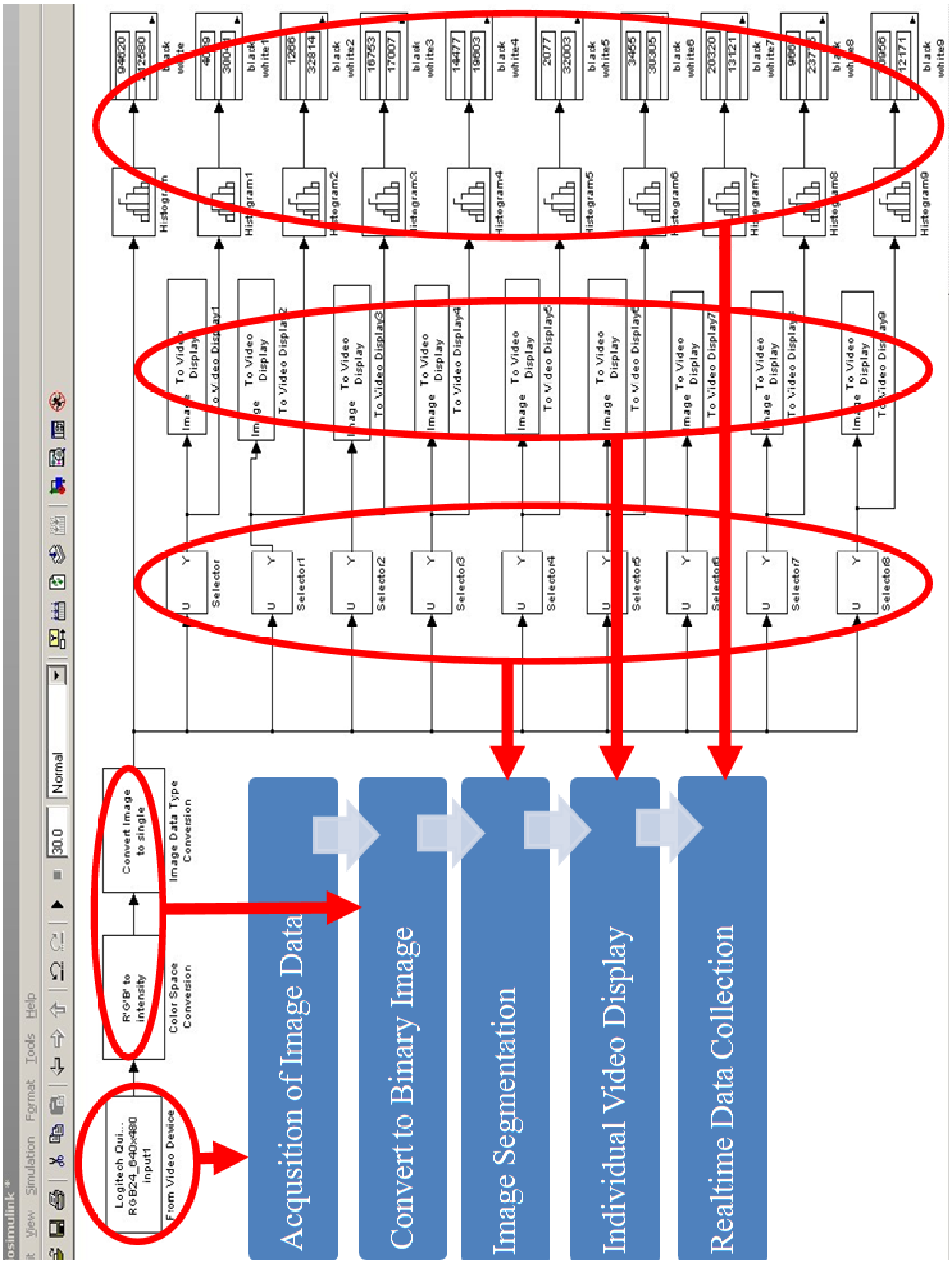

Figure A. 1 SimuLink model of light intensity detection.

B. LIGHT INTENSITY DISPLAY WITH DIFFERENT FORCE APPLIED

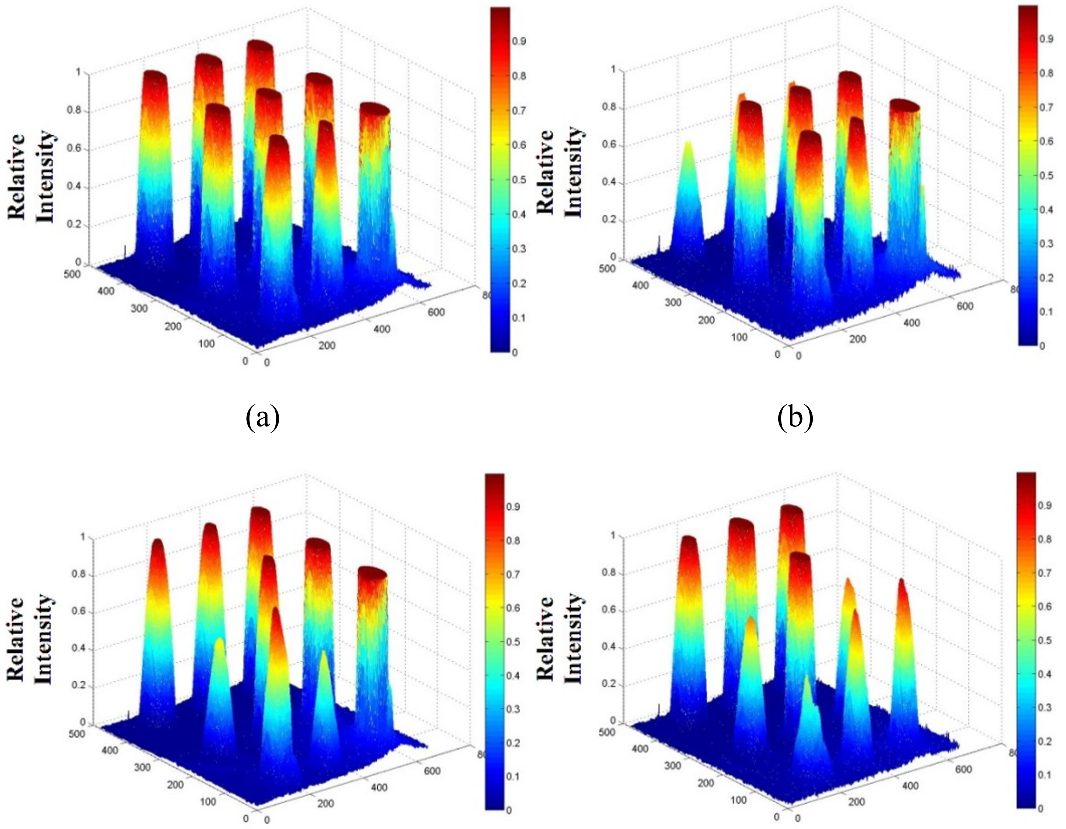

(a) (b)

(c) (d)

Figure B. 1 (a) Sensor Unloaded, (b) Force applied upper three elements, (c) Force applied lower left corner, (d) ‘U’ shape force applied lower part.

C. INDIVIDUAL CALIBRATION CURVE OF ALL SENSING ELEMENTS

1)

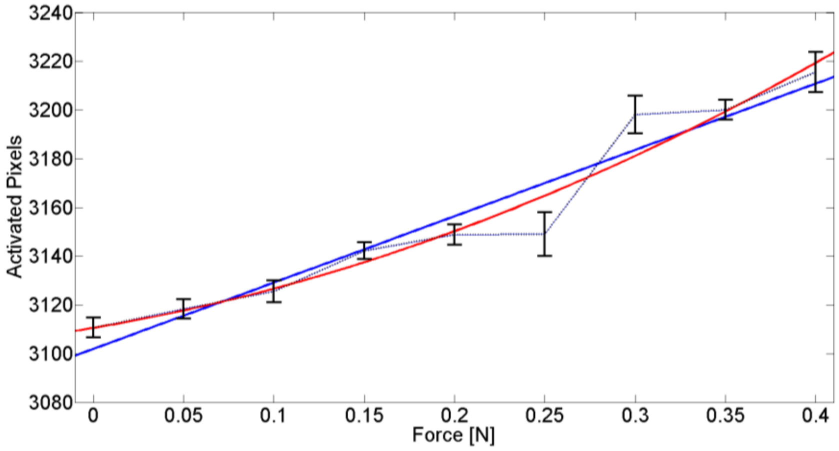

2)

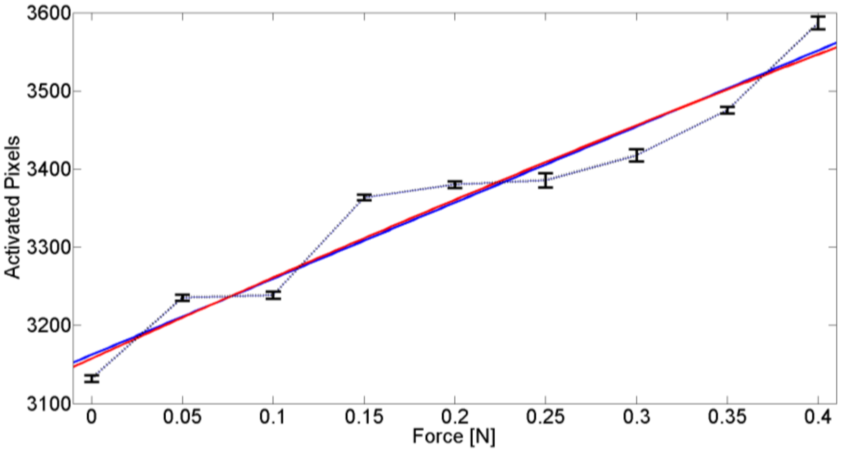

3)

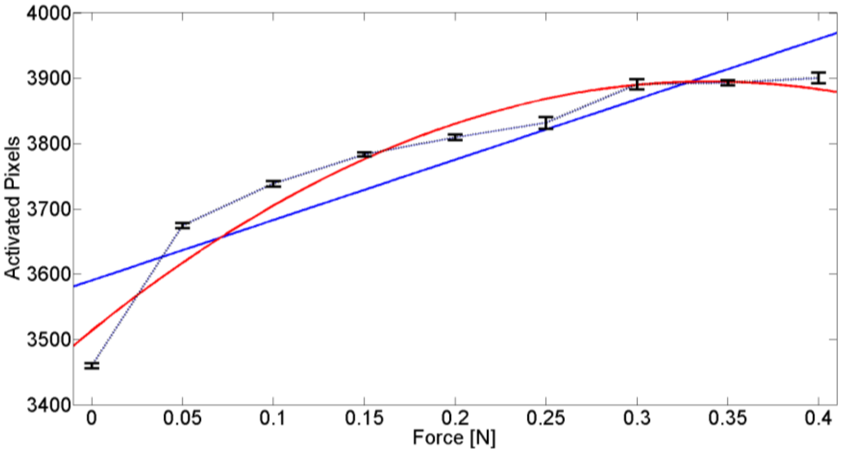

4)

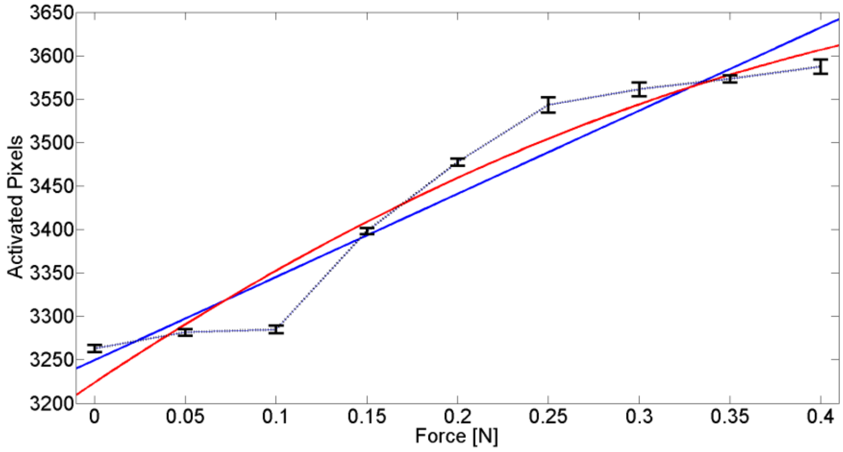
3650
3600
3550
3500
3450
3400
3350
3300
3250
3200
Activated Pixels
0
0.05
0.1
0.15
0.2
0.25
0.3
0.35
0.4
Force [N]

5)

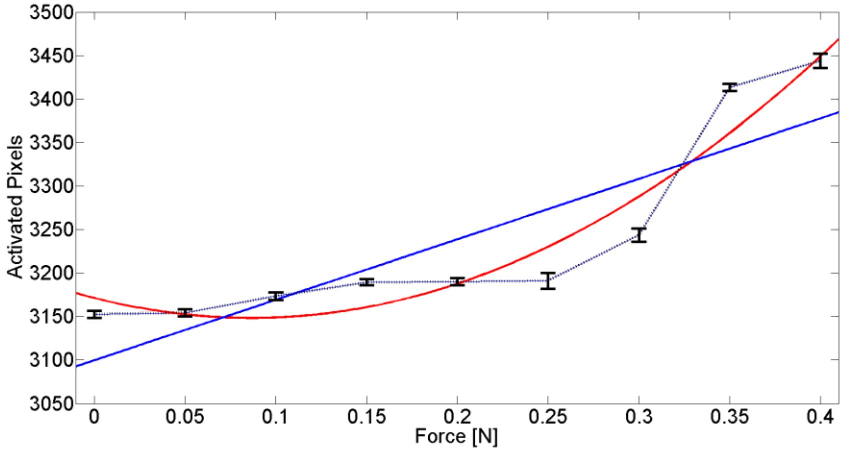
3500
3450
3400
3350
3300
3250
3200
3150
3100
3050
Activated Pixels
0
0.05
0.1
0.15
0.2
0.25
0.3
0.35
0.4
Force [N]

6)

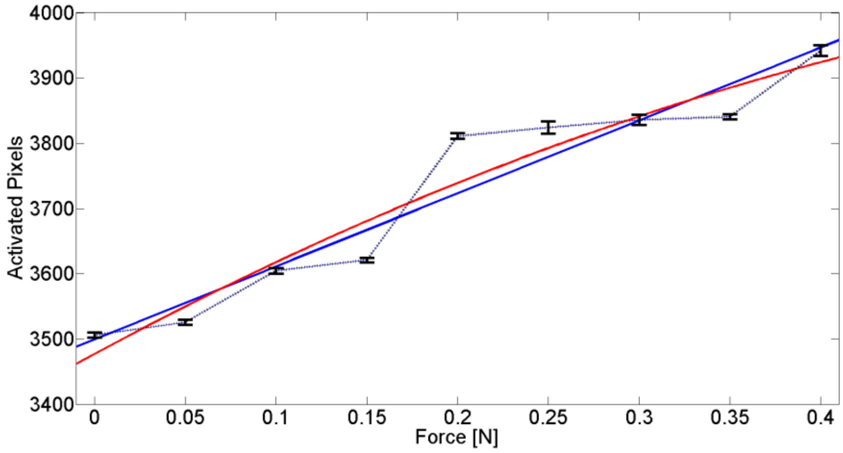
4000
3900
3800
3700
3600
3500
3400
Activated Pixels
0
0.05
0.1
0.15
0.2
0.25
0.3
0.35
0.4
Force [N]

7)

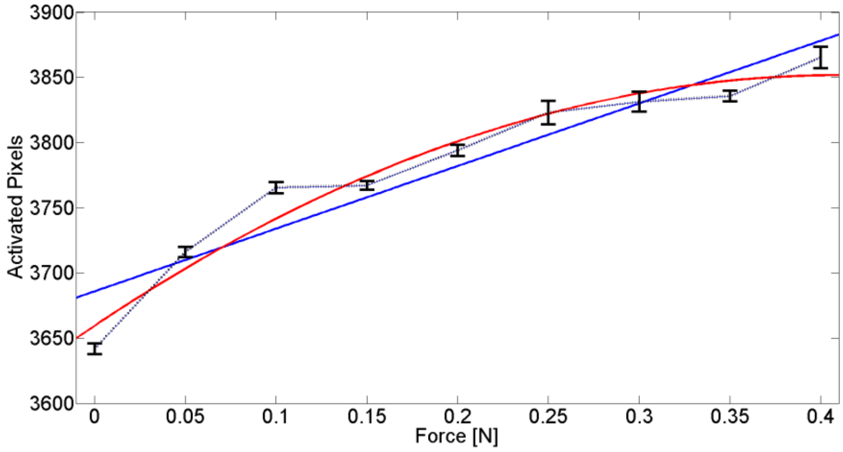
3900
3850
3800
3750
3700
3650
3600
Activated Pixels
0
0.05
0.1
0.15
0.2
0.25
0.3
0.35
0.4
Force [N]

8)

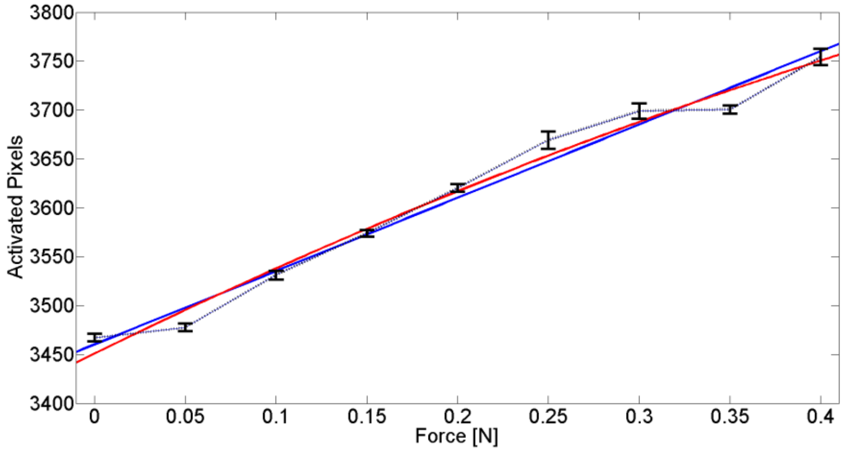
3800
3750
3700
3650
3600
3550
3500
3450
3400
Activated Pixels
0
0.05
0.1
0.15
0.2
0.25
0.3
0.35
0.4
Force [N]

9)

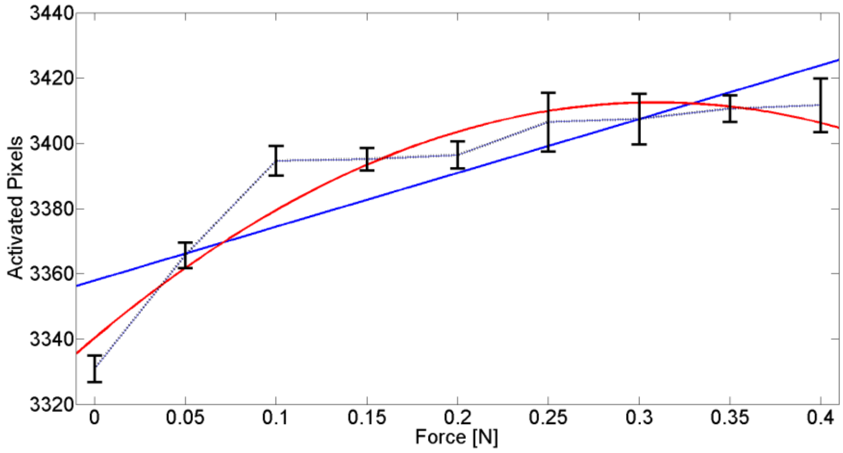
3440
3420
3400
3380
3360
3340
3320
Activated Pixels
0
0.05
0.1
0.15
0.2
0.25
0.3
0.35
0.4
Force [N]

10)

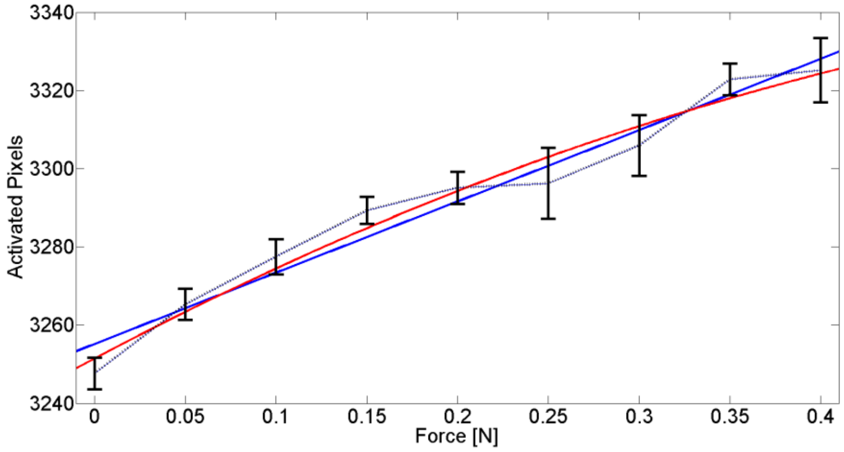
3340
3320
3300
3280
3260
3240
Activated Pixels
0
0.05
0.1
0.15
0.2
0.25
0.3
0.35
0.4
Force [N]

11)

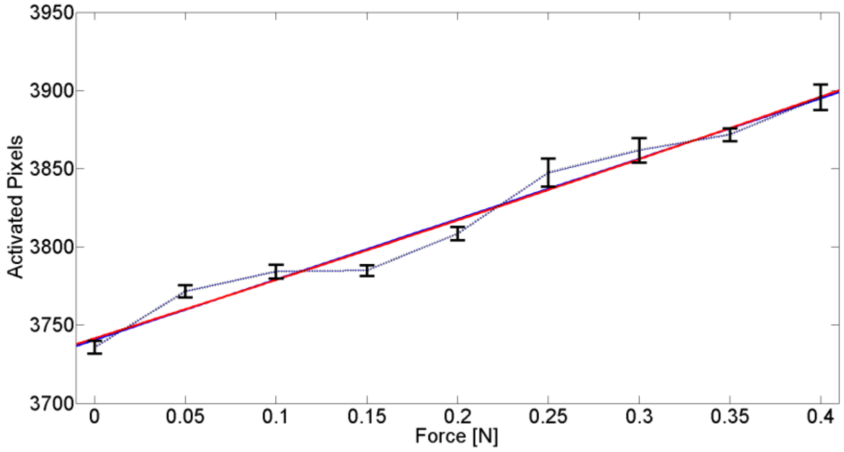
3950
3900
3850
3800
3750
3700
Activated Pixels
0
0.05
0.1
0.15
0.2
0.25
0.3
0.35
0.4
Force [N]

12)

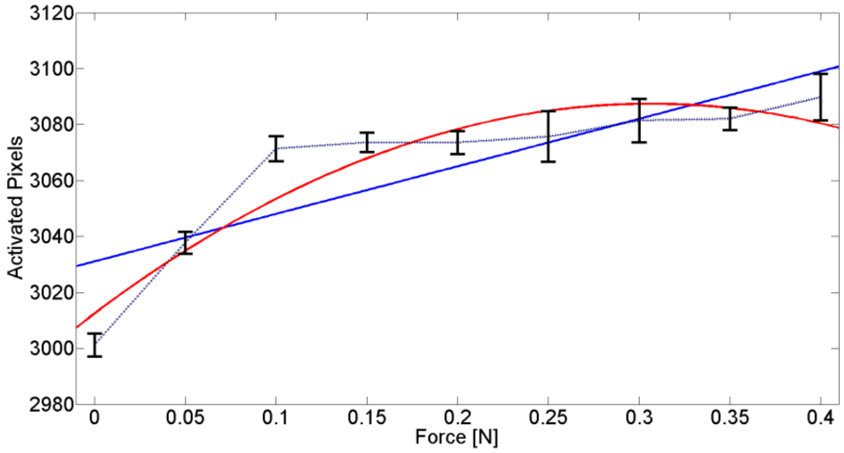
3120
3100
3080
3060
3040
3020
3000
2980
Activated Pixels
0
0.05
0.1
0.15
0.2
0.25
0.3
0.35
0.4
Force [N]

13)

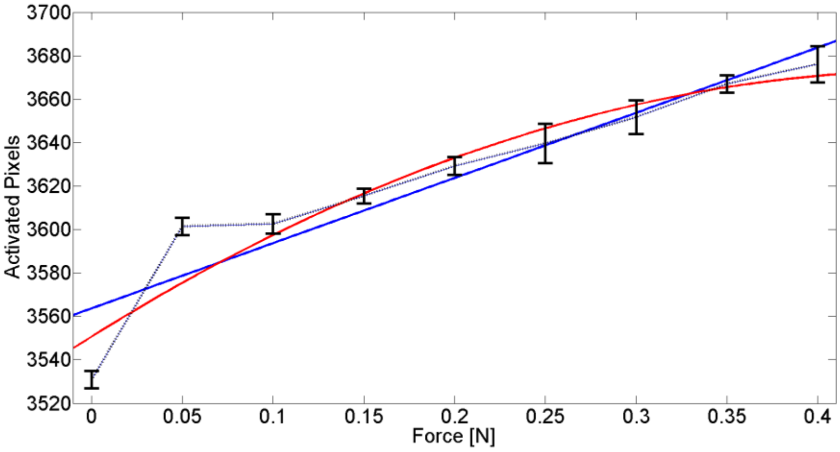

14)

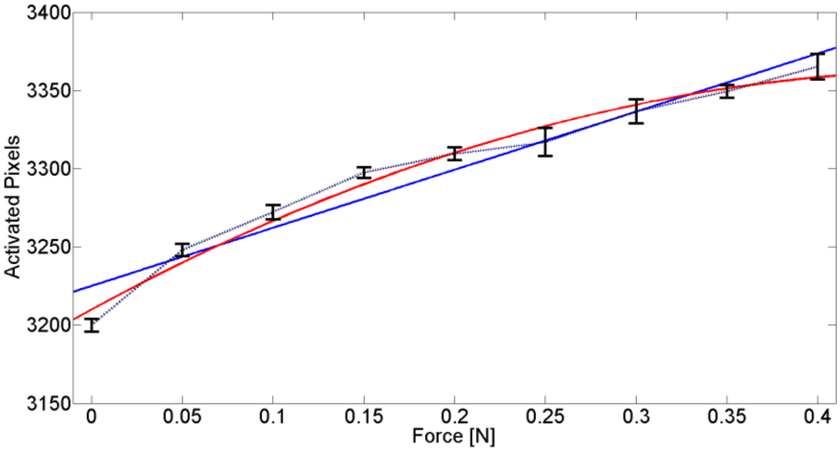

Figure C. 1 Calibration curves of all sensing elements.

D. NOISE ANALYSIS

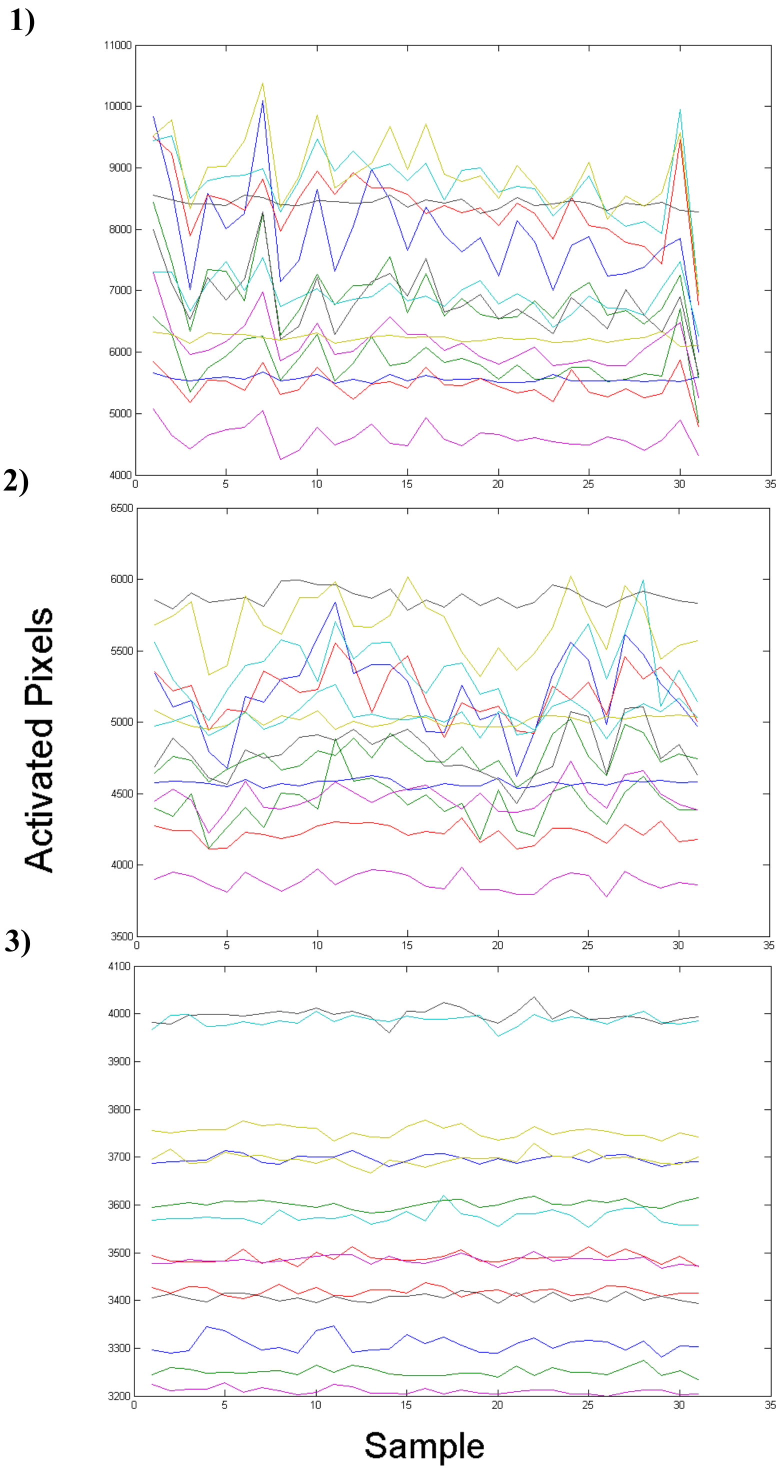

Figure D. 1 Noise analysis of different light source intensity (high-medium-low/1-2-3) at brightness=200.

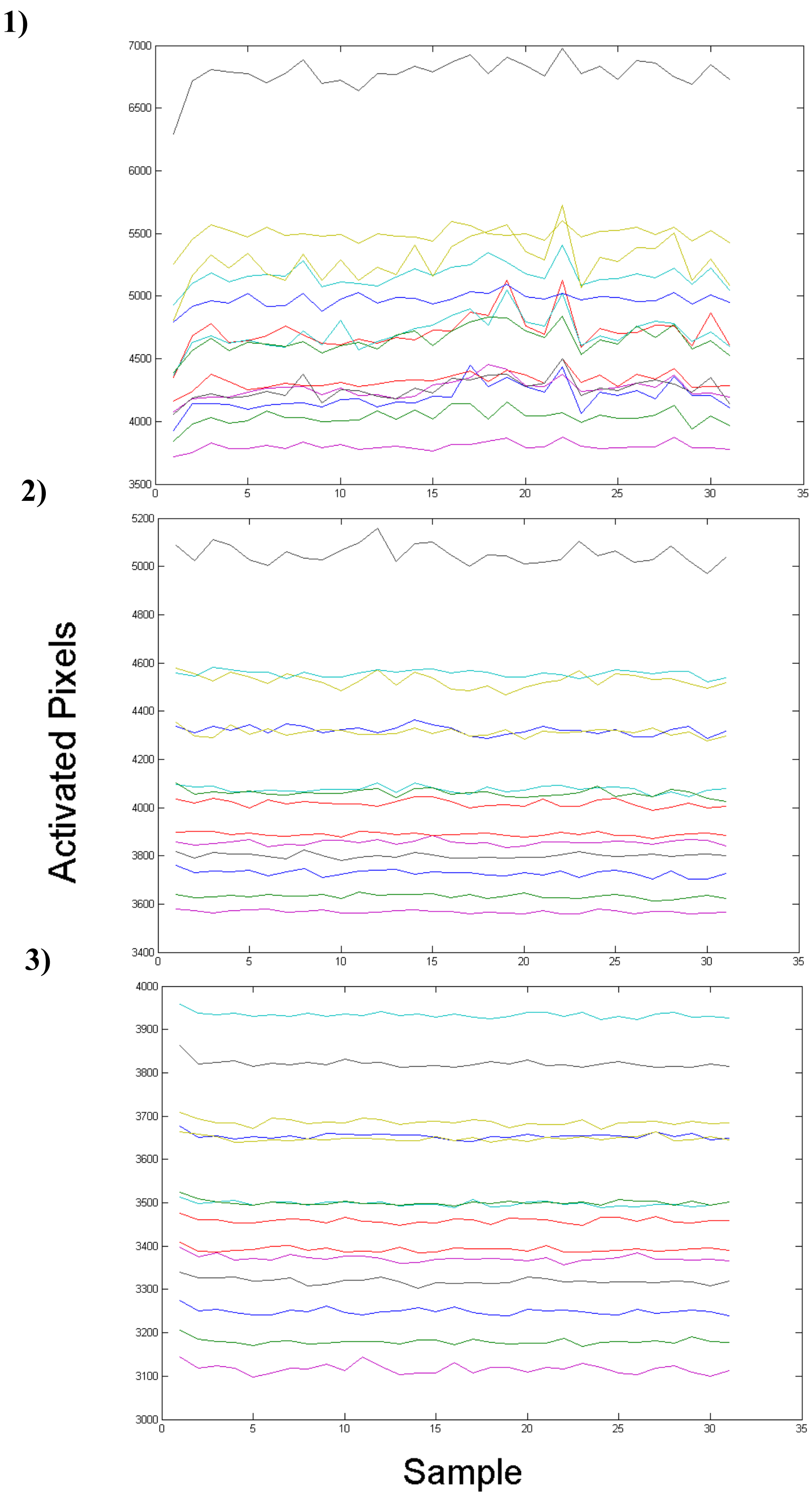

Figure D. 2 Noise analysis of different light source intensity (high-medium-low/1-2-3) at brightness=140.

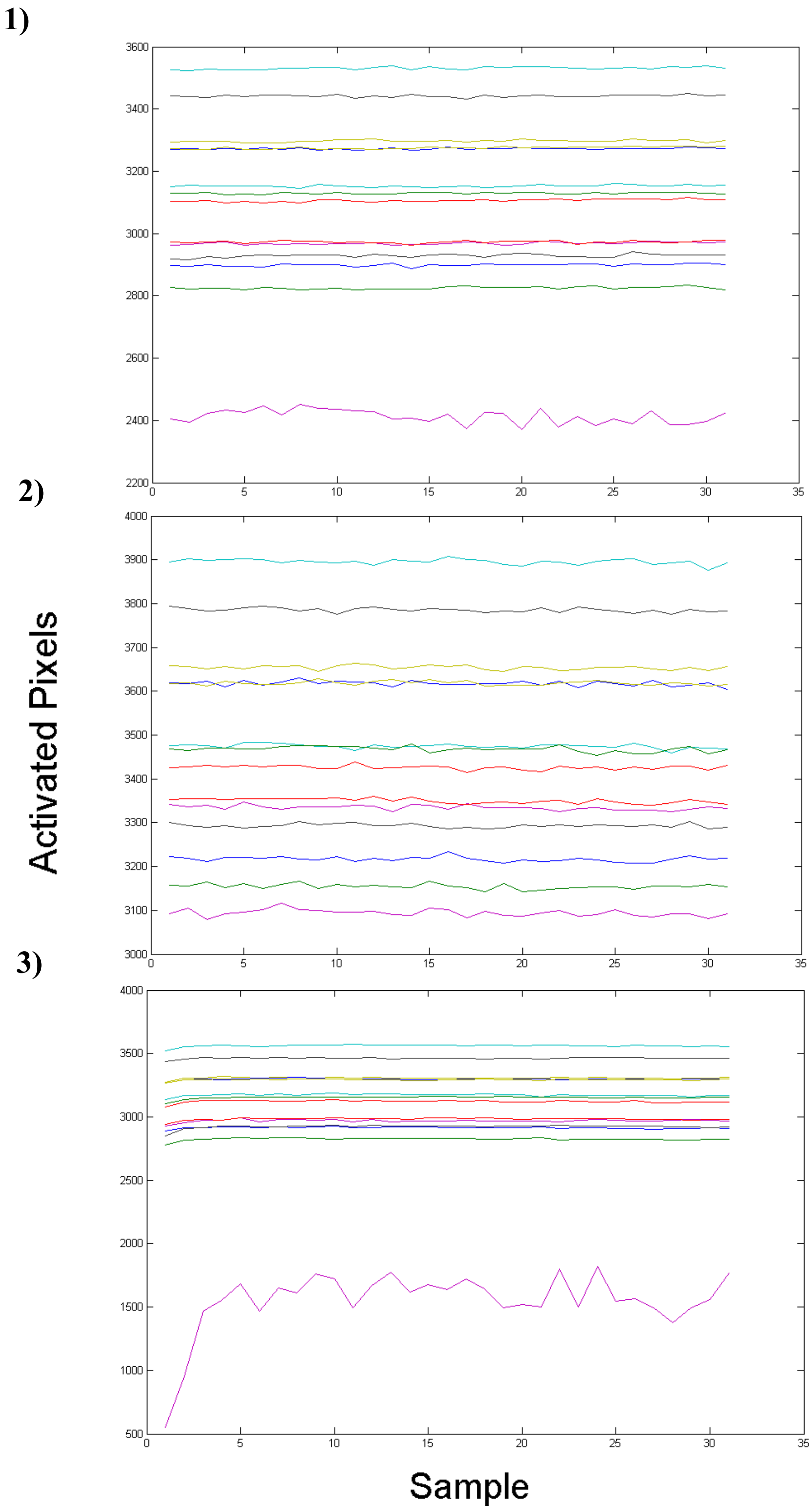

Figure D. 3 Noise analysis of different light source intensity (high-medium-low/1-2-3) at brightness=80.

E. PSEUDO MATLAB CODE:

E.1 CODE FOR PALPATION

```
for i=1:14
a(i)=ScopeData1.signals.values(2,1,:);
%% comment: read the activated pixel number data of all 14 sensing elements from image data collected in MATLAB

S=10;T=20; ……. Q=270;R=280;
%% comment: define time nodes when palpation is conducted

c(i)=[mean(a(i)(A:B)) …… mean(a(i)(Q:R)) ];
d(i)=[std2(a(i)(A:B)) …… mean(a(i)(Q:R)) ];
%% comment: obtain the average force magnitude and standard deviation during each palpation procedure of all 14 sensing elements

cc(i)(1:9)=mean(a(i)(S:T));
ccc(i)=c(i)-cc(i);
ccc(i)=ccc(i)/K(i);
%% comment: calibration process of all sensing elements by first deducting the value unloaded, then linear fitting equation is utilized to calibrate the pixel information to force information

subplot(4,4,i); plot(ccci)
%% comment: plot outputs of all sensing elements
```

E.2 CODE FOR FORCE/ANGLE SIMULATION

```
kf=1;
k1=3.4;
k2=58/62;
k3=1/3;
%% comment: define system parameters based on previous experiment data

for i=1:12
%% comment: same data processing is conducted at all other locations

f(i)=c(i)(:,5);
apha(i)=pi/2;
a(i)=-f(i)/kf*k1*sin(apha(i));
b(i)=-f(i)/kf*k2*sin(3.1415926/3-apha(i));
```

```
d(i)=-f(i)/kf*k3*sin(apha(i)-3.1415926/1.5);
%% comment: simulated voltage outputs of three sensing elements based on the
same force input

RMSE(i)a=sqrt(sum((a(i)-c(i) (:,2)).^2)/1603);
RMSE(i)b=sqrt(sum((b(i)-c(i) (:,4)).^2)/1603);
RMSE(i)c=sqrt(sum((d(i)-c(i) (:,3)).^2)/1603);
%% comment: RMSE value between simulated voltage outputs and voltage outputs
during the experiments

accuracy(i)a=100-sqrt(sum((a(i)-c(i) (:,2)).^2)/1603)/max(abs(c(i) (:,2)))*100;
accuracy(i)b=100-sqrt(sum((b(i)-c(i) (:,4)).^2)/1603)/max(abs(c(i) (:,4)))*100;
accuracy(i)c=100-sqrt(sum((d(i)-c(i) (:,3)).^2)/1603)/max(abs(c(i) (:,3)))*100;
%% comment: accuracy data between simulated voltage outputs and voltage outputs
during the experiments

x(i)=mean([RMSE(i)a,RMSE(i)b,RMSE(i)c]);
xaccuracy(i)=mean([accuracy(i)a,accuracy(i)b,accuracy(i)c]);
%% comment: average RMSE value and average accuracy of three sensing elements
at one location

xx=mean([x(i)]);
xxaccuracy=mean([xaccuracy(i));
%% comment: average RMSE value and average accuracy of three sensing elements
at all location
```

E.3 CODE FOR FORCE/ANGLE OUTPUTS:

```
kf=1;
k1=3.4;
k2=58/62;
k3=1/3;
%% comment: define system parameters based on previous experiment data

for i=1:12
%% comment: same data processing is conducted at all other locations
v1=c(i)(:,2);
v2=c(i) (:,4);
v3=c(i) (:,3);
%% comment: obtain voltage data from the experiment
f1=2*sqrt(abs((k2.*v1+k1.*v2).*(k2.*v1+k1.*v2)-k1*k2.*v1.*v2))/(sqrt(3)*k1*k2);
f2=2*sqrt(abs((k2.*v3-k3.*v2).*(k2.*v3-k3.*v2)+k2*k3.*v2.*v3))/(sqrt(3)*k2*k3);
f3=2*sqrt(abs((k1.*v3+k3.*v1).*(k1.*v3+k3.*v1)-k1*k3.*v1.*v3))/(sqrt(3)*k1*k3);
```

```
%% comment: force magnitude calculation based on the Equation 5-27

f=(f1+f2+f3)/3;
%% comment: average force magnitude using all three outputs of sensing elements

RMSE=sqrt(sum((f+c(i) (:,5)).^2)/1580);
accuracy=100-sqrt(sum((f+c(i) (:,5)).^2)/1580)/max(abs(c(i) (:,5)))*100;
%% comment: RMSE and accuracy data between calculated force magnitude based
on sensor outputs and applied force during the experiments

plot(-c(i) (:,5),'LineWidth',2);
xlabel('Smaples','fontsize',30)
ylabel('Force(N)','fontsize',30)
set(gca,'fontsize',30)
hold all
%% comment: plot applied force information

plot(f,'DisplayName','experimental results','YDataSource','f');figure(gcf)
%% comment: plot simulated force magnitude outputs

apha1=180*atan((sqrt(3)*k2.*v1)./(k2.*v1+2*k1.*v2));
apha2=180*atan((sqrt(3)*(k2.*v3-k3.*v2))./(k2.*v3+k3.*v2));
apha3=180*atan((sqrt(3)*k3.*v1)./(k3.*v1+2*k1.*v3));
%% comment: angle calculation based on the Equation 5-26

apha=(apha1+apha2+apha3)/3;
%% comment: average angle output using all three outputs of sensing elements

avapha=mean(apha);
stdapha=std(apha);
%% comment: accuracy and standard deviation between calculated angle based on
sensor outputs and input angle during the experiments and the results are presented
in Section 5.3.4.
```

F. FUTURE INTEGRATION

Both tactile probe head and lateral contact sensor are designed with similar diameter in order to conduct surgeries in MIS, shown in Figure F. 1. However, there are still some mechanical issues exist for the integration, which are bonding problem between these two sensors, extra space needed for fibres going through and uniformity of size (fibres, etc.).

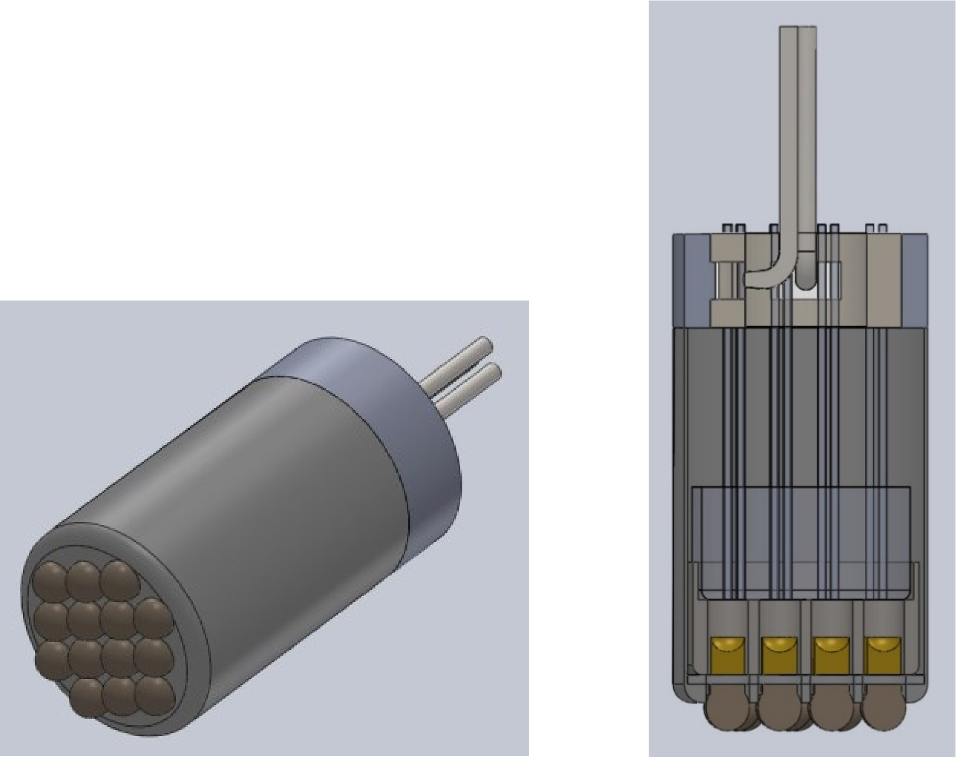

(a) (b)

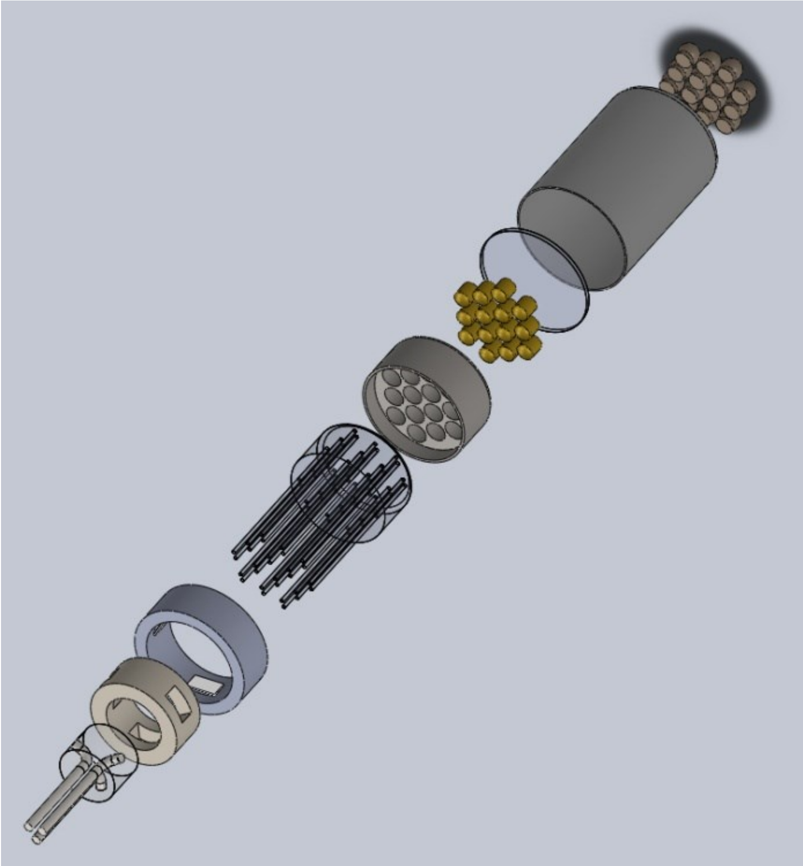

(c)

Figure F. 1 Future work on the integration of two axis tactile sensor with tactile probe head: (a) CAD drawing, (b) side view, (c) assembling view.

On the software side of light intensity detection method, the future schematic design is shown in Figure F. 2. After modifying the mechanical design, all optical fibres from both tactile sensors can be placed in a way that a camera can detect all light intensity in one go. By separating and analysing the light intensity information of the contact sensor and the array sensor, both lateral and vertical contact forces can be calculated and displayed.

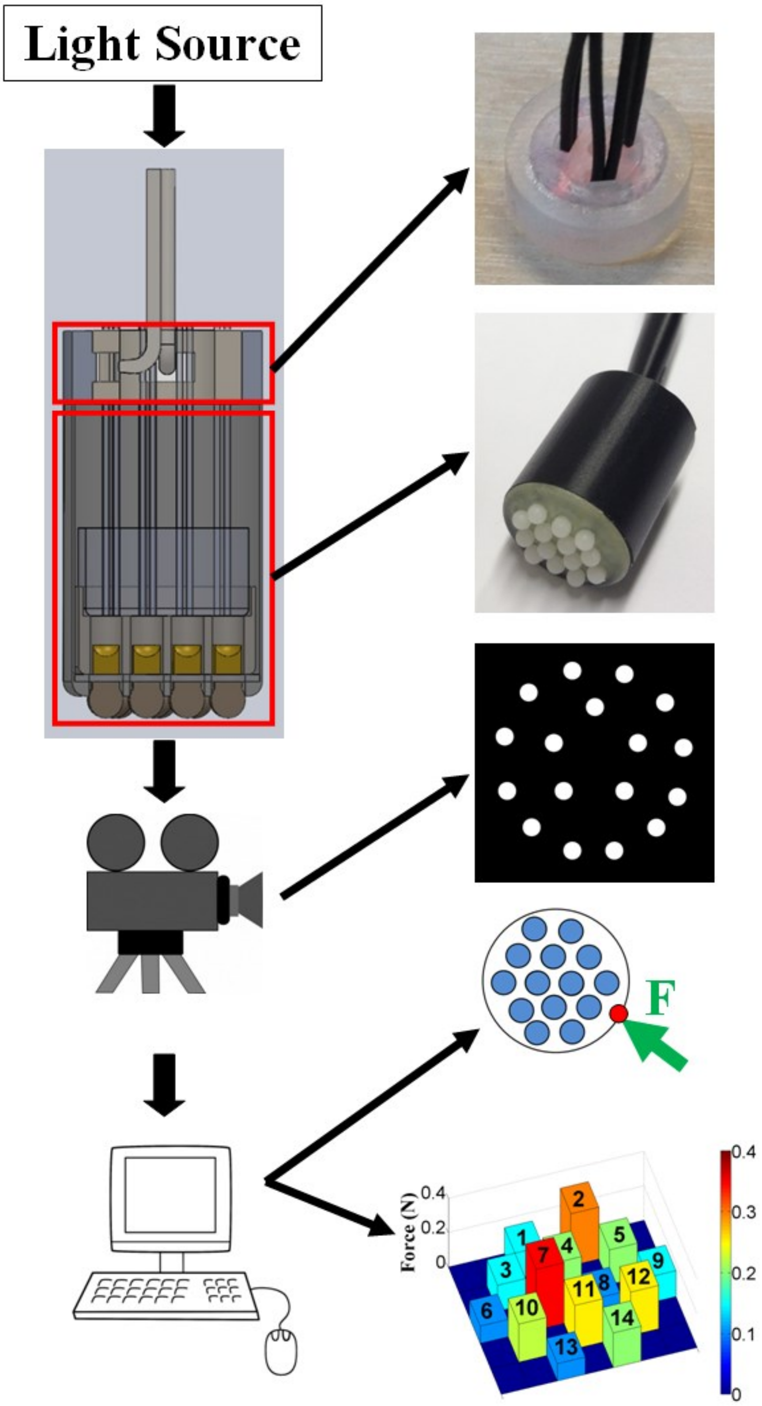

Figure F. 2 Schematic design of the integration of two axis tactile sensor with tactile probe head.

G. PUBLICATION

Journal Papers

[1] Hui Xie, N. Yohan, H. Liu, K. Althoefer, "A Fiber-Optics based Contact Sensor for Flexible Manipulator during MIS", *IEEE Sensors Journal, 2014***.** (Under preparation.)

[2] Hui Xie, H. Liu, L. D. Seneviratne, K. Althoefer, "An Optical Tactile Array Probe Head for Tissue Palpation during Minimally Invasive Surgery", *IEEE Sensors Journal,* vol. 14, no. 9, pp. 3283-3291, 2014

[3] Hui Xie, A. Jiang, H. Wurdemann, H. Liu, L. Seneviratne, K. Althoefer, "Magnetic Resonance-Compatible Tactile Force Sensor using Fiber Optics and Vision Sensor", *IEEE Sensors Journal,* vol. 14, no. 3, pp. 829-838, 2014.

Peer-reviewed International Conference Papers

[1] Hui Xie, H. Liu, K. Althoefer, "A Tactile Palpation Probe using Optical Fibers and Camera System", IEEE International Conference on Advanced Robotics and Intelligent Systems (ARIS), Taipei, 2014. (Accepted)

[2] Hui Xie, H. Liu, S. Luo, L. D. Seneviratne, K. Althoefer, "Fiber Optics Tactile Array Probe for Tissue Palpation during Minimally Invasive Surgery", *IEEE/RSJ International Conference on Intelligent Robots and Systems (IROS)*, Tokyo, pp. 2539-2544, 2013**.**

[3] Hui Xie, A. Jiang, L. D. Seneviratne, K. Althoefer, "Pixel-based Optical Fiber Tactile Force Sensor for Robot Manipulation", *Sensors, IEEE International Conference*, Taipei, pp. 1-4, 2012.

References

[1] J. Krüger, T. K. Lien, and A. Verl, "Cooperation of human and machines in assembly lines," *CIRP Ann. - Manuf. Technol.*, vol. 58, pp. 628–646, 2009.

[2] R. J. Stein, W. M. White, R. K. Goel, B. H. Irwin, G. P. Haber, and J. H. Kaouk, "Robotic Laparoendoscopic Single-Site Surgery Using GelPort as the Access Platform," *Eur. Urol.*, vol. 57, pp. 132–137, 2010.

[3] C. C. Kemp, A. Edsinger, and E. Torres-Jara, "Challenges for robot manipulation in human environments," *IEEE Robot. Autom. Mag.*, vol. 14, p. 20, 2007.

[4] M. I. Tiwana, S. J. Redmond, and N. H. Lovell, "A review of tactile sensing technologies with applications in biomedical engineering," *Sensors Actuators A Phys.*, vol. 179, pp. 17–31, Jun. 2012.

[5] Y. R. Wang, J. M. Zheng, G. Y. Ren, P. H. Zhang, and C. Xu, "A flexible piezoelectric force sensor based on PVDF fabrics," *Smart Materials and Structures*, vol. 20. p. 045009, 2011.

[6] T. Yamada, Y. Hayamizu, Y. Yamamoto, Y. Yomogida, A. Izadi-Najafabadi, D. N. Futaba, and K. Hata, "A stretchable carbon nanotube strain sensor for human-motion detection.," *Nat. Nanotechnol.*, vol. 6, pp. 296–301, 2011.

[7] A. S. G. Reddy, B. B. Narakathu, M. Z. Atashbar, M. Rebros, E. Rebrosova, B. J. Bazuin, M. K. Joyce, P. D. Fleming, and A. Pekarovicova, “Printed Capacitive Based Humidity Sensors on Flexible Substrates,” *Sens. Lett.*, vol. 9, pp. 869–871, 2011.

[8] H. Su and G. S. Fischer, “A 3-axis optical force/torque sensor for prostate needle placement in Magnetic resonance imaging environments,” *2009 IEEE Int. Conf. Technol. Pract. Robot Appl.*, 2009.

[9] Y. Fu, H. Di, and R. Liu, “Light intensity modulation fiber-optic sensor for curvature measurement,” *Opt. Laser Technol.*, vol. 42, pp. 594–599, 2010.

[10] M. H. Korayem, N. Shiehbeiki, and T. Khanali, “Design, manufacturing, and experimental tests of a prismatic robot for assembly line,” *The International Journal of Advanced Manufacturing Technology*, vol. 29, no. 3–4. pp. 379–388, 2006.

[11] B. Davies, “A review of robotics in surgery.,” *Proc. Inst. Mech. Eng. H.*, vol. 214, no. 1, pp. 129–140, 2000.

[12] G. Dogangil, B. L. Davies, and F. Rodriguez y Baena, “A review of medical robotics for minimally invasive soft tissue surgery,” *Proc. Inst. Mech. Eng. Part H J. Eng. Med.*, vol. 224, no. 5, pp. 653–679, May 2010.

[13] A. L. Trejos, J. Jayender, M. T. Perri, M. D. Naish, R. V. Patel, and R. A. Malthaner, “Robot-assisted Tactile Sensing for Minimally Invasive Tumor Localization,” *Int. J. Rob. Res.*, vol. 28, no. 9, pp. 1118–1133, May 2009.

[14] P. Puangmali, K. Althoefer, L. D. Seneviratne, D. Murphy, and P. Dasgupta, “State-of-the-Art in Force and Tactile Sensing for Minimally Invasive Surgery,” *IEEE Sens. J.*, vol. 8, no. 4, pp. 371–381, Apr. 2008.

[15] T. Haidegger, J. Sándor, and Z. Benyó, “Surgery in space: the future of robotic telesurgery.,” *Surg. Endosc.*, vol. 25, pp. 681–690, 2011.

[16] G. Gao, S. Tarte, A. King, Y. Ma, P. Chinchapatnam, T. Schaeffter, R. Razavi, D. Hawkes, D. Hill, and K. Rhode, “Validation of the use of photogrammetry to register pre-procedure MR images to intra-procedure patient position for image-guided cardiac catheterization procedures,” in *Medical Imaging*, 2008, p. 69181Q–69181Q.

[17] J. F. Schenck, “The role of magnetic susceptibility in magnetic resonance imaging: MRI magnetic compatibility of the first and second kinds.,” *Med. Phys.*, vol. 23, pp. 815–850, 1996.

[18] P. Polygerinos, D. Zbyszewski, T. Schaeffter, R. Razavi, L. D. Seneviratne, and K. Althoefer, “MRI-Compatible Fiber-Optic Force Sensors for Catheterization Procedures,” *Sensors Journal, IEEE*, vol. 10, pp. 1598–1608, 2010.

[19] M. Li, M. B. Ridzuan, S. Sareh, L. D. Seneviratne, P. Dasgupta, and K. Althoefer, "Pseudo-haptics for rigid tool/soft surface interaction feedback in virtual environments," *Mechatronics*, vol. 24, no. 8, pp. 1092–1100, Dec. 2014.

[20] S. Aoyagi, T. Tanaka, and M. Minami, "Recognition of Contact State of Four Layers Arrayed Type Tactile Sensor by using Neural Network," *2006 IEEE Int. Conf. Inf. Acquis.*, pp. 393–387, 2006.

[21] J. Cecil, D. Powell, and D. Vasquez, "Assembly and manipulation of micro devices-A state of the art survey," *Robot. Comput. Integr. Manuf.*, vol. 23, pp. 580–588, 2007.

[22] T. Papakostas, J. Lima, and M. Lowe, "A large area force sensor for smart skin applications," *Sensors, 2002. Proc. IEEE*, vol. 2, pp. 1620–1624, 2002.

[23] A. Schmitz, P. Maiolino, M. Maggiali, L. Natale, G. Cannata, and G. Metta, "Methods and Technologies for the Implementation of Large-Scale Robot Tactile Sensors," *IEEE Trans. Robot.*, vol. 27, pp. 389–400, 2011.

[24] T. Hoshi and H. Shinoda, "Robot skin based on touch-area-sensitive tactile element," *Proc. 2006 IEEE Int. Conf. Robot. Autom.*, pp. 3463–3468, 2006.

[25] J. C. Gwilliam, Z. Pezzementi, E. Jantho, A. M. Okamura, and S. Hsiao, "Human vs. robotic tactile sensing: Detecting lumps in soft tissue," *Haptics Symp. 2010 IEEE*, pp. 21–28, 2010.

[26] H. Liu, J. Li, X. Song, L. D. Seneviratne, and K. Althoefer, “Rolling Indentation Probe for Tissue Abnormality Identification During Minimally Invasive Surgery,” *IEEE Trans. Robot.*, vol. 27, no. 3, pp. 450–460, 2011.

[27] M. H. Lee, “Tactile Sensing: New Directions, New Challenges,” *Int. J. Rob. Res.*, vol. 19, pp. 636–643, 2000.

[28] H. Liu, D. P. Noonan, B. J. Challacombe, P. Dasgupta, L. D. Seneviratne, and K. Althoefer, “Rolling mechanical imaging for tissue abnormality localization during minimally invasive surgery.,” *IEEE Trans. Biomed. Eng.*, vol. 57, no. 2, pp. 404–414, Feb. 2010.

[29] H.-K. Kim, S.-G. Lee, J.-E. Han, T.-R. Kim, S.-U. Hwang, S. D. Ahn, I.-K. You, K.-I. Cho, T.-K. Song, and and K.-S. Yun., “Transparent and flexible tactile sensor for multi touch screen application with force sensing,” *Solid-State Sensors, Actuators Microsystems Conf. 2009. TRANSDUCERS 2009. Int.*, pp. 1146–1149, 2009.

[30] Y. Susuki, K. Yamada, S. Shimizu, Y. Ohno, T. Nagakura, and K. Ishihara, “Development of new type tactile endoscope with silicone rubber membrane,” *World Autom. Congr. (WAC), 2010*, pp. 1–6, 2010.

[31] E. P. Westebring-van der Putten, R. H. M. Goossens, J. J. Jakimowicz, and J. Dankelman, “Haptics in minimally invasive surgery--a review.,” *Minim. Invasive Ther. Allied Technol.*, vol. 17, pp. 3–16, 2008.

[32] H. R. Nicholls and M. H. Lee, “A Survey of Robot Tactile Sensing Technology,” *The International Journal of Robotics Research*, vol. 8. pp. 3–30, 1989.

[33] J. Tegin and J. Wikander, “Tactile sensing in intelligent robotic manipulation – a review,” *Ind. Robot An Int. J.*, vol. 32, no. 1, pp. 64–70, 2005.

[34] M. H. Lee and H. R. Nicholls, “Review Article Tactile sensing for mechatronics—a state of the art survey,” *Mechatronics*, vol. 9, no. 1, pp. 1–31, 1999.

[35] F. Yi, A. Lopez Cabezas, C. Qiang, Z. Li-Rong, and Z.-B. Zhang, “Flexible UHF Resistive Humidity Sensors Based on Carbon Nanotubes,” *Sensors Journal, IEEE*, vol. 12, no. 9, pp. 2844–2850, 2012.

[36] C. S. Park, J. Park, and D. W. Lee, “A piezoresistive tactile sensor based on carbon fibers and polymer substrates,” *Microelectron. Eng.*, vol. 86, no. 4, pp. 1250–1253, 2009.

[37] A. Wisitsoraat, V. Patthanasetakul, T. Lomas, and A. Tuantranont, “Low cost thin film based piezoresistive MEMS tactile sensor,” *Sensors Actuators, A Phys.*, vol. 139, no. 1, pp. 17–22, 2007.

[38] K. Weiss and H. Worn, “The working principle of resistive tactile sensor cells,” *IEEE Int. Conf. Mechatronics Autom. 2005*, vol. 1, pp. 471–476, 2005.

[39] N. Wettels, J. A. Fishel, and G. E. Loeb, “Multimodal Tactile Sensor,” in *The Human Hand as an Inspiration for Robot Hand Development*, Springer International Publishing, 2014, pp. 405–429.

[40] N. Wettels, V. J. Santos, R. S. Johansson, and G. E. Loeb, “Biomimetic Tactile Sensor Array,” *Adv. Robot.*, vol. 22, no. 8, pp. 829–849, 2008.

[41] J. Fishel and G. Loeb, “Sensing tactile microvibrations with the BioTac—Comparison with human sensitivity,” *Biomed. Robot. Biomechatronics (BioRob), 2012 4th IEEE RAS EMBS Int. Conf.*, pp. 1122–1127, 2012.

[42] J. Dargahi, “Piezoelectric tactile sensor with three sensing elements for robotic, endoscopic and prosthetic applications,” *Sensors Actuators, A Phys.*, vol. 80, no. 1, pp. 23–30, 2000.

[43] R. Sedaghati, J. Dargahi, and H. Singh, “Design and modeling of an endoscopic piezoelectric tactile sensor,” *Int. J. Solids Struct.*, vol. 42, no. 21, pp. 5872–5886, 2005.

[44] C. Li, P.-M. Wu, S. Lee, A. Gorton, M. J. Schulz, and C. H. Ahn, “Flexible Dome and Bump Shape Piezoelectric Tactile Sensors Using PVDF-TrFE Copolymer,” *J. Microelectromechanical Syst.*, vol. 17, no. 2, pp. 334–341, 2008.

[45] J. Dargahi, M. Parameswaran, and S. Payandeh, “A micromachined piezoelectric tactile sensor for an endoscopic grasper-theory, fabrication and experiments,” *J. Microelectromechanical Syst.*, vol. 9, no. 3, pp. 329–335, Sep. 2000.

[46] C. Chuang, W. Dong, and W. Lo, “Flexible piezoelectric tactile sensor with structural electrodes array for shape recognition system,” *2008 3rd Int. Conf. Sens. Technol.*, pp. 504–507, Nov. 2008.

[47] L. R. Smith, “Springer handbook of materials measurement method,” H. Czichos, T. Saito, and and L. Smith, Eds. Vol. 978. No. 3-20786. Springer, 2006.

[48] R. J. Stephen, K. Rajanna, V. Dhar, K. G. K. Kumar, and S. Nagabushanam, “Thin-film strain gauge sensors for ion thrust measurement,” *IEEE Sens. J.*, vol. 4, no. 3, pp. 373–377, 2004.

[49] G. Tholey and J. P. Desai, “A Compact and Modular Laparoscopic Grasper With Tridirectional Force Measurement Capability,” *J. Med. Device.*, vol. 2, no. 3, p. 031001, 2008.

[50] P. J. Berkelman, L. L. Whitcomb, R. H. Taylor, and P. Jensen, “A miniature microsurgical instrument tip force sensor for enhanced force feedback during robot-assisted manipulation,” *IEEE Trans. Robot. Autom.*, vol. 19, no. 5, pp. 917–922, Oct. 2003.

[51] E. S. Hwang, J. hoon Seo, and Y. J. Kim, “A Polymer-Based Flexible Tactile Sensor for Both Normal and Shear Load Detections and Its Application for Robotics,” *J. Microelectromechanical Syst.*, vol. 16, no. 3, pp. 556–563, Jun. 2007.

[52] C.-T. Ko, S.-H. Tseng, and M. S.-C. Lu, “A CMOS Micromachined Capacitive Tactile Sensor With High-Frequency Output,” *J. Microelectromechanical Syst.*, vol. 15, no. 6, pp. 1708–1714, 2006.

[53] M. Maggiali, G. Cannata, P. Maiolino, G. Metta, M. Randazzo, and G. Sandini, “Embedded Distributed Capacitive Tactile Sensor,” in *11th Mechatronics Forum Biennial International Conference*, 2008, pp. 1–5.

[54] J. G. Rocha, C. Santos, J. M. Cabral, and S. Lanceros-Mendez, “3 Axis Capacitive Tactile Sensor and Readout Electronics,” *2006 IEEE Int. Symp. Ind. Electron.*, vol. 4, pp. 2767–2772, 2006.

[55] “Pressure Profile Systems Inc., Robotouch — Overview,” 2007. [Online]. Available: http://www.pressureprofile.com/products-robotouch.

[56] H. Lee, J. Chung, S. Chang, and E. Yoon, “Normal and Shear Force Measurement Using a Flexible Polymer Tactile Sensor With Embedded Multiple Capacitors,” *J. Microelectromechanical Syst.*, vol. 17, no. 4, pp. 934–942, Aug. 2008.

[57] A. Ben Amor, T. Budde, and H. H. Gatzen, “A magnetoelastic microtransformer-based microstrain gauge,” *Sensors Actuators, A Phys.*, vol. 129, no. 1, pp. 41–44, 2006.

[58] S. Takenawa, “A magnetic type tactile sensor using a two-dimensional array of inductors,” *2009 IEEE Int. Conf. Robot. Autom.*, pp. 3295–3300, 2009.

[59] S. Yang, X. Chen, H. Aoki, and S. Motojima, “Tactile microsensor elements prepared from aligned superelastic carbon microcoils and polysilicone matrix,” *Smart Mater. Struct.*, vol. 15, no. 3, pp. 687–694, 2006.

[60] S. Takenawa, “A soft three-axis tactile sensor based on electromagnetic induction,” *Mechatronics, 2009. ICM 2009. IEEE Int. Conf.*, pp. 1–6, 2009.

[61] R. L. Shell and E. L. Hall, *Handbook of Industrial Automation*, vol. 65. 2000, pp. 381–382.

[62] K. Kamiyama, H. Kajimoto, N. Kawakami, and S. Tachi, “Evaluation of a vision-based tactile sensor,” *IEEE Int. Conf. Robot. Autom. 2004. Proceedings. ICRA ’04. 2004*, vol. 2, 2004.

[63] J. Ueda, Y. Ishida, M. Kondo, and T. Ogasawara, “Development of the NAIST-Hand with Vision-based Tactile Fingertip Sensor,” *Proc. 2005 IEEE Int. Conf. Robot. Autom.*, pp. 2332–2337, 2005.

[64] O. Duran, K. Althoefer, and L. D. Seneviratne, “Automated sewer pipe inspection through image processing,” *Proc. 2002 IEEE Int. Conf. Robot. Autom.*, vol. 3, pp. 2551–2556, 2002.

[65] D. Hristu, N. Ferrier, and R. W. Brockett, “The performance of a deformable-membrane tactile sensor: basic results on geometrically-defined tasks,” *Robot. Autom. 2000. Proceedings. ICRA’00. IEEE Int. Conf.*, vol. 1, pp. 508–513, 2000.

[66] Y. Ito, Y. Kim, and G. Obinata, “Robust Slippage Degree Estimation Based on Reference Update of Vision-Based Tactile Sensor,” *IEEE Sens. J.*, vol. 11, no. 9, pp. 2037–2047, Sep. 2011.

[67] K. Kamiyama, K. Vlack, T. Mizota, H. Kajimoto, N. Kawakami, and S. Tachi, “Vision-based sensor for real-time measuring of surface traction fields,” *Comput. Graph. Appl. IEEE 25*, vol. 25, no. 1, pp. 68–75, 2005.

[68] K. Vlack and K. Kamiyama, “GelForce : A Vision-based Traction Field Computer Interface,” *CHI’05 Ext. Abstr. Hum. factors Comput. Syst.*, pp. 1154–1155, 2005.

[69] K. Sato, K. Kamiyama, N. Kawakami, and S. Tachi, “Finger-Shaped GelForce: Sensor for Measuring Surface Traction Fields for Robotic Hand,” *IEEE Trans. Haptics*, vol. 3, no. 1, pp. 37–47, 2010.

[70] K. T. V Grattan and T. Sun, “Fiber optic sensor technology: An overview,” *Sensors Actuators, A Phys.*, vol. 82, pp. 40–61, 2000.

[71] M. Rothmaier, M. P. Luong, and F. Clemens, “Textile Pressure Sensor Made of Flexible Plastic Optical Fibers,” *Sensors*, vol. 8, no. 7, pp. 4318–4329, Jul. 2008.

[72] P. Lang, “Design and prototyping of a fiber optic tactile array,” in *In Electrical and Computer Engineering, 2008. CCECE 2008. Canadian Conference on*, 2008, pp. 373–376.

[73] S. J. Mihailov, “Fiber Bragg grating sensors for harsh environments.,” *Sensors (Basel).*, vol. 12, no. 2, pp. 1898–918, Jan. 2012.

[74] T. Yoshino, K. Kurosawa, K. Itoh, and T. Ose, “Fiber-Optic Fabry-Perot Interferometer and its Sensor Applications,” *IEEE Trans. Microw. Theory Tech.*, vol. 30, no. 10, pp. 1612–1621, Oct. 1982.

[75] R. Sargeant, L. D. Seneviratne, and K. Althoefer, “A 2-Axis Optical Force–Torque Fingertip Sensor for Dexterous Grasping Using Linear Polarizers,” *IEEE Trans. Instrum. Meas.*, vol. 61, no. 12, pp. 3363–3377, Dec. 2012.

[76] H. Yussof, J. Wada, and M. Ohka, “Sensorization of robotic hand using optical three-axis tactile sensor: Evaluation with grasping and twisting motions,” *J. Comput. Sci.*, vol. 6, no. 8, pp. 955–962, 2010.

[77] J.-S. Heo, J.-H. Chung, and J.-J. Lee, “Tactile sensor arrays using fiber Bragg grating sensors,” *Sensors and Actuators A: Physical*, vol. 126. pp. 312–327, 2006.

[78] J. S. Heo, J. H. Chung, and J. J. Lee, “Tactile sensor arrays using fiber Bragg grating sensors,” *Sensors Actuators A Phys.*, vol. 126, no. 2, pp. 312–327, 2006.

[79] P. D. Goodyer, J. C. Fothergill, N. B. Jones, and and C. D. Hanning., “The design of an optical fiber pressure transducer for use in the upper airways,” *Biomed. Eng. IEEE Trans.*, vol. 43, no. 6, pp. 600–606, 1996.

[80] P. Polygerinos, P. Puangmali, T. Schaeffter, R. Razavi, L. D. Seneviratne, and K. Althoefer, “Novel miniature MRI-compatible fiber-optic force sensor for cardiac catheterization procedures,” *Robot. Autom. (ICRA), 2010 IEEE Int. Conf.*, 2010.

[81] H. Liu, P. Puangmali, K. Althoefer, and L. D. Seneviratne, “Experimental study of soft tissue recovery using optical fiber probe,” *2007 IEEE/RSJ Int. Conf. Intell. Robot. Syst.*, pp. 516–521, Oct. 2007.

[82] P. Puangmali, K. Althoefer, and L. D. Seneviratne, “Mathematical Modeling of Intensity-Modulated Bent-Tip Optical Fiber Displacement Sensors,” *IEEE Trans. Instrum. Meas.*, vol. 59, no. 2, pp. 283–291, Feb. 2010.

[83] M. Poirier-Quinot, G. Frasca, C. Wilhelm, N. Luciani, J.-C. Ginefri, L. Darrasse, D. Letourneur, C. Le Visage, and F. Gazeau, “High-resolution 1.5-Tesla magnetic resonance imaging for tissue-engineered constructs: a noninvasive tool to assess three-dimensional scaffold architecture and cell seeding.,” *Tissue Eng. Part C. Methods*, vol. 16, no. 2, pp. 185–200, 2010.

[84] S. Li and P. H. Wu, “Magnetic resonance image-guided versus ultrasound-guided high-intensity focused ultrasound in the treatment of breast cancer.,” *Chin. J. Cancer*, vol. 32, no. 8, pp. 441–52, 2013.

[85] R. Gassert and R. Moser, “MRI/fMRI-compatible robotic system with force feedback for interaction with human motion,” *Mechatronics, IEEE/ASME Trans.*, vol. 11, no. 2, pp. 216–224, 2006.

[86] H. Elhawary, Z. T. H. Tse, A. Hamed, M. Rea, B. L. Davies, and M. U. Lamperth, “The case for MR-compatible robotics: a review of the state of the art.,” *Int. J. Med. Robot. Comput. Assist. Surg.*, vol. 4, no. 2, pp. 105–113, 2008.

[87] A. M. Okamura, “Methods for haptic feedback in teleoperated robot-assisted surgery,” *Ind. Robot An Int. J.*, vol. 31, no. 6, pp. 499–508, 2004.

[88] A. M. Hamed, Z. T. H. Tse, I. Young, B. L. Davies, and M. Lampérth, “Applying tactile sensing with piezoelectric materials for minimally invasive surgery and magnetic-resonance-guided interventions.,” *Proc. Inst. Mech. Eng. H.*, vol. 223, no. 1, pp. 99–110, 2009.

[89] P. Polygerinos, L. D. Seneviratne, and K. Althoefer, “Modeling of Light Intensity-Modulated Fiber-Optic Displacement Sensors,” *IEEE Trans. Instrum. Meas.*, vol. 60, no. 4, pp. 1408–1415, 2011.

[90] M. P. Ottensmeyer, “Minimally Invasive Instrument for In Vivo Measurement of Solid Organ Mechanical Impedance,” PhD Thesis, Massachusetts Institute of Technology, 2001.

[91] N. McDannold and S. E. Maier, “Magnetic resonance acoustic radiation force imaging,” *Med. Phys.*, vol. 35, no. 8, pp. 3748–3758, 2008.

[92] H. Liu, J. Greco, X. Song, J. Bimbo, L. Senerivatne, and K. Althoefer, “Tactile Image based Contact Shape Recognition using Neural Network,” in *2012 IEEE International Conference on Multisensor Fusion and Integration for Intelligent Systems (MFI)*, 2012, pp. 138–143.

[93] T. Coles, D. Meglan, and N. John, “The role of haptics in medical training simulators: a survey of the state of the art,” *Haptics, IEEE Trans.*, vol. 4, no. 1, pp. 51–66, 2011.

[94] M. Ayyildiz and B. Guclu, “An Optoelectromechanical Tactile Sensor for Detection of Breast Lumps,” *Haptics, IEEE Trans.*, vol. 6, no. 2, pp. 145–155, 2013.

[95] Q. Peng, S. Omata, D. M. Peehl, and C. E. Constantinou, “Stiffness mapping prostate biopsy samples using a tactile sensor.,” *Conf. Proc. IEEE Eng. Med. Biol. Soc.*, vol. 2011, pp. 8515–8, Jan. 2011.

[96] Y. Park and J. W. Ha, “Comparison of one-level posterior lumbar interbody fusion performed with a minimally invasive approach or a traditional open approach.,” *Spine (Phila. Pa. 1976).*, vol. 32, no. 5, pp. 537–543, 2007.

[97] J. Rosen, B. Hannaford, M. P. MacFarlane, and M. N. Sinanan, “Force controlled and teleoperated endoscopic grasper for minimally invasive surgery--experimental performance evaluation.,” *IEEE Trans. Biomed. Eng.*, vol. 46, no. 10, pp. 1212–21, Oct. 1999.

[98] G.-P. Haber, M. A. White, R. Autorino, P. F. Escobar, M. D. Kroh, S. Chalikonda, R. Khanna, S. Forest, B. Yang, F. Altunrende, R. J. Stein, and J. H. Kaouk, “Novel robotic da Vinci instruments for laparoendoscopic single-site surgery.,” *Urology*, vol. 76, no. 6, pp. 1279–82, Dec. 2010.

[99] K. Sangpradit, H. Liu, L. D. Seneviratne, and K. Althoefer, “Tissue identification using inverse Finite Element analysis of rolling indentation,” *2009 IEEE Int. Conf. Robot. Autom.*, pp. 1250–1255, 2009.

[100] M. V. Ottermo, O. Stavdahl, and T. A. Johansen, “Palpation instrument for augmented minimally invasive surgery,” *2004 IEEE/RSJ Int. Conf. Intell. Robot. Syst.*, vol. 4, pp. 3960–3964, 2004.

[101] P. Peng, A. S. Sezen, R. Rajamani, and A. G. Erdman, "Novel MEMS stiffness sensor for force and elasticity measurements," *Sensors Actuators A Phys.*, vol. 158, no. 1, pp. 10–17, Mar. 2010.

[102] K. Tadano and K. Kawashima, "Development of 4-DOFs forceps with force sensing using pneumatic servo system," in *Proceedings of IEEE International Conference on Robotics and Automation, 2006*, 2006, pp. 2250–2255.

[103] G. McCreery and A. Trejos, "Feasibility of locating tumours in lung via kinaesthetic feedback," *Int. J. Med. Robot. Comput. Assist. Surg.*, vol. 4, no. 1, pp. 58–68, 2008.

[104] B. Ahn, Y. Kim, C. K. Oh, and J. Kim, "Robotic palpation and mechanical property characterization for abnormal tissue localization.," *Med. Biol. Eng. Comput.*, vol. 50, no. 9, pp. 961–71, Sep. 2012.

[105] H. Liu, P. Puangmali, D. Zbyszewski, O. Elhage, P. Dasgupta, J. S. Dai, L. Seneviratne, and K. Althoefer, "An indentation depth–force sensing wheeled probe for abnormality identification during minimally invasive surgery," *Proc. Inst. Mech. Eng. Part H J. Eng. Med.*, vol. 224, no. 6, pp. 751–763, Jun. 2010.

[106] M. Li, J. Konstantinova, V. Aminzadeh, T. Nanayakkara, L. D. Seneviratne, P. Dasgupta, and K. Althoefer, "Real-time Visual Stiffness Feedback for Soft Tissue Palpation in a Telemanipulation Environment," in *Hamlyn Simposium*, 2013, pp. 77–78.

[107] R. D. Howe, W. J. Peine, D. A. Kantarinis, and J. S. Son, "Remote palpation technology," *Eng. Med. Biol. Mag. IEEE*, vol. 14, no. 3, pp. 318–323, 1995.

[108] E. Petter, M. Biehl, and J. U. Meyer, "Vibrotactite Palpation Instrument for Use in Minimal Invasive Surgery," *Eng. Med. Biol. Soc. 1996. Bridg. Discip. Biomed. Proc. 18th Annu. Int. Conf. IEEE*, vol. 1, pp. 179–180, 1996.

[109] P. Peng and R. Rajamani, "Handheld microtactile sensor for elasticity measurement," *Sensors Journal, IEEE*, vol. 11, no. 9, pp. 1935–1942, 2011.

[110] V. Egorov, S. Ayrapetyan, and A. P. Sarvazyan, "Prostate mechanical imaging: 3-D image composition and feature calculations.," *IEEE Trans. Med. Imaging*, vol. 25, no. 10, pp. 1329–40, Oct. 2006.

[111] A. P. Miller, W. J. Peine, Jae S. Son, Z. T. Hammoud, J. S. Son, and Z. T. H. M. D, "Tactile imaging system for localizing lung nodules during video assisted thoracoscopic surgery," *Robot. Autom. 2007 IEEE Int. Conf.*, no. April, pp. 2996–3001, 2007.

[112] A. Talasaz and R. V. Patel, "Telerobotic palpation for tumor localization with depth estimation," *IEEE/RSJ Int. Conf. Intell. Robot. Syst.*, pp. 463–468, 2013.

[113] B. Kuebler, U. Seibold, and G. Hirzinger, "Development of actuated and sensor integrated forceps for minimally invasive robotic surgery," *Int. J. Med. Robot. Comput. Assist. Surg.*, vol. 01, no. 03, pp. 96–107, 2005.

[114] R. S. Dahiya, G. Metta, M. Valle, and G. Sandini, “Tactile Sensing—From Humans to Humanoids,” *IEEE Trans. Robot.*, vol. 26, no. 1, pp. 1–20, Feb. 2010.

[115] K. T. V. Grattan and T. Sun, “Fiber optic sensors: an introduction and overview,” in *Optical Fiber Sensor Technology*, Springer US, 2000, pp. 1–44.

[116] P. Polygerinos, A. Ataollahi, T. Schaeffter, R. Razavi, L. D. Seneviratne, and K. Althoefer, “MRI-compatible intensity-modulated force sensor for cardiac catheterization procedures.,” *IEEE Trans. Biomed. Eng.*, vol. 58, no. 4, pp. 721–726, 2011.

[117] H. Xie, A. Jiang, L. D. Seneviratne, and K. Althoefer, “Pixel-based optical fiber tactile force sensor for robot manipulation,” in *Sensors conference, 2012 IEEE*, 2012, pp. 1–4.

[118] P. Puangmali, P. Dasgupta, L. D. Seneviratne, and K. Althoefer, “Miniaturized triaxial optical fiber force sensor for MRI-Guided minimally invasive surgery,” in *In Robotics and Automation (ICRA), 2010 IEEE International Conference on*, 2010, pp. 2592–2597.

[119] P. Polygerinos, T. Schaeffter, L. Seneviratne, and K. Althoefer, “A fibre-optic catheter-tip force sensor with MRI compatibility: a feasibility study.,” in *Engineering in Medicine and Biology Society, 2009. EMBC 2009. Annual International Conference of the IEEE*, 2009, pp. 1501–1054.

[120] H. Xie, A. Jiang, H. A. Wurdemann, H. Liu, L. D. Seneviratne, and K. Althoefer, “Magnetic Resonance-Compatible Tactile Force Sensor Using Fiber Optics and Vision Sensor,” *IEEE Sens. J.*, vol. 14, no. 3, pp. 829–838, Mar. 2014.

[121] N. J. Ferrier and R. W. Brockett, “Reconstructing the Shape of a Deformable Membrane from Image Data,” *Int. J. Rob. Res.*, vol. 19, no. 9, pp. 795–816, Sep. 2000.

[122] H. Yussof, S. C. Abdullah, and M. Ohka, “Development of Optical Three-Axis Tactile Sensor and its Application to Robotic Hand for Dexterous Manipulation Tasks,” *2010 Fourth Asia Int. Conf. Math. Model. Comput. Simul.*, pp. 624–629, 2010.

[123] Q. Wan, O. Schoppe, S. Gunasekaran, D. Holland, E. Roche, H.-C. Hur, and C. Walsh, “Multifunctional Laparoscopic Trocar With Built-in Fascial Closure and Stabilization,” *J. Med. Device.*, vol. 7, no. 3, p. 030912, 2013.

[124] H. Xie, H. Liu, S. Luo, L. D. Seneviratne, and K. Althoefer, “Fiber optics tactile array probe for tissue palpation during minimally invasive surgery,” *IEEE/RSJ Int. Conf. Intell. Robot. Syst.*, pp. 2539–2544, 2013.

[125] P. K. Sahoo, S. Soltani, and A. K. C. Wong, “A survey of thresholding techniques,” *Comput. Vision, Graph. Image Process.*, vol. 41, no. 2, pp. 233–260, Feb. 1988.

[126] S. Al-amri and N. Kalyankar, “Image segmentation by using threshold techniques,” *arXiv Prepr. arXiv1005.4020*, vol. 2, no. 5, pp. 83–86, 2010.

[127] X. Jiang and D. Mojon, “Adaptive local thresholding by verification-based multithreshold probing with application to vessel detection in retinal images,” *Pattern Anal. Mach. Intell. IEEE Trans.*, vol. 25, no. 1, pp. 131–137, 2003.

[128] J. L. Fan and B. Lei, “A modified valley-emphasis method for automatic thresholding,” *Pattern Recognit. Lett.*, vol. 33, no. 6, pp. 703–708, Apr. 2012.

[129] P. Puangmali, L. D. Seneviratne, P. Dasgupta, and K. Althoefer, “Miniature 3-Axis Distal Force Sensor for Minimally Invasive Surgical Palpation,” *IEEE/ASME Trans. Mechatronics*, vol. 17, no. 4, pp. 646–656, Aug. 2012.

[130] K. Sangpradit, H. Liu, P. Dasgupta, K. Althoefer, and L. D. Seneviratne, “Finite-element modeling of soft tissue rolling indentation.,” *IEEE Trans. Biomed. Eng.*, vol. 58, no. 12, pp. 3319–3327, Dec. 2011.

[131] V. Egorov, S. Tsyuryupa, S. Kanilo, M. Kogit, and A. Sarvazyan, “Soft tissue elastometer,” *Med. Eng. Phys.*, vol. 30, no. 2, pp. 206–212, 2008.

[132] A. Talasaz and R. V. Patel, “Integration of Force Reflection with Tactile Sensing for Minimally Invasive Robotics-Assisted Tumor Localization,” *Haptics, IEEE Trans.*, vol. 6, no. 2, pp. 217–228, 2013.

[133] P. Valdastri, K. Harada, A. Menciassi, L. Beccai, C. Stefanini, M. Fujie, and P. Dario, “Integration of a miniaturised triaxial force sensor in a minimally invasive surgical tool.,” *IEEE Trans. Biomed. Eng.*, vol. 53, pp. 2397–2400, 2006.

[134] K. Yokoyama, H. Nakagawa, D. C. Shah, H. Lambert, G. Leo, N. Aeby, A. Ikeda, J. V Pitha, T. Sharma, R. Lazzara, and W. M. Jackman, “Novel contact force sensor incorporated in irrigated radiofrequency ablation catheter predicts lesion size and incidence of steam pop and thrombus.,” *Circ. Arrhythm. Electrophysiol.*, vol. 1, no. 5, pp. 354–362, 2008.

[135] U. Seibold, B. Kübler, and G. Hirzinger, “Prototype of instrument for minimally invasive surgery with 6-axis force sensing capability,” *ICRA*, pp. 498–503, 2005.

[136] A. L. Trejos, R. V Patel, and M. D. Naish, “Force sensing and its application in minimally invasive surgery and therapy: a survey,” *Proc. Inst. Mech. Eng. Part C J. Mech. Eng. Sci.*, vol. 224, pp. 1435–1454, 2010.

[137] V. Gupta, N. Reddy, and P. Batur, “Forces in surgical tools: comparison between laparoscopic and surgical forceps,” *Eng. Med. Biol. Soc. 1996. Bridg. Discip. Biomed. Proc. 18th Annu. Int. Conf. IEEE*, vol. 1, pp. 223–224, 1996.

[138] G. Picod, A. C. Jambon, D. Vinatier, and P. Dubois, "What can the operator actually feel when performing a laparoscopy?," *Surg. Endosc.*, vol. 19, no. 1, pp. 95–100, Jan. 2005.

[139] P. Dubois, Q. Thommen, and A. C. Jambon, "In vivo measurement of surgical gestures," *IEEE Trans. Biomed. Eng.*, vol. 49, no. 1, pp. 49–54, Jan. 2002.

[140] J. J. van den Dobbelsteen, A. Schooleman, and J. Dankelman, "Friction dynamics of trocars.," *Surg. Endosc.*, vol. 21, pp. 1338–1343, 2007.

[141] A. Okamura, L. Verner, C. Reiley, and M. Mahvash, "Haptics for robot-assisted minimally invasive surgery," *Robot. Res.*, vol. 2, pp. 361–372, 2011.

[142] S. B. Kesner and R. D. Howe, "Design Principles for Rapid Prototyping Forces Sensors using 3D Printing," *IEEE/ASME Trans. mechatronics*, vol. 16, no. 5, pp. 1–5, Jul. 2011.